UNIVERSITÀ DEGLI STUDI DI
CASSINO E DEL LAZIO MERIDIONALE

Corso di Dottorato in
Metodi, Modelli e Tecnologie per l'Ingegneria
Curriculum: Ingegneria Elettrica
Ciclo XXXV

Hybrid Energy Storage Systems for Electric Vehicles and Stationary Applications

SSD: ING/IND-32

Supervisor
Prof. Giuseppe Tomasso

Ph.D. Student
Davide Fusco

Coordinator
Prof. Fabrizio Marignetti

February 2023

UNIVERSITÀ DEGLI STUDI DI
CASSINO E DEL LAZIO MERIDIONALE

Date: **February 2023**

Author: **Davide Fusco**

Title: **Hybrid Energy Storage Systems for Electric Vehicles and Stationary Applications**

Department: **Dipartimento di Ingegneria Elettrica e dell'Informazione "M. Scarano"**

Degree: **PHILOSOPHIAE DOCTOR**

To "Nonno Stefano"

My greatest example of honesty, hard work and gratitude.

My dream is to become the person he was.

Acknowledgments

I would like to sincerely thank my supervisor, Prof. Giuseppe Tomasso, for his precious guidance and support towards my Ph.D. studies. I also thank all the team of the Laboratory of Industrial Automation of the University of Cassino and Southern Lazio for all the skills and knowledge they transmitted to me. A special mention to Dr. Mauro Di Monaco and Dr. Francesco Porpora for their endless help and encouragement in always improving myself.

I wish to express my gratitude to Prof. Giovanni De Carne for the opportunity to spend my abroad period at the Karlsruhe Institute of Technology, within the Institute for Technical Physics, and for his priceless support during this experience.

To my family, all my gratitude for encouraging me and being at my side this whole time, always ready to help me in whatever I needed, while giving me all the joy and love a person can ever imagine, and even more.

Last but not least, I thank all my friends of a lifetime and the ones I met during my university life. They surrounded me with friendliness and love, and I know they will always be there for me.

Contents

Introduction

The research activity described in this dissertation is related to the design and prototyping of Energy Storage Systems (ESSs) and advanced control algorithms to enhance their performances while ensuring safe operation. In particular, three main tasks can be distinguished in this research activity. The first one deals with the development of advanced state estimators for extending the lifetime of Lithium-Ion battery packs, accurately assessing the State of Charge (SoC) at cell level and, concurrently, at pack level as well as managing the cell-to-cell inaccuracies and imbalance conditions. Secondly, Hybrid Energy Storage Systems (HESSs) for stationary and automotive applications have been investigated. In detail, the activity has regarded the development of a battery/supercapacitor storage system and the SoC estimation algorithms for all the involved storage systems to enable advanced power allocation control strategies. The third task includes the sizing and the implementation of bidirectional DC-DC power converters for interconnecting different high-voltage storage systems and energy sources in stationary and automotive applications. HESSs and Electric Vehicles (EVs) application fields have been chosen due to their high performance requirements in terms of current profiles, fast response and system dynamics as well as size, costs and reliability of the integrated structure.

Motivation

The dependence on traditional energy sources, global warming and environmental pollution problems have been among the most concerning topics in the last few years. Worldwide public authorities, including the European Union (EU), are defining increasingly strict regulations on pollutant emissions and fossil fuels consumption. Major efforts are made in reducing greenhouse gas (GHG) and pollutant emissions as well as in maximizing the integration of Renewable En-

ergy Sources (RESs). In detail, the EU defined global climate goals to be fulfilled by 2030, including a 55% reduction in GHG emissions with respect to 1990 levels, 40% of energy production from RESs and a 55% of average emission reduction in automotive sector.

However, according to data reports from the International Energy Agency, the power sector, including electricity generation, accounts for the 40% of total CO_2 emissions, and the bigger part of them is accounted to coal-fired power plants. In addition, the transport sector is responsible for the 23% of global emissions, mainly due to road transport.

In this context, one of the leading solutions to address the challenge of global warming through integrating Renewable Energy Sources (RES) in the power system is using Energy Storage Systems (ESS). On the other hand, the electrification of the automotive field can significantly contribute to decarbonisation and emission reduction of the transport sector. However, consistent efforts in technology innovations development are still required to accelerate EVs adoption and storage systems integration.

Currently, in the electric powertrain of an EV, the battery system strongly limits the overall costs and performances. On the other hand, inadequate dynamic response and power control challenges for battery storage systems limit the storage integration with RESs in the grid infrastructure. Therefore, the development of new battery technologies as well as hybrid systems consisting of different ESSs can lead to simultaneously meeting the needs of high specific power and energy density. Moreover, the performance increase of storage systems is one of the main factors leading the increasing developments in Battery Management Systems (BMSs).

Likewise, power converter are integral part of the system in applications requiring high performance and reliability, such as high-power charging stations for EVs and HESS topologies. In both application fields, high efficiency, bidirectional power transfer and input/output galvanic isolation are the main requirements. Therefore, the development of high performance and high efficiency power converters for EVs and stationary applications can strongly impact on their adoption in transport and power sectors.

The main motivations of this dissertation include the development of advanced BMSs for Lithium-Ion battery packs and
battery/supercapacitor HESSs, capable of estimating cell-to-cell state conditions variability and accurate SoC knowledge for each storage system involved. In addition, high performance DC-DC converters

need to be integrated in the system to maximize the energy and power capability of the storage system while ensuring safe operating conditions.

Original Contribute

High performance storage systems, such as Hybrid and Battery Energy Storage Systems, are required in stationary and automotive application fields to lead the electrification of the road transport sector as well as the integration of renewable energy sources in the power system. However, the development of pure and hybrid battery packs require effective Battery Management Systems (BMSs) to ensure performance exploitation and safe operating conditions. On the other hand, high efficiency and fast dynamic response are required from the integrated power electronic converters to effectively interconnect the whole power system.

This dissertation has focused on the development of an advanced BMS for automotive battery pack application as well as stationary HESS systems. In particular, the State of Charge (SoC) estimation has been investigated to develop accurate and reliable solutions for state estimation both at cell and pack level. Subsequently, the hybridization of energy storage systems has been investigated and the SoC estimation functionality has been implemented for HESSs considering a battery and supercapacitor integration.

The main contribution has concerned the development of accurate models for both supercapacitors and battery systems as well as the design of advanced and reliable model-based state estimation algorithms to improve the system performances.

Subsequently, DC-DC power converters for smooth integration of different storage technologies and their interconnection in power systems have been investigated. A design methodology for Dual-Active-Bridge converters has been defined by taking into account main system requirements. Moreover, advanced modulation techniques and control strategies have been investigated and a real prototype has been implemented for experimental validation. In detail, a modular 25-kW SiC-based DAB converter, working at 100 kHz switching frequency, has been prototyped with the aim of performance evaluating in real-world application.

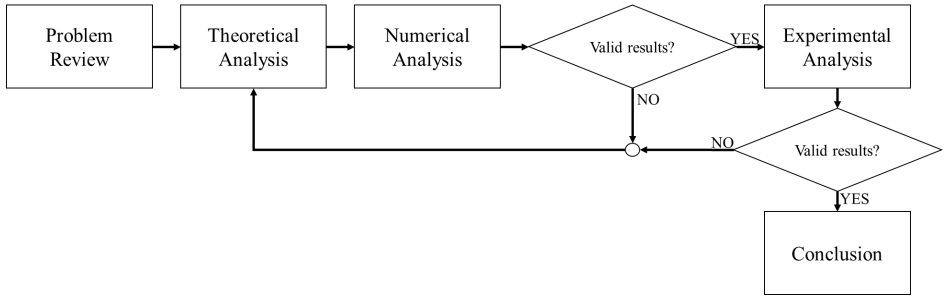

Figure 1: Flowchart of the adopted methodological approach.

Methodology

The adopted methodology is of paramount importance to define a systematic approach in the research activity. The experimental-based approach depicted in figure 1 has been adopted in this dissertation. It can be summarized in the following steps:

- **Problem review**: an extended bibliographic study is needed to gain familiarity with the specific topic. All the functionalities and implementation objectives of Energy Storage Systems have been investigated with particular focus on the conversion stages involved in battery systems and HESSs. Moreover, model-based state estimation methods and their applications in SoC evaluation for battery packs and supercapacitors have been analyzed. In addition, related topics, such as State of Health (SoH) and DC-AC high power converters have been studied in order to gain widespread knowledge in the research topics and similar application fields.

- **Theoretical Analysis**: in this phase, mathematical models are developed to analyze the faced problem from a scientific point of view. Moreover, analytical and/or experimental approach for identifying the model parameters are investigated. This step allow to deeply understand strengths and weaknesses of the mainly adopted solution and, thus, leading to new algorithms and control strategies proposal.

- **Numerical Analysis**: with the numerical analysis, the estimation performances of the proposed methodology have been compared to conventional and state-of-the-art methods, highlighting necessary improvements and further implementation steps.

Moreover, the design approach of DC-DC converters for energy storage systems has been preliminary validated in numerical environment in order to demonstrate its effectiveness.

- **Experimental Analysis**: once the numerical validation is passed, the experimental set-up is designed and implemented to fully validate the estimation accuracy and reliability of the developed algorithm. Furthermore, the same approach has been pursued for the Dual-Active-Bridge converter and its performances in terms of efficiency and power control have been experimentally validated.

Summary

The dissertation is organized in five chapters. The first one reports the fundamentals of Energy Storage Systems for stationary and automotive application fields, while power converters for storage systems are discussed in the second one. The third section illustrates an overview of the BMS functionality with focus on SoC estimation methods for ESSs. The last two chapters highlight the original contribute of the proposed research activity, including the development of model-based SoC estimation algorithms for battery packs and supercapacitors as well as the DAB converter prototyped and implemented in real-world application.
In detail, the dissertation is organized as follows:

- **Chapter 1** provides an overview on main characteristics of Energy Storage Systems as well as benefits and challenges for vehicle electrification and grid-support stationary applications. Moreover, different architectures for Hybrid Energy Storage Systems are illustrated, highlighting advantages and disadvantages of each solution.

- **Chapter 2** introduces the power converters for storage systems and main DC-DC converters in automotive and stationary applications are discussed.

- **Chapter 3** is focused on model-based algorithms for SoC estimation in batteries both at cell and pack level and in high power supercapacitors. In particular, different variants of Kalman Filters combined with different plant models have been considered.

Furthermore, mathematical and implementation details of the investigated estimators as well as the modeling procedures and techniques are provided in this section.

- **Chapter 4** illustrates the proposed solutions for state estimation in Lithium-based battery packs and in supercapacitors for HESSs implementation. In detail, an Adaptive Square-Root Unscented Kalman Filter has been developed and its integration with different battery and supercapacitor models has been investigated. The impact of model accuracy and parameter variations and the system operating conditions has been evaluated as well.
- **Chapter 5** presents the details related to the development, sizing and implementation of the real prototype of the considered Dual-Active-Bridge converter. The design performances and the project requirements have been validated by means of experimental tests in real-world implementation. Typical automotive and stationary operating conditions have been evaluated since in both cases high performances in terms of power, fast dynamics and efficiency as well as system reliability are required.

Chapter 1

Fundamentals of Energy Storage Systems

Energy storage systems based on Lithium-Ion batteries are widely adopted in Hybrid and Electric Vehicles, as well as in stationary applications. These application fields increasingly demand high performance and reliability, resulting in the need for fast response and high power and energy capability. However, in order to fully benefit from system characteristics, in many cases different storage technologies are coupled for enhancing both power and energy density while ensuring safe operation and longer useful life. This gives the Battery Management System (BMS) an important role in monitoring the state conditions of each storage system, such as State of Charge (SoC) and State of Health (SoH), which result fundamental in power management strategy in order to maximize efficiency and lifetime.
In this chapter, an overview of energy storage technologies, with a focus on Lithium-Ion batteries and dual layer supercapacitors is presented. Morevoer, different hybrid solutions for both EVs and stationary applications are introduced and their characteristics are discussed.

1.1 Energy situation

Nowadays, the environmental problem is of primary concern in worldwide public opinion, and decarbonization, as well as emission and pollution reduction, are leading research efforts in maximizing the use of Renewable Energy Sources (RESs) and in road transport electrification. Indeed, public authorities, including European Union (EU),

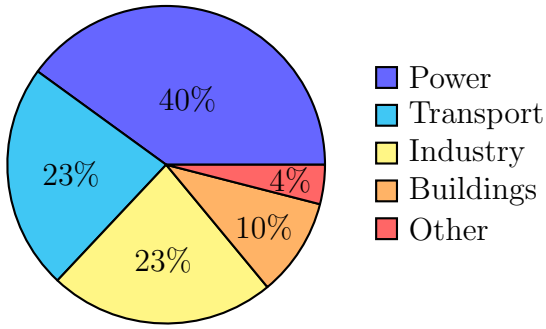

Figure 1.1: Global energy-related CO_2 emissions by sector. *Source: International Energy Agency.*

are issuing strict regulations on pollutant emissions and fossil fuels consumption. With the Paris Agreement, countries have committed to pursue efforts in order to maintain the Earth temperature increase below 1.5°C. Global warming is mainly related to the uncontrolled emissions of carbon dioxide gas (CO_2), which has been continuously increased by human activities in the past decades. Figure 1.1 shows the global CO_2 emissions related to energy production and consumption, divided by sector. The power sector, including electricity generation, accounts for the bigger part of CO_2 emissions, while the 75% of them is due to coal-fired power plants, meaning that foundamental actions have to be taken in energy production regards. In addition, a consistent contribution is given by the transport sector, which is responsible for 23% of global emissions, the largest part of which is due to road transport. Indeed, passenger road vehicles contributed for 3.6 Gt of CO_2 production, while 2.4 Gt were accounted to road freight vehicles, representing 44% and the 30% over the total transport sector emissions, respectively. Considering that the transport sector still relies on oil products for 91% of its final energy, the electrification of road vehicles represents a strategic move towards sustainability and consistent CO_2 emission reduction.

As a matter of fact, both energy and transport sectors have been included in the global climate goals, recently defined by the EU to be fulfilled by 2030, as follows:

- 55% reduction of net greenhouse gas emissions, compared to 1990 levels;
- 40% of energy production from RESs;

- 55% average emissions reduction of new cars;

As a consequence, in the past decades, the interest in installing new distributed energy generators has increased, and the use of renewable energy is nowadays widespread. However, the typical variability and lower inertia of Renewable Energy Sources (RES), compared to traditional sources, makes the grid support, in terms of voltage and frequency regulation as well as the need for energy reservoir, a crucial task for embracing their full utilization in the grid infrastructure. The most promising solution for moving towards a sustainable power sector is represented by Energy Storage Systems (ESSs). ESS overcomes the intermittency and unpredictability of RES by saving energy at the time of less demand and discharging when the demand is high [1]. With the deployment of ESS in an electricity system, voltage instability, frequency fluctuation, poor power quality, load-following, and other power system challenges could be mitigated [2]. On the other hand, a significant decarbonisation with consequent emission reduction can only be achieved in the road transport by means of vehicle electrification. Indeed, conventional vehicles, which are based on internal combustion engines (ICE), can be replaced by different vehicle solutions which can be classified on the basis of the electrification level, as follows:

- Battery Electric Vehicles (BEVs);
- Hybrid Electric Vehicles (HEVs);
- Plug-in Hybrid Electric Vehicles (PHEVs)
- Fuel Cell Electric Vehicles (FCEVs)

BEVs and FCEVs can be considered fully-electric vehicle, while the hybrid solutions represent an integration between BEVs and ICE vehicles. They both exploit an electric motor supplied by power converters, but they differ in the storage technology. It is represented by electrochemical batteries for BEVs, while the hydrogen is adopted as energy source in FCEVs and fuel cells realize the conversion in electric power. Depending on the design solution, the ICE can be used for charging the energy storage or even it can be employed for traction in HEVs. On the other hand, a charging plug is provided in a PHEV and both the electric and the traditional powertrains can contribute to the driving of the vehicle.

1.2 Energy storage systems

Energy Storage Systems (ESSs) are technical solutions for capturing and storing energy generated from a variety of sources. They allow energy to be stored and then released when it is needed, rather than being generated and used immediately.
ESS technologies are usually classified in relation to the form of the energy stored, the following are currently the most appropriate solutions:

- Mechanical Energy Storage, which includes Flywheels (FES) and pumped hydro energy storage;
- Electrochemical Energy Storage, including Batteries (BES) and Fuel Cells (FC);
- Electromagnetic Storage, such as Supercapacitors (SC).

Each of them has different characteristics in terms of specific power and energy, and the most appropriate technology will depend on the specific application and the characteristics of the energy source. For instance, batteries are widely used for small-scale applications such as electric vehicles, while pumped hydro is highly prevalent in large-scale energy storage. However, in many cases, a Hybrid Energy Storage System (HESS) is required, which consists of coupling two or more different ESSs in order to efficiently fulfill the application requirements, while guaranteeing the best performance of the system.

In stationary applications, high amounts of energy are required for ensuring the grid support possible during the entire working daily profile. On the other hand, high peak power capability is required when high frequency load and source variability are characteristics of the system. In the case of automotive applications, the system performances are strongly related to the ESS, since it is responsible for efficiency, peak power, maximum speed/torque as well as driving range of Electric Vehicles (EV).

Figure 1.2 depicts the Ragone plot, comparing power and energy densities of main storage technologies. All the available technologies for storage devices substantially differ from each other in their characteristics, in terms of specific energy and power density. Therefore, the best trade-off is pursued depending on the specific application needs. For instance, supercapacitors can provide high power in very short time periods, while fuel cells guarantee high energy with slower discharging rates.

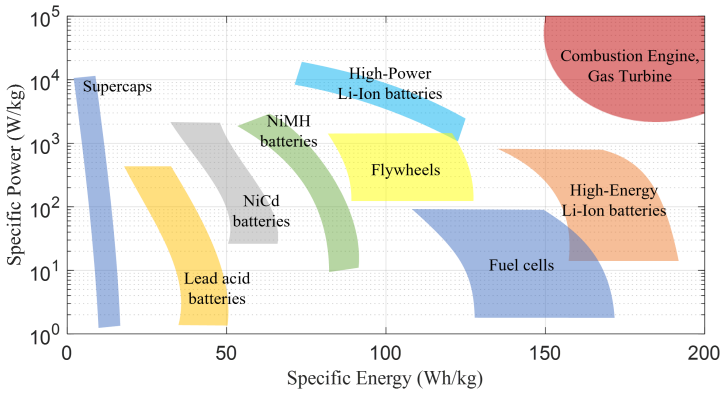

Figure 1.2: Ragone plot of different Energy Storage Systems.

Figure 1.3 shows the typical application fields for ESS and their requirements in terms of energy, expressed as discharge time, and power rating. The applications fields are classified in three topics, as follows.

Energy Management: the main objective is decoupling the generation of electric energy from its instantaneous consumption.

System Services: they include any service that aims to improve and support the quality of energy production and distribution in electric power systems.

Transportation: every kind of electric transport system, including BEVs, HEVs, trains, planes, ships and so on.

As can be deduced from figure 1.3, all the main ESSs applications ideally require a wide range of power and energy, which is hardly fulfilled by a single energy storage technology at the actual state of the art. In many cases, Lithium batteries are chosen as a good trade-off in accomplishing power and energy needs. Indeed, Energy storage systems based on Li-Ion batteries are widely adopted in Hybrid and Electric Vehicles, as well as in stationary applications. However, to fully benefit from system characteristics, in many cases different storage technologies are coupled for enhancing both power and energy density while ensuring safe operation and longer useful life.

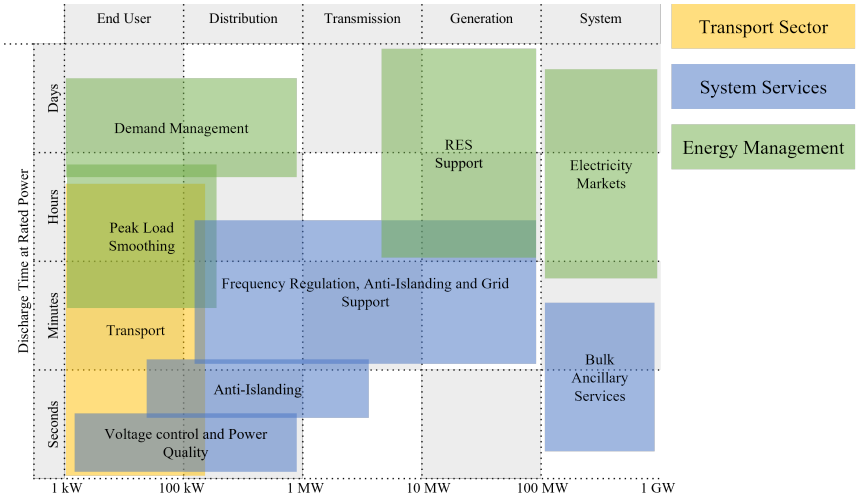

Figure 1.3: Typical applications of ESSs and their requirements in terms of power rating and discharge time [3].

1.3 Battery storage

Battery Energy Storage Systems (BESSs) store the electrical energy under the form of chemical energy. The conversion takes place between the two electrodes electrically separated by a porous electrolyte, which is the means of diffusion of the ions. The discharging phase consists in the migration of electrons from the negative pole (anode) to the positive one (cathode) through a reduction-oxidation (Redox) reaction, while the charging of the battery is obtained by inverting the electrochemical reaction by the electrolyte ionization. The process is limited during the device lifetime, since the nominal capacity and power decrease with the number of executed cycles due to materials and components degradation as well as non-ideal chemical phenomena. Moreover, battery performances are strictly related to the material and realization choices of the involved components. Currently, the most adopted technologies include lead-acid, nickel-based and lithium-ion batteries [4].

1.3.1 Lead-acid Batteries

Lead-acid is a well known battery technology and it is the most common and widely used solution in many application fields, such as

automotive, industrial as well as naval and submarine applications.
A lead-acid battery is typically made of a lead dust anode, a cathode composed of dioxide lead (PbO_2) and a sulphuric acid (H_2SO_4) electrolyte. It represent the cheapest and most mature battery chemistry and it can be designed to withstand frequent charge/discharge cycles (deep cycle batteries mostly used in Uninterruptible Power Supplies) or to provide high amplitude inrush currents for very short time periods (shallow cycle batteries mostly used in automotive applications as combustion engine starters). However, main disadvantages are low energy and power densities, decrease of performances at low temperatures and limited number of life cycles.

1.3.2 Nickel-based Batteries

Nickel-based batteries present many advantages if compared to lead-acid technologies, such as higher power and energy density, longer useful life and lower self-discharge. Typically, these batteries have a cylindrical structure and they can be distinguished in different types depending on which material is considered for the negative electrode. Main nickel batteries are represented by nickel-cadmium (NiCd) and nickel-metal-hydride (NiMH). Despite the use of Cadmium which is a toxic heavy metal, NiCd technology is the most common. However, in many applications they have been totally replaced by the NiMH batteries, which are more robust, reliable and environmental friendly. Main disadvantages include the complexity of manufacturing the metal-hydride component and the higher cost compared to lead-acid batteries.

1.3.3 Lithium-ion batteries

Lithium batteries structure include a negative electrode composed by graphite active material while the positive one is typically made of metal oxides. An aluminum and a copper current collectors for the positive and negative terminals, respectively, are located in contact with the active materials. Between the two electrodes a porous electrolyte acts as separator and allows the migration of lithium ions. Depending on the direction of the ions flow towards the electrodes, the charging or the discharging can occur in the battery [5].
The Lithium-ion technology is considered the most promising to allow larger integration of storage devices in electric transport and stationary applications [6]. A few characteristics of these batteries that make

them highly attractive can be summarized as follows:

- the variety of cell shapes and materials adopted in batteries realization result in high design flexibility, making them suitable for a wide application range;
- Thanks to different design solutions and research progress in material innovation, high energy or high power density can be achieved in order to satisfy high performance requirements;
- the cell voltage level of the basic battery element, approximately of 3.7 V, is the highest among the chemistries available, which allows for reducing the number of series-connected cells in a battery pack.

Despite the high power/energy and efficiency characteristics, the technology is improving year by year and incremental improvements are commonly seen in disruptive battery technologies [7]. However, its full potential is still unexplored. In the recent years, many efforts were made in designing new battery technologies and developing innovative materials in order to achieve higher performances in many applications. In particular, BESSs and HESSs for automotive and stationary applications usually require high energy and high power at the minimum possible volume and weight.

Major concerns about this technology are related to safety issues. Indeed, damages to the internal components, caused by elevated temperatures or overcharge/overdischarge conditions, can lead to gases release and potential thermal runaway. Moreover, battery packs are made by a large number of series and parallel connected cells. Therefore, a battery management system is always needed for monitoring the entire pack and ensuring highest performances in safe operating conditions.
For a better understanding of the advantages as well as the limitations of the current technology, a detailed knowledge of battery features is needed. In the following, an overview of the general terminology used to describe battery characteristics is introduced. These characteristics are usually adopted for defining the performance and properties of the batteries.

Capacity

The nominal capacity represents the maximum amount of energy that can be stored in a battery expressed in Ah. Typically, it is defined as the amount of coulombic charge that can be drawn from the device

starting in full charge down to full discharge condition at nominal or lower current value. It can also be indicated as an energy amount, by roughly multiplying for the nominal voltage, obtaining a Wh or kWh value.

C-Rate

The C-Rate is the normalized value of the charge or discharge current referred to its nominal capacity expressed in Ah. It is defined with the expression xC where x is the ratio between the current amplitude and the nominal capacity.

Terminal Voltage

The voltage measured between the positive and negative terminals of the battery, while a load or a charger is connected, is defined as terminal voltage. It is strictly related to cell parameters and operating conditions, such as temperature, current amplitude and state of charge.

Open-circuit Voltage

The Open-circuit Voltage (OCV) is the battery voltage detected in no-load condition and when a consistent rest period is respected. Measuring the OCV is not a straightforward task and may require high precision measurement tools. Moreover, the duration of the needed resting time, before the measure is considered reliable, depends on many factors, including the chemistry of the device and the applied current amplitude, and ranges from several minutes up to some hours.

State of Charge

The State of Charge (SoC) of a battery provides an indication of the actual stored energy expressed as a percentage of the nominal capacity. It is one of the most important information for safety purposes and it is usually derived by integrating the measured current over time and dividing it by the rated capacity. However, since non-ideal conditions negatively affect this measurement, more advanced methods, such as state observers, are usually required. More details will be illustrated in section 3.

Depth of Discharge

The Depth of Discharge (DoD) represents the amount of energy that has been discharged from the battery and it is expressed in percentage of the nominal capacity. Substantially, it is the complement of the SoC.

State of Health

The State of Health (SoH) is an indication of the remaining useful life of the battery compared to the end of life condition. The latter is defined as the point in which the device cannot fulfill anymore the performance requirements for the specific application. Usually, it is assumed to be related to the capacity or internal parameters of the adopted model of the battery, since it is not directly correlated to physical properties, and a wide variety of estimation methods can be found in literature.

Cut-off Voltage

The cut-off Voltage is declared by the battery manufacturer and it is the minimum allowable voltage value at which the device can be operated. It represent a strict limit for the cell under which several damages to the elementary components of the battery can occur.

1.3.4 Cell structure

The basic unit of an electrochemical battery is the cell, in which the chemical reactions generating electric power take place. Lithium-ions cells are characterized by a wide design flexibility which allows for implementing the optimal solution for the specific application requirements in terms of energy and power density as well as physical distribution in the battery pack geometry. Moreover, a large variety of materials can be adopted for the cell components, which accounts for the overall battery performances. However, in order to promote a deeper electrification of the road transport sector and likewise encourage the introduction of BESS and HESS in stationary applications, further technological progress is needed. Indeed, the development of improved lithium-ion cell components is still a topic of interest in the research field.

1.3.4.1 Design solutions

Figure 1.4 shows the cylindrical, prismatic and pouch designs, which are the main manufactured Lithium-ion battery formats on the market [8].

Cylindrical

The cylindrical shape is widely adopted in cell design thanks to its low cost and long life with good cycling capabilities. In addition, it is characterized by an easy manufacturing process and by a good

(a) (b) (c)

Figure 1.4: Formats currently available on the market for Lithium-ion cells: (a) cylindrical, (b) prismatic and (b) pouch.

mechanical endurance. However, despite cylindrical cells allow for high flexibility in assembling battery packs, their space cavities and their weight lead to low package and energy densities. For safety reasons, these cells usually incorporates a pressure relief mechanism, which breaks up at high pressure, and a resealable vent with a spring-loaded valve which opens to relieve pressure. Moreover, they can present a Positive Thermal Coefficient (PTC) switch, which heats up and interrupt the power flow at high currents, acting as a short circuit protection.
The most popular package of cylindrical cells is the 18650, while other formats include the 20700, 21700, 22700 and 26650. They all differ from each other in rated quantities, such as the nominal capacity.

Prismatic

Prismatic cells have a layered structure and they are commonly wrapped in aluminium cans. Thanks to the manufacturing process, they make an optimal use of the space inside the package. They present a liquid electrolyte and the case provides rigidity to the cell and it include terminal connections and a vent plug. There are no standard packages for this format and each manufacturer adopts custom designs to fulfill the specific application needs. Despite a low energy density due to the packaging, these cells are characterized by high robustness and reliability. Moreover, they can be packaged in large battery packs commonly adopted for EVs and heavy duty vehicles.

Pouch

Pouch cells are integrated in soft laminated cases, which lead to a thin form factor. Terminal connections are made by wide conductive tabs welded to the electrodes which present low series resistance.

This enables the cell to be charged and discharged at higher current rates with respect to other cell formats. Despite the low mechanical strength and the need for an external housing for protection, these cells represent the more flexible and lightweight solution in battery pack designs. However, major concerns are related to the excess swelling due to gassing. In case of overcharge or overheating, gasses are released and the cell may expand causing a separation of the internal layers. Pouch cells are widely adopted in low power and energy devices, such as smartphones, tablets and laptops thanks to their form factor, but they result very suitable for EVs as well, thanks to their high power capabilities.

1.4 Supercapacitors

Differently from battery technology, supercapacitors store the electric energy in an electromagnetic process. Also known as Double-Layer Capacitors (DLCs), they are made by two conductive electrodes, acting as anode and cathode, separated by a thin insulating material, known as dielectric. A static charge is accumulated by means of ions at the interface between electrodes and the dielectric when energy is stored in the device. They result in higher rate capability for fast charging/discharging, when compared to other storage technologies, and lower energy density. Moreover, compared to batteries, supercapacitors (SC) present a longer useful life in terms of the maximum number of charging/discharging cycles, which can be operated at higher current rates without degrading the device's performance. As a result, many research efforts are made in developing high energy density supercapacitors, which represent an attractive technology in many high-power applications [9]. Moreover, recent developments have been directed in improving performances and efficiency of SCs, with the aim of making them more competitive in comparison to other storage systems. At the actual state of the art, they can be adopted as a single power source or in combination with other chemistries for improving power efficiency or useful cycle life of the system [10]. Indeed, SC are often used in applications that require quick bursts of energy, such as in regenerative braking systems in electric vehicles, and in wind and solar power systems. A crucial task in designing SC modules for widespread applications is represented by the possibility to reach an adequate energy density while ensuring acceptable size, weight and cost.

1.5 Hybrid Energy Storage Systems

Hybrid energy storage systems (HESSs) are systems that combine two or more types of energy storage technologies to take advantage of the strengths of each individual component. By combining different types of storage, a hybrid system can improve overall performance and reduce costs compared to using a single type of storage [3]. Indeed, many applications require both power and energy, but none of the energy storage technologies can provide us with high power and energy density at the same time. As a consequence, it is applicable that a hybrid system consisting of two ESS is introduced to take advantage if the strengths of different technologies, improving the useful life of the overall system as well [11]. HESS solves the problems faced by alternative single-energy storage systems regarding simultaneously meeting the needs of high specific power and high specific energy. Moreover, it helps reduce the battery's size and increase its lifespan. Several hybrid configurations have been proposed in literature, which mostly consist of the combination of two or more BESS characterized by complementary features. Alternatively, different storage technologies can be joined allowing for high performances in terms of both energy and power capability.

One of the major concerns for HESS is related to the integration and optimal sizing of the system. The design of an HESS is usually a difficult task, since the system development is based on specific application-related requirements and many different features are considered in finding the best tradeoff. Moreover, the energy management represents a crucial task to be taken into account, since the positive features of each involved ESS have to be exploited in order to properly operate the HESS and much research has been done on improving this aspect [12, 13]. Moreover, many state conditions, such as State of Charge (SoC) and State of Health (SoH), have to be monitored for ensuring the highest performances and safe operating conditions [14, 15].

1.5.1 Automotive application

In the past decades, the increase of interest in the environmental problem made the decarbonisation and emission reduction from transport sector one of the main targets to be addressed in the very close future. The ambition of EU in substantially reducing greenhouse gas emission made the electrification of transport sector one of the main aims for achieving net-zero CO_2 emissions by 2070. Moreover, gov-

ernments around the world are promoting the use of electric vehicles through incentives and regulations to reduce greenhouse gas emissions and dependence on fossil fuels.
Electrification of road vehicles plays a critical role in reducing emissions from the transportation sector. However, it is a constantly technologically advancing sector and innovations are still needed to make Electric Vehicles (EVs) the actual replacement option for traditional vehicles.
Currently, alternative options to conventional transports include:

- Battery Electric Vehicles (BEVs), which are powered solely by an electric motor and battery. They do not have an internal combustion engine or a fuel tank, and must be recharged by plugging them into an electric power source;

- Hybrid Electric Vehicles (HEVs), which combine an internal combustion engine with an electric motor and battery. The electric motor is used to assist the internal combustion engine, and the battery is recharged through regenerative braking and by the internal combustion engine.

- Plug-in Hybrid Electric Vehicles (PHEVs), which present the same HEVs structure, but the battery can be recharged by plugging it into an electric power source. The electric motor can power the vehicle for a certain distance before the internal combustion engine needs to take over.

- Fuel Cell Electric Vehicles (FCEVs), including a hydrogen fuel cell to power the electric motor. They have a very long range compared to BEVs and they produce zero emissions.

However, according to the Ragone plot shown in figure 1.2 , the same energy and power density levels of traditional combustion engines cannot be reached by the capabilities of current energy storage technologies, but in most cases the best solution can be identified to meet the necessary requirements of the case. The most promising devices are Lithium-ion batteries, since they represent a reasonable choice to fulfill the EV goal in matching the necessary electric power and vehicle acceleration, while ensuring a good driving range. However, in many applications regarding high performance EVs, both high power and high energy capability are needed from the ESS. For this reason, HESSs are becoming increasingly popular in the automotive field, as they can improve the performance and efficiency of Electric

Vehicles (EVs) and Hybrid Electric Vehicles (HEVs), and reduce the overall cost of the energy storage system as well.
Most common solutions include the combination of hydrogen fuel cells or flywheel storage systems with lithium-ion batteries. The latter considers the battery for long time energy storage and the flywheel for short-time power burst, while the first solution makes use of high power batteries for overcoming fuel cells weaknesses. In addition, a widely adopted HESS for EVs combines an high energy battery pack and a supercapacitor module. The battery provides energy reservoir over a long period of time in this case as well, while the SC allows for delivering high power burst during acceleration and regenerative braking. The same solution is commonly adopted in stationary applications as well. The main purpose is the exploitment of the SC higher rate capability and the battery higher energy reservoir, while improving the overall system lifetime.

1.5.2 Stationary applications

In the past decades, the electric energy generation system experienced substantial changes. Currently, fossil fuels are still the primary source of energy worldwide, but there has been a significant shift towards renewable energy sources in recent years due to concerns about climate change and the need to reduce greenhouse gas emissions. Solar and wind power in particular have seen a rapid growth and are becoming increasingly cost-competitive with fossil fuels. The high penetration of Renewable Energy Sources (RESs), along with the increasing complexity of energy generation infrastructure, introduces new challenges in grid management such as frequency and voltage regulation for grid stability. HESSs represent the best candidates for facing these issues while managing the increment in global energy demand. Moreover, there is more and more interest in energy storage technology that allows for storing the energy generated during peak production to use it during peak consumption. In the same way, as the cost of renewable energy has decreased, there is more focus on reducing consumption through energy efficiency measures and conservation programs.
ESSs experienced a growing interest in shaping the future of energy and electrical sectors. Batteries can provide long-duration energy storage for grid support, such as peak shaving, load leveling and renewable integration. They can store energy generated during periods of low demand and release it during periods of high demand. Lithium-ion

batteries are widely used in stationary applications due to their high energy density, long life, and ability to handle deep discharge cycles. On the other hand, supercapacitors can provide fast response for frequency regulation and support the grid during periods of high power demand, thanks to their ability to rapidly charge and discharge. They can also handle many more charge/discharge cycles than batteries, which means they can be used more often without suffering from degradation. Furthermore, when SCs and batteries are used together in stationary applications, they can provide a combination of fast response and long-duration energy storage. Supercapacitors can provide quick bursts of energy when the grid is under stress, while batteries can provide long-duration energy storage to help smooth out the supply of energy to the grid.
Other common applications of hybrid energy storage systems in stationary for grid support include combinations of flywheels and batteries, fuel cells and lithium-based ESSs as well as lithium-ion batteries and compressed air energy storage. Overall, HESSs can provide a variety of services to the grid, such as frequency regulation, peak shaving, and renewable integration, and can improve the overall performance and efficiency of the system and reduce the overall cost. Moreover, they can be used for both residential and commercial applications, other than grid-scale energy storage projects.
Some major concerns about HESSs for stationary applications can be summarized:

- complexity increase in comparison with traditional storage systems;
- reliability decrease in comparison with traditional systems due to the use of multiple components;
- battery degradation over time;
- compatibility issues with some types of RESs or existing electrical infrastructure;
- scalability, which can be challenging in order to meet changing energy demand;
- energy management is not a straightforward task and more advanced management systems are required to optimize performances of the system.

Chapter 2

Power Converters for Storage Systems

Power converters are integral part of the system in applications requiring high performance and reliability, such as high-power charging stations for EVs and stationary BESS topologies [16]. In both application fields, high efficiency, bidirectional power transfer and input/output galvanic isolation are the main requirements.
In this chapter, an overview on different DC-DC power converters applications is reported, focusing on automotive and stationary applications for grid ancillary services. Then, the main topologies commonly adopted for Battery and Hybrid Energy Storage Systems are discussed. The operating principle of bidirectional isolated converters is highlighted as well.

2.1 Applications of DC-DC Converters

2.1.1 Automotive Applications

In electric vehicles, power converters play a crucial role in converting the energy stored in the battery pack to the power needed to drive the electric motor. They are also responsible for managing the flow of energy between the battery and the grid during the charging phase. In many cases, such as Vehicle to Grid (V2G) applications, bidirectional high power and high efficiency converters need to be considered to permit the highest level of flexibility, while ensuring optimal performances, in power and energy management [17–19].

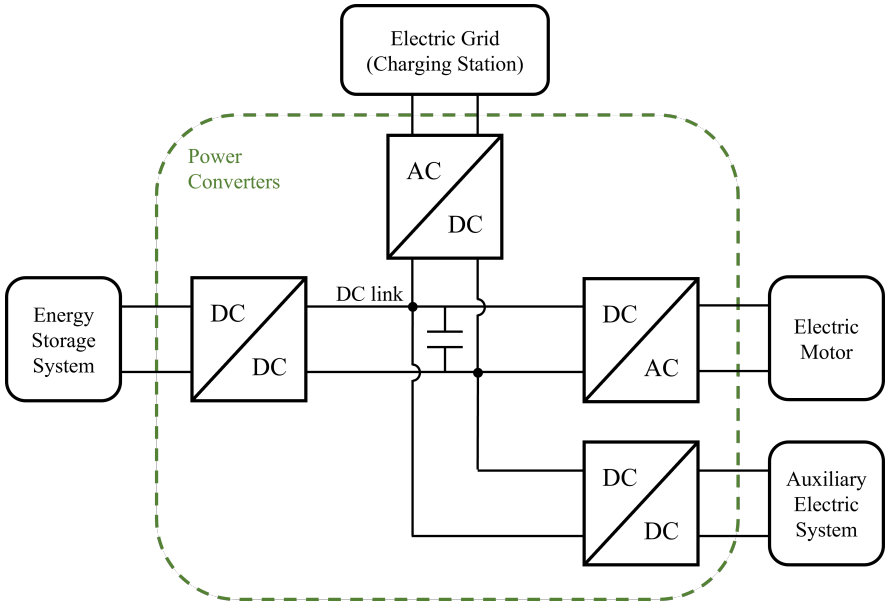

Figure 2.1: Simplified block diagram of an EV electric power system.

Figure 2.1 depicts a typical architecture of a powertrain for EVs, highlighting the involved power converters. It is composed of an AC/DC charger, a DC/AC traction inverter and a bidirectional DC/DC converter for adapting the storage system voltage and power levels to the DC link of the powertrain. The AC/DC charger allows for recharging the battery pack of the BEV or PHEV by interfacing it to the grid. The implementation of a bidirectional DC/DC charger can be considered for V2G technology enabling, which allows the EV to provide additional ancillary services to the grid while improving the charging performances [20, 21].

2.1.2 Stationary Applications

In stationary applications, the power converter is the interface between a storage unit and the electric grid, usually involving up to tens of MWs at medium voltage level [22]. The involved power electronics enable the power and energy sharing from the storage to the grid and vice versa, while ensuring fast response and effective grid support. As a matter of fact, it plays a decisive role in providing high performance service in mitigating the power system challenges, such as voltage instability, frequency fluctuation and load-following [23].

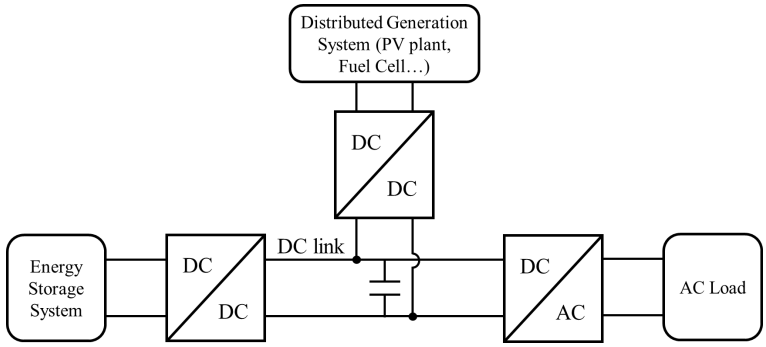

Figure 2.2: Simplified architecture of a distributed generation system.

Most common applications include residential back-up energy storage and small distributed power plants. Figure 2.2 shows a typical architecture of a distributed generation system involving an ESS. The storage is commonly adopted for peak power support during load and supply transient variations. The generation system employs an unidirectional power conversion, whereas the grid supporting BESS require a bidirectional DC-DC converter to enable both charging and discharging operation [24].
The power source and the battery systems are connected to a high-voltage DC-link and different converters are usually considered to maintain a constant bus voltage. The battery is designed with relation to the involved power levels. For high power applications, high voltage batteries are usually adopted to lower the currents expected in the system. On the other hand, when the power level is lower than 5 kW, a low voltage battery may be chosen. In that case, the input/output isolation has to be guaranteed by the converter due to the large voltage ratio between the battery and the DC-link voltage [25].

2.1.3 Hybrid Energy Storage Systems

When different kind of ESSs are integrated to obtain an HESS, the increase of complexity leads to different solutions for the DC/DC converters to interface each storage technology. In particular, the interconnection topology is responsible for flexibility of the system, dynamic performance, efficiency and lifetime of the involved ESSs [26]. As shown in figure 2.3, on the basis of their interconnection, the possible topologies can be distinguished in passive, semi-active and active connection.

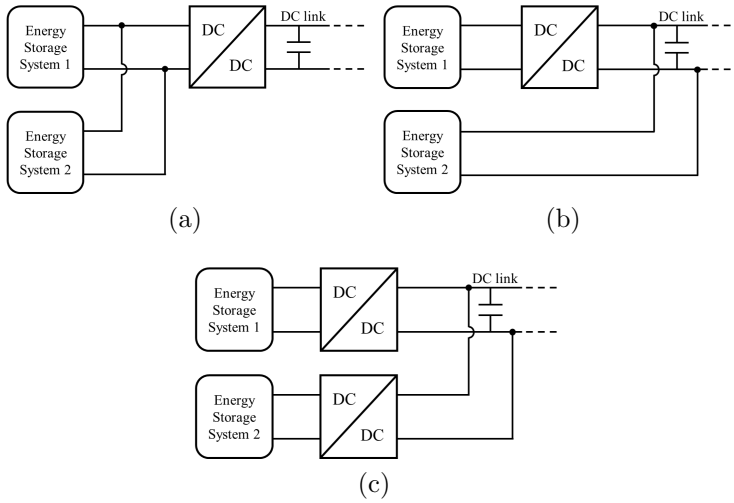

Figure 2.3: Topologies of Hybrid Energy Storage Systems: (a) passive interconnection, (b) semi-active interconnection and (c) active interconnection.

Passive connection

The passive topology involves a direct connection between the different storage components without considering any conversion stage in between them. It can be actuated when the ESSs present the same voltage level and represent the simplest system architecture, since the power allocation between each device is only dictated by their own electrical impedance. For instance, the lower impedance of a supercapacitor with respect to a battery allows it for providing peak power while the battery accounts for energy supply. However, the advantages coming from the ESS hybridization are not fully exploited due to the low flexibility in the system and the DC-DC power converter has to be designed to manage both the high power and high energy from the two storage systems.

Semi-active connection

The semi-active topology involves a single converter for interfacing one ESS to the DC bus, which is adapted to the voltage level of the other device directly connected to it. In this case, the energy management system is in charge of controlling the power flow to the first ESS, while the remaining part is passively provided from the second device. In that case the conversion stage is designed to handle only the power and energy level of one of the two storages, but it has to cope with a

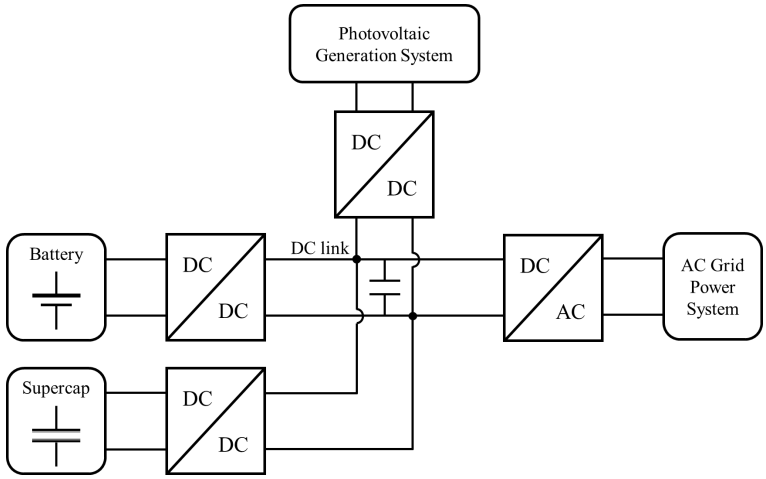

Figure 2.4: Simplified architecture of an active connection Hybrid Energy Storage System implemented in a photovoltaic generation system.

variable voltage level of the DC-link due to the direct connection with the second ESS.

Active connection

The active topology offers the highest level of flexibility since it involves a distinct bidirectional DC/DC converter for each ESS involved in the system. As a consequence, each conversion stage is appositely designed for a specific storage system, enabling the full exploitation of the system performances and characteristics.
HESSs with active connection topology are commonly employed in Renewable Energy Sources (RES) power systems [27]. The storage system is adopted to mitigate the variability of the power generation and fast response as well as high efficiency represent the main requirements. Figure 2.4 shows a typical system architecture when a supercapacitor/battery HESS is considered to support a photovoltaic generation system. The energy source only requires a unidirectional DC-DC converter, whereas the storage systems need bidirectional isolated DC-DC converters to cope with the power sharing at different voltage levels.

Despite the higher complexity of the system, the following advantages of the active configuration can be summarized:

- the voltage levels of the involved ESSs and the DC link are independent from each other;
- higher flexibility for power sharing with a wide variety of control strategies to be implemented;
- each power converter is designed for the power level of a specific ESS;
- higher stability and safety levels can be guaranteed with the decoupling of each storage system.

Thanks to its simplicity and lower number of involved components, the semi-active topology is the most common solution adopted in HESSs for EVs [28, 29]. On the other hand, the active topology has been widely implemented in stationary application considering HESSs, since it allows for faster dynamics and higher performance in grid support service [30–32].
Figure 2.5 shows a simplified block diagram of the typical components involved in a DC/DC conversion stage. Input and output filters are needed for providing smooth voltage and current waveforms at the input and output ports of the converter, which means reduced stress on batteries and other components involved in the grid. The DC/AC conversion unit supplies the HF transformer with AC power, which is then rectified by the AC/DC stage to the output port. Push-pull circuits and half-bridge or full-bridge converter are usually employed. The high-frequency AC network incorporates the HF transformer and additional reactive components can be included for enhancing specific characteristics of the converter or employing resonant power transfer.

2.2 Bidirectional Isolated Power Converters

In many applications, such as high-power charging station for EVs and high-performance converters in grid-connected HESSs for ancillary services, the involved power converters are integral part in the system since their characteristics play a crucial role in defining the global dynamics and efficiency. In most cases, high performances and

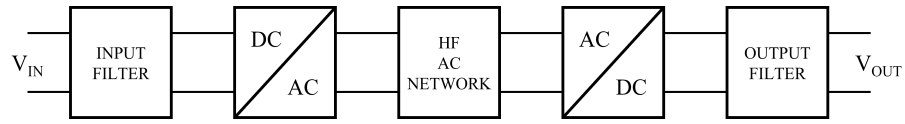

Figure 2.5: Simplified block diagram of an isolated bidirectional DC/DC converter.

reliability as well as bidirectional power flow and input/output galvanic isolation are the main requirements. Best solutions to fulfill these needs consider an high frequency transformer for achieving galvanic isolation, and they can be distinguished in two major groups depending on the adopted reactive network within the HF:

- Non-resonant dual bridge converters
- Resonant dual bridge converters

In non-resonant dual bridge converters, a simple non-resonant reactive component, usually an inductor connected in series with the HF transformer, or the transformer stray inductance itself is typically considered. Two major topologies are worth considering among the non-resonant converters:

- Bidirectional Full-Bridge Converter
- Dual-Active-Bridge Converter

Resonant converters include series or parallel resonant converters, LLC and CLLC converter topologies. Exploiting the resonant characteristic, which guarantee zero current switching thanks to their typical current waveform, these power converters can achieve lowest switching losses and higher efficiencies compared to other topologies. However, the need for additional components and the higher complexity of design and control strongly limit their adoption in real world applications.

2.2.1 Bidirectional Full-Bridge Converter

A bidirectional full-bridge converter is a type of bidirectional DC-DC converter that uses four switches on each side of a transformer to control the power flow between two voltage sources [33]. A typical schematic of the converter is shown in fig. 2.6.

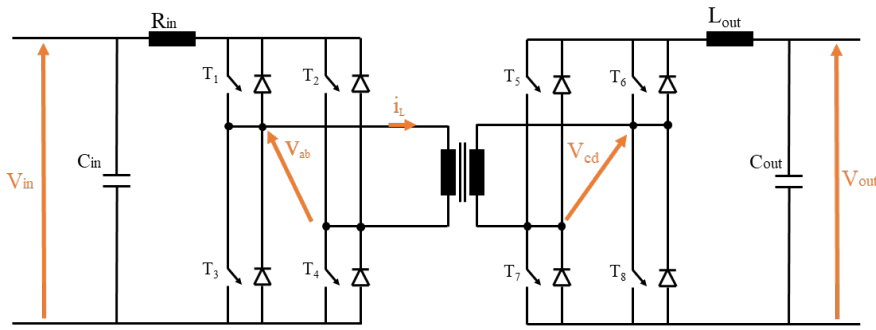

Figure 2.6: Schematic of a Bidirectional Full-Bridge Converter topology.

When the electric power is transferred from V_{in} to V_{out} the input bridge is operated as an inverter to impose an AC voltage on the primary side of the transformer. The transformer only modifies the output voltage amplitude by means of its winding ratio and the output bridge is operated as a diode rectifier by keeping open the four switches T_1, T_2, T_3 and T_4. With a PWM modulation on the input bridge the power can be regulated by means of the duty cycle operated on the bridge legs. The operation mode of the two bridges are swapped when the power flow is inverted, which is easily obtained thanks to the symmetrical structure. It follows that, the converter side working as output port can only be operated at a lower voltage level with respect to the input port and a linear relationship between the PWM duty cycle and the output voltage is obtained, which does not depend on the power flow direction.
Conduction losses can be reduced by operating the rectifying bridge as a synchronous rectifier, leading to higher converter efficiency. Moreover, the device performances can be increased by implementing more advanced control techniques, such as the phase shift modulation [33], while switching losses can be reduced by enabling soft-switching operation [34].
The topology results well-suited for various applications, such as energy storage systems, electric vehicles and renewable energy sources.

2.2.2 Dual Active Bridge Converter

As shown in figure 2.7, the Dual Active Bridge (DAB) converter is composed by two voltage sourced bridges featuring an isolation transformer. Half-bridges can be considered if using a low number

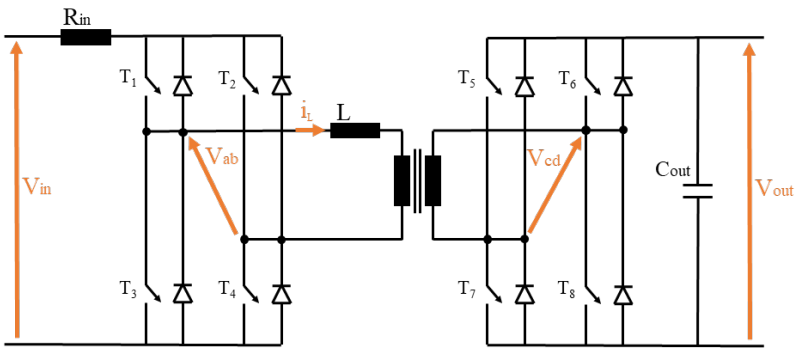

Figure 2.7: Dual Active Bridge converter topology.

of switching devices is a requirement, whit the drawback of lowering the AC voltage levels imposed on the transformer. On the other hand, the use of full-bridges enables the full exploitation of the sources and loads voltage potentials while providing enhanced flexibility for the control strategy and better power regulation.
The input/output galvanic isolation is achieved by the adoption of an insulated high-frequency transformer, which stray inductance is directly involved in the power transfer process. Moreover, an additional inductance in the AC network can be considered for performance enhancement.
Thanks to its capability of transferring high power at high efficiencies, ensuring a bidirectional power flow and providing input/output galvanic isolation, the DAB architecture is one of the most suited solutions in application fields where high efficiency, fast response and safe operation are considered as main requirements [35]. Most common applications include energy storage systems [36], DC distribution and renewable power sources [37], aerospace and automotive applications [38].
Main advantages include the limited number of passive components, the possibility of zero-voltage switching (ZVS) operation over a wide operating range, high efficiency and, therefore, the possibility to achieve high power densities. For enabling power transfer, the DAB utilizes the stray inductance of the HF transformer as reactive network, while an additional series-connected inductance can be considered for enhancing soft switching operation [39]. Moreover, its symmetrical structure easily allow for bidirectional power transfer, maintaining the same characteristics in both directions. Indeed, when the basic modulation technique, known as Single Phase-Shift (SPS) modulation, is consid-

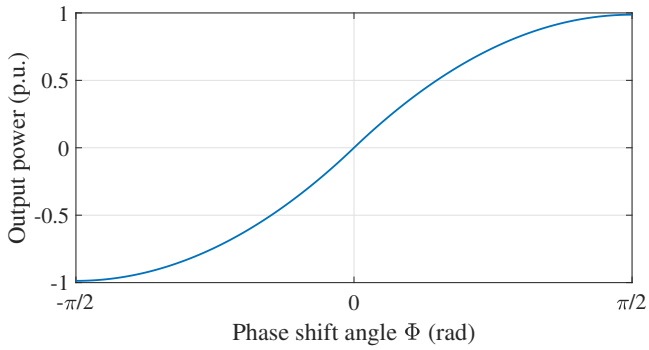

Figure 2.8: Typical power transfer characteristic, in per unit with respect to the converter rated power, for a Dual-Active-Bridge operated under single phase-shift modulation.

ered, the nominal power transfer can be achieved in both directions, as illustrated in figure 2.8.

However, the converter performances are directly related to the operating conditions, and the SPS modulation only provide a limited range of ZVS operation, with consequently decrease of the overall system efficiency. In addition, high RMS current values result in the power components. On the other hand, the adoption of more advanced modulation schemes can lead to current reduction in the HF network, higher efficiency and wider ZVS operating range [40]. Hence, the optimization of both performance and efficiency represents the main topic of interest and several modulation improvements aiming to these objectives have been proposed in literature [41, 42].
Noticeable performance improvements can be achieved if the degrees of freedom are increased the modulation, obtaining a Double Phase-Shift (DPS) [43] or a Triple Phase-Shift (TPS) [44]. Moreover, a proper combination of multiple modulations, related to input/output voltage and power transfer levels, can lead to significant performance increase and component stress minimization. This can be achieved with the implementation of offline predetermined Lookup tables. Otherwise, many solutions for online identifying the optimal modulation have been proposed in literature, such as Sliding Mode Observers (SMO) [45], Artificial Neural Networks (ANN) [46] and Model Predictive Controllers (MPC) [47–49]. Main advantages rely in faster dynamics, optimal utilization of the system with relation to the actual operating point and component stress reduction.

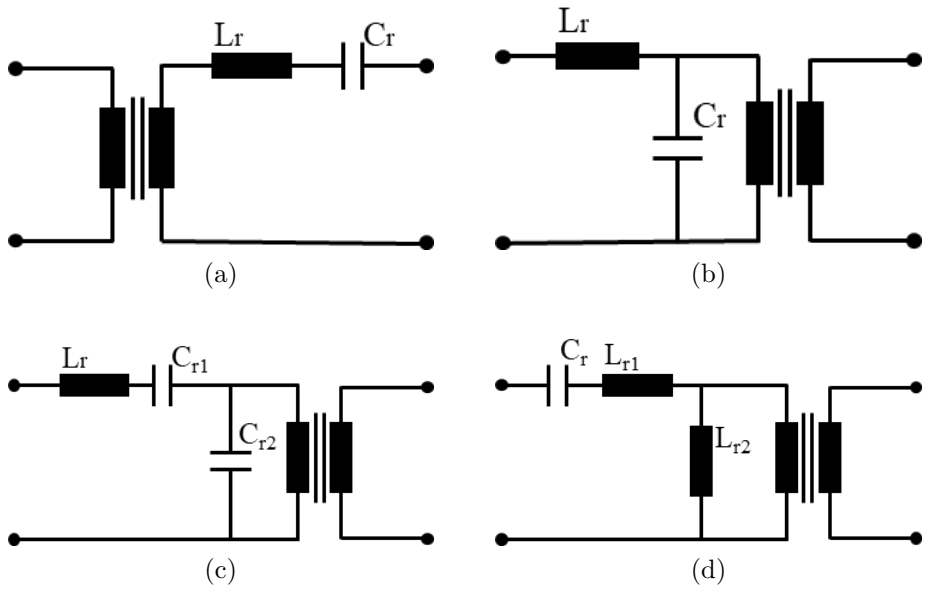

Figure 2.9: Schematic circuits of the reactive networks considered for different resonant DC-DC power converters: (a) Series Resonant, (b) Parallel Resonant, (c) Series-Parallel Resonant LCC and (c) Series-Parallel Resonant LLC networks.

2.2.3 Resonant Isolated DC-DC Converters

The implementation of a resonant network with the high-frequency transformer allows for soft switching operation and thus efficiency improvement. The resonance frequency of the reactive elements is exploited to obtain nearly sinusoidal current in the transformer which leads to a natural turning off of the bridge switches [50]. However, the main drawback is the necessity of operating the converter at variable switching frequency, which depends on the load and on the voltages at input and output ports.

Most popular topologies include the Series Resonant Converter (SRC), the Parallel Resonant Converter (PRC) and the Series-Parallel Resonant Converter (SPRC). They differ from each other by the considered reactive elements and their connection in the resonant network, while the bidirectional functionality is achieved by the implementation of active bridges on both the input and output stage.

The *SRC* resonant network consists in an inductor L_r and a capacitor C_r series-connected to the HF transformer, as shown in figure 2.9(a). The RMS current strongly decreases with the load decreasing [51], but the wide voltage operating range leads to a strong variability of the switching frequency. In addition, high current is experienced at low voltage load, due to the voltage sourced output, and the converter cannot be operated at no load condition since an infinite frequency should be actuated.

The *PRC* resonant tank gives the possibility to control the output voltage even in no load condition. It is composed by a resonant capacitor connected in parallel with the transformer, as shown in figure 2.9(b). High current operation at low output voltage can be improved with the adoption of an inductance in the output filter. However, in this topology, the current in the bridges is not considerably lowered at low power operation. Thus, this converter is not suitable for wide operating power ranges.

The benefits of both the preceding topologies are collected with the adoption of a *SPRC* converter. The resonant network can be made by a single inductor connected to two resonant capacitors, obtaining a LCC converter [52], while a double inductance interconnected to a capacitor is represented by the LLC topology [53], as shown in figures 2.9(c) and 2.9(d), respectively. Low RMS transformer current is achieved at low load conditions and a smaller range of required switching frequency allows for a wider operating range in terms of transferred power compared to the SRC.

2.2.4 LLC Converter

The resonant LLC converter has become increasingly popular in the last years thanks to its high efficiency, low electromagnetic emissions and the possibility to achieve high power density [54]. The bidirectional feature can be enabled by implementing actively controlled bridges on both the input and output stage of the converter, as shown in figure 2.10(a).
When a rectangular voltage waveform is actuated by the input bridge, an approximately sinusoidal current is obtained in the transformer, thanks to the resonant tank of the converter. On the output bridge, Zero-Current Switching (ZCS) is naturally actuated, thanks to the resonant nature of the converter. Furthermore, the output bridge can be operated as synchronous rectifier to further reduce conduction

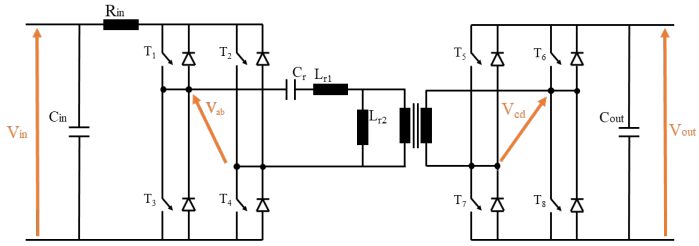

(a)

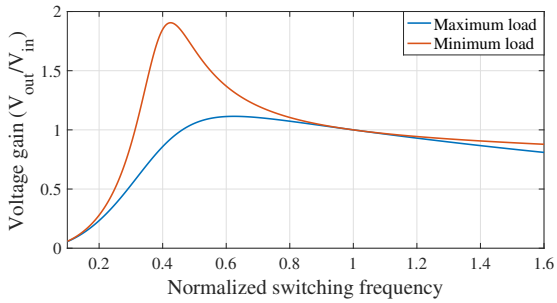

(b)

Figure 2.10: (a) Bidirectional LLC resonant converter topology and (b) typical voltage gain characteristic with respect to the normalized switching frequency at minimum and maximum load condition.

losses and increase the overall efficiency. A typical output voltage gain characteristic is illustrated in figure 2.10(b), which depends on the switching frequency and the load condition. On the other hand, when the converter is operated with a reversed power transfer, the characteristic changes since the inductance L_{r2} is not involved in the resonant tank [55].
Despite the topology results suitable for various applications [56–59], there are still several disadvantages that limit its fully adoption. Indeed, major concerns are related to the control complexity, since it has to be performed at variable switching frequency. In addition, the non-symmetrical structure leads to different transfer characteristic in the bidirectional power transfer and the design optimization cannot be effective for both directions.

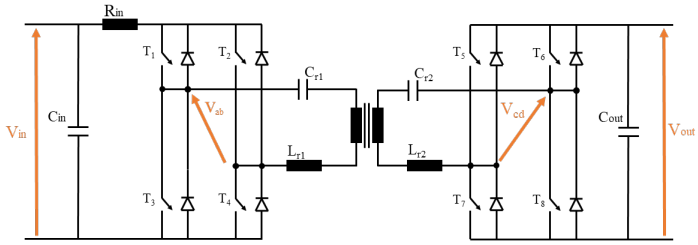

(a)

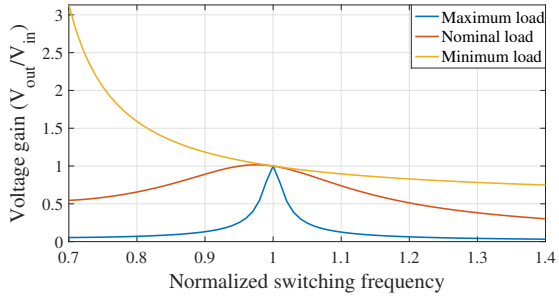

(b)

Figure 2.11: (a) Bidirectional CLLC resonant converter topology and (b) typical voltage gain characteristic with respect to the normalized switching frequency at different load conditions.

2.2.5 CLLC Converter

Uniform characteristics for bidirectional operation are easily ensured with the adoption of a CLLC bidirectional converter.
Different from the LLC topology, in the CLLC resonant tank two LC branches are considered on the primary and the secondary side of the transformer, respectively. As possible to notice from the schematic in figure 2.11(a), the two resonant tank need to be designed by defining two quality factors and two resonant inductance ratios.
A symmetric design is usually adopted to ensure uniform characteristics for bidirectional operation [60]. It consists in making the secondary side LC tank equal to the primary LC components after reflection and it is suitable for small voltage range applications [61]. On the other hand, an asymmetric parameter design can be considered when highly variable and different voltage ranges are expected on the converter input and output ports [62].
A typical characteristic of a symmetrical bidirectional CLLC resonant

converter is shown in figure 2.11(b), which is easy to achieve in both power transfer directions.
As a matter of fact, the design procedure and parameter optimization are not straightforward tasks for this converter and the implementation complexity still represent a consistent issue.

Chapter 3

SoC Estimation Methods for ESSs

In most vehicular and stationary applications, power and energy levels of installed ESSs are exponentially increasing. With the increase of performances, the monitoring tasks performed by the Battery Management System (BMS) become of paramount importance since they include accurate current and voltage measurements, cell voltage equalization and reliable estimation of the State of Charge (SoC) and the State of Health (SoH) in order to ensure safe operating conditions [63].

In BESSs, the accurate knowledge of the SoC helps in correctly defining the power limits of the battery pack and the remaining usable energy during operation. Considering an EV implementation, it results in perfectly knowing the remaining mileage before needing to recharge the ESS. On the other hand, if a HESS for ancillary service is considered, the best power allocation between two or more energy sources with substantial differences in power and energy characteristics is crucial. Hence, the SoC helps in exploiting the fundamental information about the energy and power capability of the device and consequently improving the performances in the HESSs control strategies. Moreover, in all the mentioned examples, it represents a crucial indicator for avoiding hazard conditions, such as overcharge and over discharge. However, due to non-ideal characteristics of the storage devices the SoC cannot be directly observed and its estimation results a challenging task.

In this chapter, the BMS functionalities are introduced and an overview of the main SoC estimation methods is presented. Moreover, the implementation of a state observer for SoC estimation in Lithium batter-

ies as well as in Supercapacitors is presented, including details related to system models and characterization issues.

3.1 SoC Estimation

SoC estimation is one of the most demanding task for the BMS of an energy storage system. From the user point of view it represents an useful information for knowing how much energy is available in the system. Moreover, it allows for performance increasing and guarantees safe operating conditions. However, in many storage devices, including Lithium-ion batteries and Supercapacitors (SC), the SoC information is not directly available due to non-ideal behaviors and time-varying characteristics. Currently, conventional methods can be distinguished from more advanced model-based estimators, which include state observers such as Kalman Filters (KFs), data driven algorithms such as Artificial Neural Networks (ANN) and nonlinear observers such as Sliding Mode Observers (SMO).

3.1.1 Conventional Methods for Battery SoC Estimation

Most common methods for battery SoC estimation include the OCV observation, the Coulomb Counting, Electrochemical models, Internal Impedance Models and Equivalent Circuit Models (ECMs).

OCV Observation

The battery cell presents an OCV characteristic related to the SoC which can be used for online estimating the SoC by observing the cell voltage. The main problem of this method is that the OCV can only be represented by the cell terminal voltage after a long time under no load condition. Therefore, a proper rest time needs to be waited before measuring the OCV, which is hardly suitable during battery operation, especially in high-power applications. Moreover, the OCV-SoC curve is strictly related to the battery chemistry and varies depending on environmental conditions such as temperature and aging conditions of the cell. Hence, time consuming characterization procedures must be taken into account. Moreover, some chemistries, such as LFP batteries, have a very flat characteristic which involves high inaccuracies in relating the SoC to the measured cell voltage.

Coulomb Counting

The Coulomb Counting method is the most adopted solution for battery SoC estimation thanks to its simplicity and low computational cost. It is based on the integration of the pack current over time for evaluating the amount of energy stored or discharged. Therefore, starting from a known initial condition, the actual SoC SoC_{CC} can be easily identified during online operation, as shown in equation (3.1).

$$SoC_{CC}(t) = SoC(t_0) - \frac{1}{3600 \cdot C_n} \int_{t_0}^{t} i(t) d\tau \tag{3.1}$$

where $SoC(t_0)$ is the initial SoC at time t_0, the division by 3600 is needed for converting the integral result in Ah, C_n is the nominal capacity of the cell and $i(t)$ is the measured battery current. Some non-ideal behaviors can be taken into account by introducing the coulombic efficiency η, which can be different in charging and discharging phase, and the self-discharge rate S_d [64], as follows.

$$SoC_{CC}(t) = SoC(t_0) - \frac{1}{3600 \cdot C_n} \int_{t_0}^{t} (\eta \cdot i(t) - S_d)\, d\tau \tag{3.2}$$

The performances of this method strongly rely on the correct knowledge of the initial condition SoC_0, which is not an easy task. It is accurate only in a few operating points such as fully discharged or charged cell. These two cases are rarely met especially in applications involving high dynamics. For instance, in the automotive case, quick charges and discharges are very usual and full charges are rarely executed. Similarly, in stationary applications, the storage system is subjected to rapidly changing currents and it is supposed to provide power supply as well as energy absorbing without prediction, so it is preferred to avoid the extreme values of SoC during operation. Moreover, current measurement errors and noise strongly affect the accuracy of the Coulomb Counting method. Indeed, since the current is integrated over time, the error related to measurement instruments gets increasing during the battery operation until another known condition is met. Moreover, the aging of the device usually results in a capacity fade during lifetime, which should be taken into account for improving the estimation accuracy.

Electrochemical models

Electrochemical models represent the most accurate way to model the behavior of a Lithium-ion battery. With the adoption of partial differential equations, the SoC can be estimated by considering its dependency with the lithium concentration in the positive and negative electrodes. This is the most accurate method for identifying the state of the battery, but it involves a large amount of model parameters to be implemented, thus resulting too complex for online operation.
Alternatively, reduced-order electrochemical models have been proposed in literature to be a good trade-off between complexity and accuracy [65].

Internal Impedance Models

A characteristic curve can be derived in order to relate the internal impedance of a battery to its SoC. The estimation of the internal impedance is made by means of the Electrochemical Impedance Spectroscopy (EIS), resulting in a model including inductances and capacitances over a wide range of frequencies [66]. A simpler approach can be adopted if only the internal resistance is considered, which is calculated by the ratio between the cell voltage and the current variations in DC current pulses. Nevertheless, the characteristics that relate the impedance or resistance to the SoC are less accurate than the OCV-SoC curve and they can be nonmonotonic functions. Therefore, this method is usually unsuitable for real-world applications.

Equivalent Circuit Models

The Equivalent Circuit Model of a battery can be used for online SoC estimation by comparing the model output to the measured terminal voltage. Despite some chemical behaviors cannot be fully represented by circuit elements, ECMs are widely adopted in real-time applications thanks to their good trade-off between model accuracy and complexity [67]. However, two main drawbacks need to be taken into account. Firstly, time consuming experimental tests are required to optimally calibrating the model parameters. Indeed, a proper number of operating conditions, in terms of current profile, ambient temperature and battery aging should be considered to achieve a good modeling accuracy. In addition, the main parameter of the ECMs is the OCV and the disadvantages illustrated for the OCV-SoC method are inherited.

3.1.2 Conventional Methods for Supercapacitor SoC Estimation

Conventional methods for identifying the SoC in a SC include the simple capacity model, the Coulomb Counting method, the OCV observation and the multi-branch Equivalent Circuit Model.

Simple Capacity Model

The simple capacity model calculates the energy from the voltage measured at the device terminals, assuming the supercapacitor behavior to be approximately the same as a classic capacitor with its nominal capacity. In particular, the SoC value is obtained as the ratio between the actual stored energy and the maximum available energy in the device, as shown in equation (3.3). The latter is derived from the nominal voltage and capacity values, while the actual stored energy is derived from the voltage measured at the device terminals.

$$SoC_{simple} = \frac{\frac{1}{2}C_n v_{sc}^2}{\frac{1}{2}C_n V_n^2} = \frac{v_{sc}^2}{V_n^2} \tag{3.3}$$

where v_{sc} is the measured capacitor voltage, C_n and V_n are the rated capacity and voltage values, respectively. This definition is mostly used thanks to its simplicity and easy implementation. However, the supercapacitor non-linear behavior, comprising internal losses and charge redistribution effect, is not taken into account, which inevitably leads to consistent error in SoC tracking.

Coulomb Counting

The Coulomb Counting method is widely adopted for SCs as well. It is based on the same principle adopted for the batteries case, involving the equation (3.1) for SoC computation. Despite the self-discharge can be taken into account and less intense nonlinearities are typical of SCs, measurement issues still impact the SoC estimation and significant errors can be caused by inaccurate knowledge of the initial SoC value $SoC(t_0)$.

OCV

Similarly to the battery case, the OCV of a supercapacitor can be observed to estimate te SoC or to interpolate the initial SoC value

($SoC(t_0)$) and clear the accumulated error in the Coulomb Counting method. Nevertheless, the OCV-SoC relation ignores the typical nonlinear behavior of the supercapacitors, such as the voltage-dependent capacity term. Moreover, even for SCs a minimum rest period has to be waited in order to properly observe the OCV of the device.

3.1.2.1 Multi-branch model

The more accurate indication of the SoC value in a SC can be achieved with a multi-branch model implementation. In detail, multiple R-C branches are considered for representing the nonlinear behavior of the device, and the energy accumulated in the internal modeled capacitors is monitored, as follows.

$$SoC_{MB} = \frac{\sum_{i=1}^{n} \frac{1}{2} C_i v_i^2}{E_{max}} \tag{3.4}$$

where n is the number of internal states included in the model, C_i and v_i are the modeled internal capacitance values of the SC and the voltage across them, respectively, and E_{max} represents the characterized maximum energy considering all the internal states.
Despite this method is characterized by high accuracy in SoC estimation, the internal voltage and capacity states of the SC are not physical quantities easy to reach. Indeed, an additional algorithm should be considered to estimate the internal voltages.

3.1.3 Kalman Filtering Methods

Among all the SoC estimation methods, state observers allow for overcoming the issues of conventional methods. In particular, in the past few years much research has been done on the model-based KFs, which have become a commonly adopted solution. The main features that support their adoption include the unneeded knowledge of the initial state of the battery and their robustness to measurement noise and errors.

3.1.3.1 State Estimation

The state estimation is the process of extracting information about quantities which are not directly available by exploiting the measurable inputs and outputs of the system.

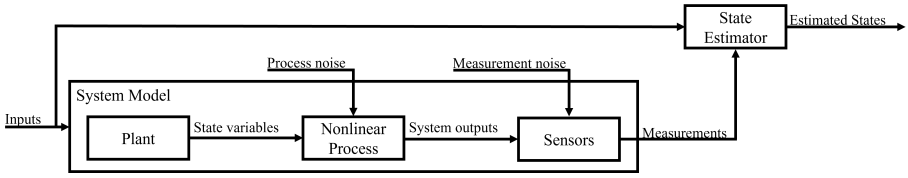

Figure 3.1: Simplified block diagram of a state estimation process.

As shown in figure 3.1, a model-based state estimation needs knowledge about the system model and information about measurement noise. The measurement represents the output of the system, which is a function of the input and one or more state. Moreover, the effect of the past behavior is included in the system states.

A linear system model is usually represented by discrete-time state-space equations, as follows:

$$\begin{cases} x_{k+1} = A_k x_k + B_k u_k + q_k \\ y_k = C_k x_k + D_k u_k + r_k \end{cases} \tag{3.5}$$

where x_k is the state vector, u_k is the input vector, y_k represents the measurable output, while q_k and r_k represent the process and measurement noises, respectively.

If the system is hardly represented by a linear model, a discrete-time nonlinear equations system must be considered. It is composed by a process function $f(\ )$ and a measurement function $g(\ )$:

$$\begin{cases} x_{k+1} = f\left(x_k, u_k\right) + q_k \\ y_k = g\left(x_k, u_k\right) + r_k \end{cases} \tag{3.6}$$

where u_k is the known input of the system, y_k represents the measurable output, while q_k and r_k represent the process and measurement noises, respectively. q_k and r_k are assumed to be zero-mean white Gaussian noises with covariance matrices Q_k and R_k, respectively.

3.1.3.2 Linear Kalman FIlter

The Kalman Filter is an optimal state observer which was introduced in 1960 for state estimation in linear systems [68]. They result unaffected by measurement noise and capable of correcting the initial estimation error [69]. Moreover, since linear models are hardly

Table 3.1: EKF Algorithm.

Prediction
Computation of A_k and C_k
$x_k^- = f(x_{k-1}^+, u_{k-1})$
$y_k^- = g(x_k^-, u_k)$
$P_k^- = A_{k-1} P_{k-1}^+ A_{k-1}^T + Q$
Update
$K_k = P_k^- C_k^T \left[C_k P_k^- C_k^T + R_k \right]^{-1}$
$x_k^+ = x_k^- + K_k \left(y_{mk} - y_k^- \right)$
$P_k^+ = P_k^- - K_k C_k P_k^-$

applicable in applications such as lithium batteries and supercapacitors, many nonlinear implementations have been developed in the past years. Main estimators for identifying the SoC in nonlinear systems include the Extended Kalman Filter (EKF), the Unscented Kalman Filter (UKF) and the Square-Root Unscented Kalman Filter (SR-UKF).

3.1.3.3 Extended Kalman Filter

The Extended Kalman Filter (EKF) involves a first-order Taylor-series expansion for linearizing the system equation, thus resulting an effective solution when strong nonlinearities are not affecting the system.
The linearization consists in Jacobian matrices of the state and measurement functions (3.6) in the nearest of x_k, as follows.

$$\begin{aligned} A_k &= \left. \frac{\partial f(x_k, u_k)}{\partial x_k} \right|_{x=x_k} \\ C_k &= \left. \frac{\partial g(x_k, u_k)}{\partial x_k} \right|_{x=x_k} \end{aligned} \tag{3.7}$$

The Jacobian matrices are iterated at each time step of the algorithm, and the Kalman gain matrix K_k is computed to correct the estimation, as illustrated in table 3.1 [70].

This represents an effective solution to operate a linear filter for state estimation in nonlinear systems. However, strong nonlinearities and inaccuracies in the model may lead to performance decrease and potentially divergence of the filter.

3.1.3.4 Unscented Kalman Filter

The Unscented Kalman Filter (UKF) introduces a deterministic sampling approach instead of linearizing the system model. In detail, it iterates at each discrete time step the true nonlinear state-space equations of the systems, by means of the so-called Unscented Transform [71]. It is based on the propagation of sigma points through a matrix square-root operation, which are used to estimate the state by means of a weighted mean. Table 3.2 depicts the system equations on the basis of the UKF. As possible to notice, considering L the dimension of the state vector, $2L + 1$ sigma points are evaluated.

Table 3.2: UKF algorithm.

Prediction
Sigma points computation
$\chi_{k-1} = \left[x_{k-1} \;\; x_{k-1} + \gamma\sqrt{P_{k-1}} \;\; x_{k-1} - \gamma\sqrt{P_{k-1}}\right]$
$\chi_{k,k-1} = f\left(\chi_{k-1}, u_{k-1}\right)$
$x_k^- = \sum_{i=0}^{2L} W_i^m \chi_{i,k,k-1}$
$P_k^- = \sum_{i=0}^{2L} W_i^c \left[\chi_{i,k,k-1} - x_k^-\right]\left[\chi_{i,k,k-1} - x_k^-\right]^T + Q_k$
$\Upsilon_{k,k-1} = g\left(\chi_{k,k-1}, u_{k-1}\right)$
$y_k^- = \sum_{i=0}^{2L} W_i^m \Upsilon_{i,k,k-1}$
Update
$P_y = \sum_{i=0}^{2L} W_i^c \left[\Upsilon_{i,k,k-1} - y_k^-\right]\left[\Upsilon_{i,k,k-1} - y_k^-\right]^T + R_k$
$P_{xy} = \sum_{i=0}^{2L} W_i^c \left[\chi_{i,k,k-1} - x_k^-\right]\left[\Upsilon_{i,k,k-1} - y_k^-\right]^T$
$K_k = P_{xy} P_y^{-1}$
$x_k = x_k^- + K_k\left(y_{mk} - y_k^-\right)$
$P_k = P_k^- - K_k P_y K_k^T$

In order to ensure good performance, the weights W^c and W^m need to be set properly. Their initialization is usually performed as follows [71]:

$$
\begin{aligned}
W_0^m &= \frac{\lambda}{L+\lambda} \\
W_0^c &= \frac{\lambda}{L+\lambda} + 1 - \alpha^2 + \beta \\
W_i^m &= W_i^c = \frac{1}{2 \cdot (L+\lambda)}
\end{aligned}
\tag{3.8}
$$

with

$$
\begin{aligned}
\lambda &= \alpha^2 \cdot (L+\kappa) - L \\
\gamma &= \sqrt{L+\lambda}
\end{aligned}
\tag{3.9}
$$

where α determines the spread of the sigma points around the mean state value (usually set to 0.5), κ is a second scaling parameter (usually set to 0) and β incorporates prior knowledge of the distribution of the state. In particular, assuming a Gaussian distribution, $\beta = 2$ represents an optimal solution to be considered [72].

Since the set of sigma points is calculated through a square-root operation, the UKF results computationally expensive and the covariance matrices are required to be positive definite for avoiding the divergence of the filter.

3.1.3.5 Square-Root Unscented Kalman Filter

The SR-UKF is based on three linear algebra techniques known as QR decomposition, Cholesky factor updating and efficient least square, which are widely illustrated in [73], leading to an efficient implementation of the square-root operation. In this way, the matrices positive definiteness is guaranteed and the square root of the covariance matrix is recursively updated. This also allows for avoiding the need to re-factorize at each time step, leading to a computationally less expensive algorithm.
As for the UKF, considering L the dimension of the state vector, $2L+1$ sample points called Sigma points are computed in the SR-UKF and iterated according to the algorithm reported in table 3.3 [72].

The matrix S is derived as the square-root of the initial state covariance matrix, as follows:

$$
S = \sqrt{P_0} \tag{3.10}
$$

Table 3.3: SR-UKF Algorithm.

Prediction
Sigma points calculation
$\chi_{k-1} = [x_{k-1} \quad x_{k-1} + \gamma S_{k-1} \quad x_{k-1} - \gamma S_{k-1}]$
$\chi_k = f(\chi_{k-1}, u_{k-1})$
$x_k^- = \sum_{i=0}^{2L} W_i^m \chi_{i,k}$
$S_k^- = qr\left\{\left[\sqrt{W_1^c}\left(\chi_k - x_k^-\right) \quad Q\right]\right\}$
$S_k^- = cholupdate\left\{S_k^-,\ \chi_k(0) - x_k^-,\ W_0^c\right\}$
$\Upsilon_k = g(\chi_k, u_{k-1})$
$y_k^- = \sum_{i=0}^{2L} W_i^m \Upsilon_{i,k}$
Update
$S_y = qr\left\{\left[\sqrt{W_1^c}\left(\Upsilon_k - y_k^-\right) \quad R\right]\right\}$
$S_y = cholupdate\left\{S_y,\ \Upsilon_k(0) - y_k^-,\ W_0^c\right\}$
$P_{xy} = \sum_{i=0}^{2L} W_i^c \left[\chi_{i,k,k-1} - x_k^-\right]\left[\Upsilon_{i,k} - y_k^-\right]^T$
$K_k = \left(P_{xy}/S_y^T\right)/S_y$
$x_k = x_k^- + K_k\left(y_{mk} - y_k^-\right)$
$U = K_k S_y$
$S_k = cholupdate\left\{S_k^-,\ U,\ -1\right\}$

3.1.4 Kalman Filter Initialization

In Kalman Filtering methods, an initial calibration based on system dynamics has to be made to guarantee the algorithm's best performance and robust operation, as illustrated in [74]. Indeed, a calibration of the filters is needed depending on the system dynamics and characteristics. Details on the statistical properties of the process and measurement noises in terms of covariance matrices are required. However, since covariance matrices may also be time-dependent, it results difficult to find a mathematical correlation between the system characteristics and the matrices initialization. Therefore, covariance matrices are typically defined by trial and error methods in numerical analysis. Alternatively, two different approaches can be distinguished for optimally calibrate the initial parameters, including an analytical procedure and a parameter fitting by means of a nonlinear least square solver. In both cases, the measurement noise covariance R, the pro-

cess noise covariance Q, and the initial state covariance S_0, are set as diagonal matrices. This means that only the auto-covariance terms are considered and the involved noise terms are independent of each other.

Analytical equations

The initialization of a Kalman Filter can be achieved by considering practical guidelines to correlate the best available knowledge of the system to the filter parameters [75]. In detail, considering a generic model with n state variables $x_1 \dots x_n$, it results:

$$R = (dE_m)^2 \tag{3.11}$$

$$Q = \begin{bmatrix} (dx_1)^2 & 0 & \cdots & 0 \\ 0 & (dx_i)^2 & & \vdots \\ \vdots & & \ddots & 0 \\ 0 & \cdots & 0 & (dx_n)^2 \end{bmatrix} \tag{3.12}$$

where dE_m is the measurement accuracy and dx_i is the maximum expected variation of the $i-th$ state variable in a complete operating process.
Likewise, considering the initial error ε_{x_i} related to the estimation of the *i-th* state variable, the initial state covariance can be yield as follows.

$$P_0 = \begin{bmatrix} (\varepsilon_{x_1})^2 & 0 & \cdots & 0 \\ 0 & (\varepsilon_{x_i})^2 & & \vdots \\ \vdots & & \ddots & 0 \\ 0 & \cdots & 0 & (\varepsilon_{x_n})^2 \end{bmatrix} \tag{3.13}$$

Parameter fitting

Since the covariance matrices influence the filter convergence and estimation performance, a charging/discharging current profile can be defined for validating their initialization. Therefore, as part of the modeling procedure, an optimal calibration is achieved by fitting the filter estimated state variables onto the ideally simulated ones by means of the "Parameter Estimator" app tool in Matlab-Simulink®. The toolbox implements the nonlinear least square solver for minimizing the error on the chosen model outputs. The obtained parameters

represent the optimal choice for the Kalman Filter initialization in the predefined operating conditions.

3.1.5 Adaptive Algorithm

As mentioned before, the filter performances depend on the process and measurement noise covariance matrices initialization, which is related to the knowledge of system dynamics and statistical properties. However, these parameters are usually unknown and they can change over time. Therefore, KFs performance and accuracy improvements can be achieved with the implementation of adaptive algorithms capable of calculating and updating the noise covariance matrices at each time step. Several adaptive laws have been proposed in literature, including an Adaptive Unscented Kalman Filter (AUKF) based on the output voltage residual sequence of the battery model [76] and an Adaptive Square-Root Unscented Kalman Filter (ASR-UKF) obtained through the integration of the Sage-Husa adaptive filtering algorithm with the SR-UKF [77–79].

Taking into account the adaptive algorithm presented in [76, 80], the covariance matrices can be updated according to the residuals of the output variable estimation, as follows.

$$C_k = \frac{1}{N} \sum_{i=k-N}^{k} (e_i)^2 \tag{3.14}$$

where C_k is related to the covariance of the output residuals at time step k, N is a window size for covariance matching and e is the voltage residual of the battery model at time step k, defined as:

$$e_k = y_{mk} - y_k \tag{3.15}$$

where y_{mk} is the output variable of the system measured at time step k and y_k is the estimated output variable.
In order to integrate this adaptive algorithm to the SR-UKF, the square-root of covariances should be iterated as follows.

$$\begin{aligned} Q_k &= \sqrt{|diag(diag(K_k C_k (K_k)^T))|} \\ R_k &= \sqrt{C_k + \sum_{i=1}^{2L} W_i^c \cdot [\Upsilon_{i,k} - y_{mk}] [\Upsilon_{i,k} - y_{mk}]^T} \end{aligned} \tag{3.16}$$

Moreover, only the absolute value of the main diagonal needs to be considered in the updating step of Q for ensuring the positive definiteness of the matrix. The integration of such adaptive law with the SR-UKF leads to an Adaptive Square-Root Unscented Kalman Filter (ASR-UKF), which results unaffected by the typical Kalman Filter initialization issue.

3.2 Kalman Filter Implementation

3.2.1 Kalman Filter for Battery SoC Estimation

Kalman Filters are optimal state observers and have been proven to be highly suitable in Li-Ion batteries state of charge estimation. Nevertheless, their performances are strongly affected by the accuracy of the battery model adopted for carrying out the SoC estimation [74]. In this section, an overview on battery modelling approaches and their challenges is reported.

3.2.2 Battery Models

The development of an accurate battery model is a crucial task for the design of a reliable SoC estimator. Indeed, numerical results from battery models allow for achieving reliable information about non measurable variables, such as SoC and SoH.

Many variants of battery models can be found in the literature, differing in complexity and accuracy [81,82]. They can be classified in four main categories: electrochemical, mathematical, black-box and equivalent circuit models.

3.2.2.1 Electrochemical Models

Electrochemical models are the most accurate for representing the electrical behavior of Lithium-ion batteries. Indeed, they provide the highest accuracy in describing the electrochemical processes that take place inside the cell. They make use of nonlinear partial differential equation for describing the transport, thermodynamic and kinetic phenomena inside the cell, on the basis of porous electrode theory and concentrated solution theory [83].

The electrochemical models are particularly useful in the design process of battery cells but they result in high complexity since de-

tailed knowledge of the battery chemistry is needed to achieve high accuracy. Despite reduced order electrochemical models have been proposed to reduce model complexity [65], these models are hardly suitable for real-time state estimation applications.

3.2.2.2 Mathematical Models

Mathematical models describe the battery cell behavior by means of analytical or stochastic approach. They are characterized by a set of equation and they can be distinguished in Kinetic battery models and stochastic cell models [84,85]. Complexity is still a concern with these models and they are usually adopted for very specific applications.

3.2.2.3 Black-Box Models

Black-box models reproduce the behavior of the cell without looking into the physical or electrochemical processes acting inside the device. Indeed, these models consider the battery as an unknown box and Artificial Intelligence (AI) techniques are applied to establish a relationship between the inputs and outputs of the system. Most commonly adopted AI techniques include Artificial Neural Network (ANN) [86], Fuzzy Logic (FL) [87] and Support Vector Machine (SVM) [88]. These approaches need training procedures to capture the system behavior with the use of large sets of data. In order to achieve high model accuracy, the dataset should cover a wide operating range and large amount of experimental data is required. However, the data acquisition results in time consuming processes and the reproduction of a wide range of operating conditions is not immediate, especially in high-energy and high-power battery cells.

3.2.2.4 Equivalent Circuit Models

Equivalent Circuit Models (ECMs) aim at reproducing the nonlinear behavior of electrochemical cells by means of lumped circuit components. Once the circuit topology is defined, the model parameters can be properly characterized to represent the dynamics of any kind of battery chemistry, resulting in high flexibility for a large number of different applications. As shown in figure 3.2, starting form a simple circuit involving a few number of constant parameters, the model complexity can easily be increased up to the needed accuracy level. For instance, the number of circuit components can be increased and parameter variation over time or environmental conditions can be

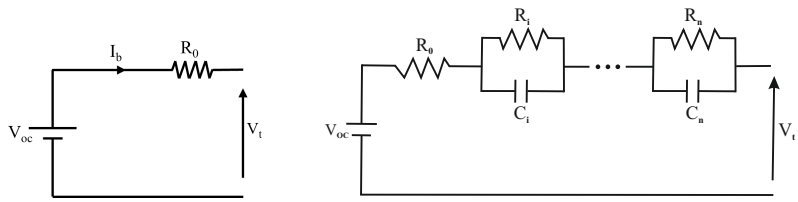

(a) (b)

Figure 3.2: (a) Zero-order and (b) n-order Equivalent Circuit Model for electrochemical batteries.

taken into account. Therefore, they allow to reach the best trade-off between complexity and accuracy depending on the specific needs of the application. Thanks to their easy implementation and relatively low computational cost as well as limited number of parameters to tune, ECMs are widely adopted in Battery Management Systems and in state estimation tasks.

Figure 3.2 depicts a zero-order ECM and a generic n-order model, obtained by increasing the number of dynamic elements in the circuit. The voltage source V_{oc} represents the SoC-OCV characteristic, and the zero order ECM only include a series resistor R_0 to represent the cell voltage response. The optimal trade-off between complexity and accuracy is commonly found in second-order ECMs, which is typically needed for reproducing the cell dynamics.
Including in the model the Coulomb Counting equation to represent the SoC behavior, the generic model equations for a generalized n-order ECM can be worked out as follows:

$$\begin{cases} SoC = SoC(t_0) - \dfrac{1}{3600 \cdot C_{Ah}} \displaystyle\int_{t_0}^{t} I_b(t)\, dt \\ \dfrac{dv_i}{dt} = -\dfrac{v_i}{R_i C_i} + \dfrac{I_b}{C_i} \qquad \forall\ i = 1...n \\ V_t = V_{oc} - R_0 \cdot I_b - \displaystyle\sum_{i=1}^{n} v_n \end{cases} \tag{3.17}$$

where V_t is the cell terminal voltage, C_{Ah} is the nominal cell capacity expressed in ampere-hour, I_b is the battery current, which is positive in discharging, R_0 is the series resistance and R_n and C_n are the resistances and the capacitances values of the n-order ECM.

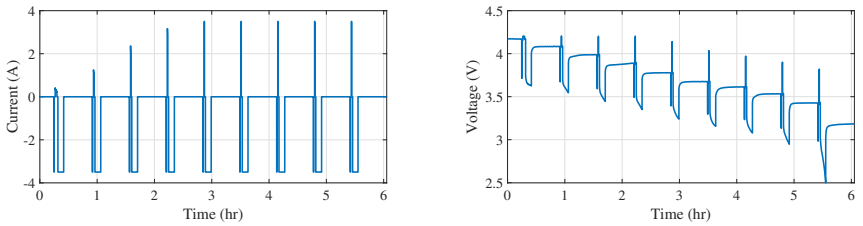

(a) (b)

Figure 3.3: Experimental HPPC test procedure: (a) measured current and (b) corresponding terminal voltage.

3.2.3 Model Parameter Characterization

ECMs are usually characterized by means of experimental test procedures. The first parameter to be identified is the capacity of the battery cell. A complete discharge process starting from a fully charged condition is typically performed in order to correctly define the real cell capacity in different operating conditions. Since the capacity strongly depends on temperature and charging/discharging C-rate, the test is usually executed in a climatic chamber to maintain a constant temperature during the whole test. Meanwhile, the current amplitude is controlled by a cell cycler, which is usually a programmable power supply/load. The other parameters are strongly related to the SoC. Therefore, during the test procedure, the current measurement is typically used to online calculate the SoC value with the Coulomb Counting method. As result, a large amount of experimental data is required to accurately identify the parameters of the ECM. The SoC-OCV curve can be approximated by the cell voltage response under low C-rate, constant current cycles. Alternatively, the OCV is assumed to be the cell terminal voltage after a proper rest time.

The Hybrid Pulse Power Characterization (HPPC) is a widely adopted experimental test procedure to identify battery ECM parameters [89]. Step changes in SoC are predefined and the cell is gradually discharged from a fully charged condition, as shown in figure 3.3. Between each SoC change step, short-duration current pulses are performed to generate sufficient dynamic behavior to identify the parameters under the assumption of constant SoC.

Right after each pulse repetition, a one hour resting period is observed to allow the cell for reaching electrochemical equilibrium and

the OCV corresponding to each SoC step i is measured, as follows:

$$V_{oc}(SoC_i) = V_t(t) \tag{3.18}$$

The series resistance R_0 is usually calculated from the voltage drop that occurs right after the start of a current pulse. Considering the pulse being applied at time t_i and the voltage drop being observed at time $t_i + \Delta t$, the series resistance is measured as follows:

$$R_0(SoC_i) = \frac{V_t(t_i + \Delta t) - V_t(t_i)}{I_b} \tag{3.19}$$

where I_b is the amplitude of the current pulse. The values of the equivalent resistance and capacitance of the RC branches included in the model are determined by exploiting the terminal voltage measured during the cell relaxation right after the current pulse is stopped. In particular, an exponential function is fitted to the measured voltage and the R_n-C_n parameters are derived from the obtained time constants.
Figure 3.3 shows the voltage and current measurements of a Lithium-ion battery cell during an HPPC test.

Due to the large amount of experimental tests needed, and the dependency to the operating conditions, these parameters are usually identified in a laboratory environment. Subsequently, they are stored in lookup tables or characteristic function are linearly extrapolated for implementing the model in a real- world application.

3.2.3.1 Modelling results

In order to validate the performances of the KFs in estimating the SoC, the ECM of different Lithium-Ion batteries has been characterized. In detail, the HPPC test procedure has been performed on two different battery cells, a 40 Ah Kokam pouch cell (model SLPB100216216H1) and a 3.5 Ah Efest cylindrical cell (model IMR18650 V1). The technical specifications of the two cells considered in the analysis are reported in table 3.4.

Table 3.4: Technical specifications of Kokam and EFEST cells.

	Kokam	**EFEST**
Chemistry	NMC	LMO
Nominal capacity (Ah)	40	3.5
Nominal voltage (V)	3.7	3.7
Cut-off voltage (V)	2.7	2.5
Maximum working voltage (V)	4.2	4.2
Maximum charging current (A)	120	4
Standard charging current (A)	80	2
Continuous discharging current (A)	320	10
Pulse discharging current (A)	600	20
Temperature operating range (℃)	0 − 40	0 − 45

The Kokam Lithium-ion cell has been characterized by performing the HPPC test at 0.5, 1 and 1.5 C-rates. The identified SoC-OCV curve is shown in figure 3.4(a). It was extracted at each 10% SoC step after 1 hour rest time and it resulted approximately the same in all the performed tests.
The other parameters for a second-order ECM were identified at different C-rates separately for charging and discharging phase. The results are reported in figures 3.4(b-f), where the current is positive for charging and negative for discharging.

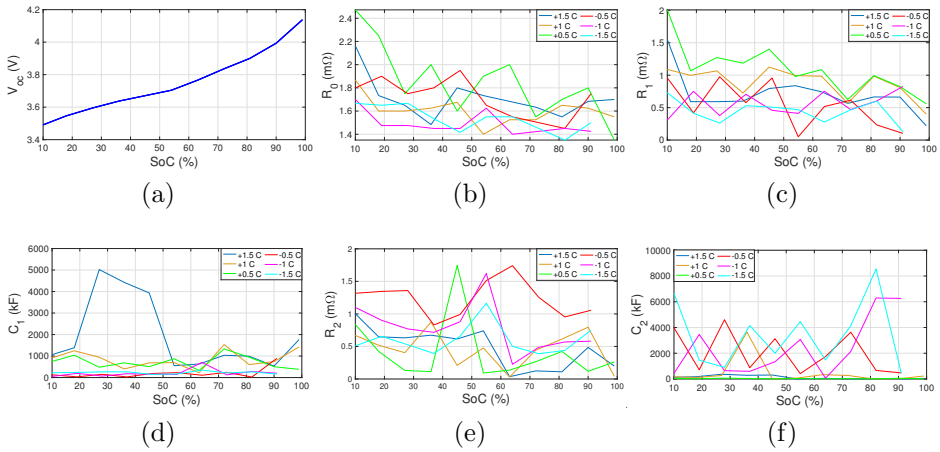

Figure 3.4: ECM parameters of a Kokam Li-Ion Battery for different C-rates: (a) OCV-SoC curve, (b) R_0, (c) R_1, (d) C_1, (e) R_2, (f) C_2.

The EFEST Lithium-ion cell was characterized by performing the HPPC test at 0.5, 1 and 2 C-rates. The identified OCV-SoC curve is shown in figure 3.5(a). It was extracted at each 10% SoC step after 1 hour rest time and it resulted approximately the same in all the performed tests.
The other parameters were identified for three ECMs with different model order (zero, first and second-order) by analyzing the measured data during the discharge phase of the tests. The results obtained from the modelling procedures, distinguished by model order and C-rate value, are reported in figures 3.5(b-j).

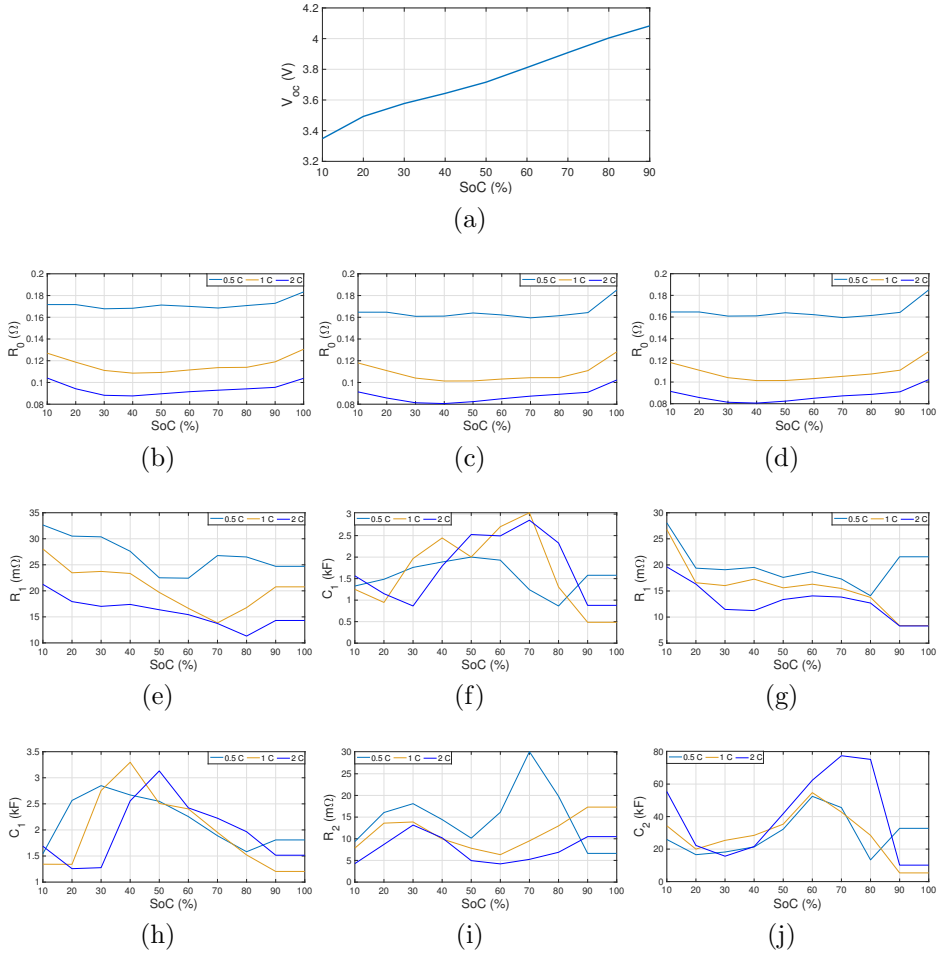

Figure 3.5: Zero, first and second-order ECM parameters of a 18650 EFEST Li-Ion Battery: (a) OCV-SoC curve, (b) Zero-order R_0, (c) first-order R_0, (d) second-order R_0, (e) first-order R_1, (f) first-order C_1, (g) second-order R_1, (h) second-order C_1, (i) second-order R_2, (j) second-order C_2.

3.2.4 Battery pack models

Lithium-ion battery packs usually involve a large number of cells in series and parallel connections in order to meet the specific voltage and capacity requirements. Usually, in order to select similar cells to compose a battery pack, manufacturers adopts specific design processes such as scanning procedures and cell testing to check their main features. However, even after these processes, the cells inside a battery pack always present differences in real-world applications. Therefore, the definition of a model to represent the behavior of a complete battery pack is not a straightforward operation.

Multi-Cell Model

Multi-Cell Model (MCM) is the most accurate method to represent the behavior of a battery pack. It adopts a single cell model, usually chosen as a first or second order ECM, and model parameters are separately identified for each cell. Extensive details and interconnections behavior are addressed with this approach. However, time-consuming characterization procedures and high computational effort for implementing the model are major concerns. Indeed, MCMs are hardly suitable for real-time implementation and their adoption in state estimation tasks lead to high complexity, which cannot be afforded by commonly adopted BMSs [90].

Big Cell Model

The Big Cell Model (BCM) approach adopts the same single-cell model for the entire battery pack, which is considered as a single unit. The identification process is performed only once without taking into account internal connections and differences between the cells. This model is characterized by simplicity and easy implementation, while ensures enough accuracy for many applications not requiring detailed knowledge of the battery pack internal behavior. However, individual overcharge or overdischarge events are not highlighted in the BCM, which results not suitable in applications with high safety requirements.

Mean and Difference Model

Mean and Difference Models (MDMs) are the most promising for online implementation in state estimation [91], thanks to their good

trade-off between accuracy and complexity in representing the different cell behaviors occurring inside the battery pack. They adopt a mean model composed by mean values of the parameters of all the cells, which represents the overall dynamic behavior of the battery, while each single cell is modeled with a Cell Difference Model (CDM) with respect to the mean pack representation. Nevertheless, this approach leads to significant model complexity related to the number of parameter differences included in the CDM as well as a significant effort in the characterization process.

3.2.5 Kalman Filter for Supercapacitor SoC Estimation

In HESS, accurate knowledge of SoC is of paramount importance, since it allows for maximizing system performance and improving energy management strategies while ensuring safe operating conditions. Nevertheless, the amount of energy stored in a supercapacitor is not directly measurable and internal nonlinear phenomena make the online SoC estimation challenging.

3.2.6 Supercapacitor Models

A proper model of the real system needs to be defined in order to implement an effective and reliable model-based state estimation algorithm, such as the Kalman Filtering method.

In this section, the investigation of modeling approaches for supercapacitors is reported. Two different ECM models have been considered for representing the supercapacitors behavior since they are proven to be the best trade-off between accuracy and implementation complexity.

3.2.6.1 Supercapacitor ECM Models

Equivalent Circuit Models are proven to be the best candidates as system models in model-based state estimation algorithms. Indeed, they provide good trade-off between accuracy and computational cost, resulting particularly suited for real-time implementation [92]. Among the different variants that can be found in literature, multi-branch models and the ECMs usually adopted for battery modeling can be considered to be integrated in Kalman Filters.

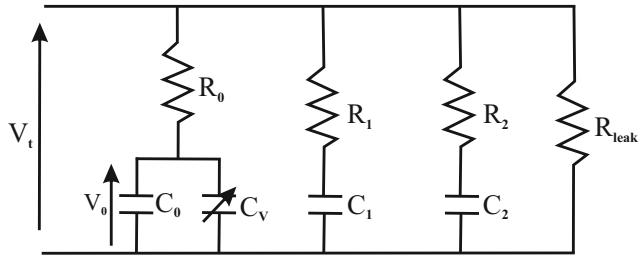

Figure 3.6: Three-branches Electric Circuit Model.

3.2.6.2 Multi-branch Models

Multi-branch models are known to be the most accurate ECMs in representing the typical nonlinear behavior of supercapacitors. In particular, the three parallel branches dynamic model, reported in figure 3.6, is proven to be a good trade-off between model accuracy and computational cost for real-time implementation [92].

As shown in figure 3.6, it is composed of a main RC branch with two parallel-connected RC branches. In the main branch, the basic nonlinear capacitive effect is represented by the capacitor $C(v)$ connected in series with the resistor R. The capacitance dependency on the voltage is taken into account as follows:

$$C(v) = C_0 + C_v = C_0 + K_v \cdot v_0 \tag{3.20}$$

where C_0 represents the fixed capacitance of the SC and K_v is the factor describing the dependency of the capacitance C_v on its voltage v_0. The two additional RC branches, namely R_1-C_1 and R_2-C_2, are included in the model for distinguishing two different time constants, accounting the dynamics related to ion diffusion effect [93]. A leakage resistor R_{leak} for representing the self-discharge effect is included as well and its value is usually declared on the manufacturer datasheet. According to Kirchhoff laws, system equations can be worked out from the ECM as follows.

$$\begin{cases} C\left(v_0\right)\dfrac{dv_0}{dt} = -\dfrac{R_p}{R_0}\left(\dfrac{1}{R_1}+\dfrac{1}{R_2}\right)v_0 + \dfrac{R_p}{R_0R_1}v_1 + \\ \qquad\qquad + \dfrac{R_p}{R_0R_2}v_2 + \dfrac{R_p}{R_0}I \\ C_1\dfrac{dv_1}{dt} = \dfrac{R_p}{R_0R_1}v_0 - \dfrac{R_p}{R_1}\left(\dfrac{1}{R_0}+\dfrac{1}{R_2}\right)v_1 + \\ \qquad\qquad + \dfrac{R_p}{R_1R_2}v_2 + \dfrac{R_p}{R_1}I \\ C_2\dfrac{dv_2}{dt} = \dfrac{R_p}{R_0R_2}v_0 + \dfrac{R_p}{R_1R_2}v_1 + \\ \qquad\qquad - \dfrac{R_p}{R_2}\left(\dfrac{1}{R_1}+\dfrac{1}{R_0}\right)v_2 + \dfrac{R_p}{R_2}I \\ V_t = \dfrac{R_p}{R_0}v_0 + \dfrac{R_p}{R_1}v_1 + \dfrac{R_p}{R_2}v_2 + R_pI \end{cases} \tag{3.21}$$

where $R_p = R_0 \parallel R_1 \parallel R_2 \parallel R_{leak}$, v_1 and v_2 are the voltages on capacitors C_1 and C_2, respectively.

As possible to notice, the observability of the SoC is not an immediate task with this model, since the SoC is not included as a state variable. On the other hand, the model is highly effective if the objective is the estimation of the internal voltages of the supercapacitor, which are included in the model state variables. Therefore, a formulation of the SoC related to the internal capacitor voltages can be considered. In addition, considering the minimum operating voltage of a supercapacitor, usually determined as half of the maximum voltage, a relative indication is worked out according to equation (3.22).

$$SoC_{3B} = \frac{\sum_{i=1}^{n}\frac{1}{2}C_iv_i^2 - E_{min}}{E_{max} - E_{min}} \tag{3.22}$$

where E_{max} represents the characterized maximum energy considering all the internal states, while E_{min} is the minimum necessary energy to be stored in the SC to fully operate it, which is defined as follows:

$$E_{min} = \sum_{i=1}^{n}\frac{1}{2}C_iv_{min}^2 \tag{3.23}$$

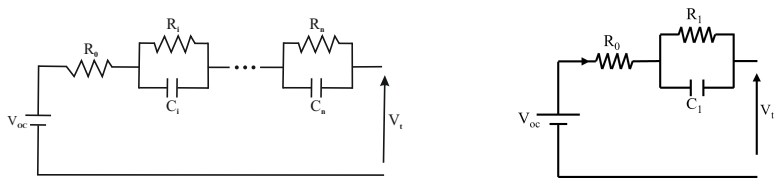

Figure 3.7: (a) n-order and (b) first-order Dynamic Electric Circuit Model.

3.2.6.3 First-order ECM

Electric circuit models are widely adopted in battery state of art for representing equivalent electrical behavior. The electrical characteristic of a supercapacitor can be considered similar to the battery case if the different voltage range and rated capacity exhibited by the device is taken into account. Therefore, the behavior of a SC can be represented by an ideal voltage source connected in series with a resistor R_0 and one or more parallel branches R_i-C_i, as shown in figure 3.7(a). In this work, the first-order ECM reported in figure 3.7(b) has been considered, in which V_{oc} is the Open Circuit Voltage (OCV) and represents the SoC-dependent voltage exhibited by the device in no-load condition. R_0 is the equivalent series internal resistance, mainly due to non-ideal contacts and electrodes, and the R_1-C_1 branch represents the internal charge redistribution and ion diffusion effect.

Since SoC is a variable in the system, the Coulomb Counting method is included in the model, and the following equations are obtained:

$$\begin{cases} SoC = SoC(t_0) - \dfrac{1}{3600 \cdot C_{Ah}} \displaystyle\int_{t_0}^{t} I_{sc}\,(t)\,dt \\ \dfrac{dv_1}{dt} = -\dfrac{v_1}{R_1 C_1} + \dfrac{I_{sc}}{C_1} \\ V_t = V_{oc} - R_0 \cdot I_{sc} - v_1 \end{cases} \tag{3.24}$$

where v_1 is the voltage across the $R_1 - C_1$ branch, C_{Ah} is the nominal capacity expressed in ampere-hour, and I_{sc} is the current flowing in the SC, being positive for discharging and negative for charging phase.

3.2.7 Model Parameter Identification

A good prediction of the supercapacitor behavior in different operating conditions relies on the goodness of the characterization process. In particular, the extraction of model parameters, by means of experimental tests, is required under realistic operating conditions in order to obtain a reliable supercapacitor model. The modeling procedure need to be specifically defined to obtain the best results for the considered model. In the following, an overview of the modelling techniques commonly adopted for the two supercapacitor models presented in section 3.2.6 is reported. Moreover, the two considered models have been characterized in a laboratory environment testing an EATON 166F supercapacitor (model XLR-48R6167-R with the specifications reported in table 3.5) as Device Under Test (DUT) and the results are illustrated as well.

Table 3.5: EATON XLR 166F Supercapacitor Specifications.

Parameter	**Value**
Capacitance (F)	166
Maximum working voltage (V)	48.6
Equivalent Series Resistance (mΩ)	5
Nominal leakage current (mA)	5.2
Stored energy at maximum voltage (Wh)	54
Nominal continuous current (A)	86
Peak power (kW)	118
Pulse current (A)	2200

Three-branches model

Different characterization procedures can be found in literature and a large part of them consider an Electrochemical Impedance Spectroscopy (EIS) approach. It consists in applying AC tests with small current amplitude (usually lower than 1 A) to define the AC resistance of the device under test [94, 95]. However, the low current value is hardly representative of the typical supercapacitor behavior in real-world applications. Therefore, many alternative approaches have been proposed in the literature to achieve better modeling accuracy in more practical operating conditions in terms of current and voltage ranges [93, 96–100].

3.2.7.1 Modelling Results

When a multi-branch model is considered, the supercapacitor is usually subjected to specific procedures during the characterization process. Consequently, the circuit parameters are identified by applying specific formulae to the acquired voltage and current measurements. A well-known and validated method was firstly proposed in [93]. The test consists in imposing to the SC a step current to execute a constant current controlled charge. Once the rated voltage is met at the device terminals, the current is stopped and the terminal voltage is observed over a 30 minutes time period. In detail, with the assumption that only the main branch R_0-C_0 is responsible of the immediate voltage response, these two parameters are derived considering the voltage and current response shown immediately after the current step is imposed.
In table 3.6 the complete procedure and the related equations for identifying the parameters are summarized.

Table 3.6: Three-branch model characterization procedure.

Event	**Procedure**
$t = 0$ DUT Fully discharged	$V_t = 0\ V$ Switch ON the current source: $I = I_{ch}$
$t = t_1 = 20\ ms$	Measure V_1 $R_1 = \frac{V_1}{I_{ch}}$
when $V_t = V_1 + \Delta V$ with $\Delta V = 50mV$	Measure t_2 and $\Delta t = t_2 - t_1$ $C_0 = I_{ch} \cdot \frac{\Delta t}{\Delta V}$
when $V_t = V_3 = V_n$ where V_n is the rated voltage	Measure t_3 Switch OFF the current source: $I = 0\ A$
when $t_4 = t_3 + 20\ ms$	Measure $V_4 = V_t$ $Q_{TOT} = I_{ch} \cdot (t_4 - t_1)$ $C_q = \frac{Q_{TOT}}{V_4}$ $K_v = \frac{2}{V_4} \cdot \left(\frac{Q_{TOT}}{V_4} - C1 \right)$
when $V_5 = V_t = V_4 + \Delta V$ with $\Delta V = 50mV$	Measure t_5 and $\Delta t = t_5 - t_4$ Consider $V_{c0} = V_4 - \frac{\Delta V}{2}$ $C_{diff} = C_0 + K_v \cdot V_{c0}$ $R_1 = \frac{V_{c0} \cdot \Delta t}{C_{doff} \cdot \Delta V}$
when $t_6 = t_5 + 3 \cdot (C_1 \cdot R_1)$ where $C_1 \cdot R_1 \cong 100\ s$ (typically)	Measure $V_6 = V_t$ $C_1 = \frac{Q_{tot}}{V_6} - \left(C_0 + \frac{K_v}{2} \cdot V_6 \right)$
when $V_7 = V_t = V_6 + \Delta V$ with $\Delta V = 50mV$	Measure t_7 and $\Delta t = t_7 - t_6$ Consider $V_{c0} = V_6 - \frac{\Delta V}{2}$ $C_{diff} = C_0 + K_v \cdot V_{c0}$ $R_2 = \frac{V_{c0} \cdot \Delta t}{C_{diff} \cdot \Delta V}$
when $t_8 = 30\ min$	Measure $V_8 = V_t$ $C_2 = \frac{Q_{tot}}{V_8} - \left(C_0 + \frac{K_v}{2} \cdot V_8 \right)$

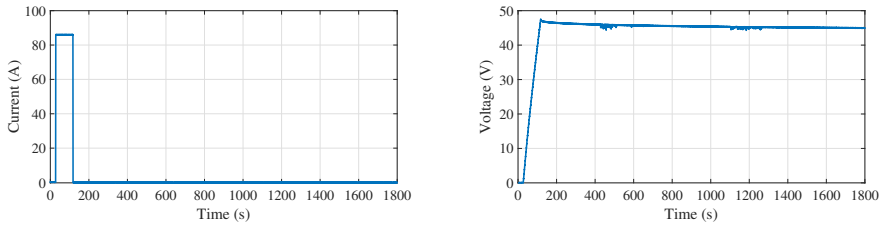

(a) (b)

Figure 3.8: Experimental test for the first SC model characterization procedure: (a) measured current and (b) corresponding terminal voltage.

In laboratory environment, the test was performed by means of a bidirectional power amplifier. The voltage and current waveform measured at the supercapacitor terminals are shown in figure 3.8. The obtained parameters are listed in table 3.7.

Table 3.7: Parameters for the 3-branch Supercapacitor model obtained with the procedure from [93].

Parameter	**Value**
C_0	113.70 F
K_v	2.12 $\frac{F}{V}$
R_0	4.3 $m\Omega$
R_1	16.36 Ω
C_1	6.49 F
R_2	147.55 Ω
C_2	10.83 F
R_{leak}	9.5 $k\Omega$

A different approach has been proposed in the literature to improve the characterization process and the model accuracy [92, 100]. It considers the practical operating currents of the DUT in a realistic application, in terms of current and voltage levels. In detail, a charging/discharging repeating cycle is performed by imposing constant current steps on the device in order to characterize the three-branch model. As shown in figure 3.9, the DUT is charged and discharged four times between a selected minimum voltage level and its nominal value, applying 20 seconds rest period between each phase of the test. In order to replicate a realistic application, the nominal current

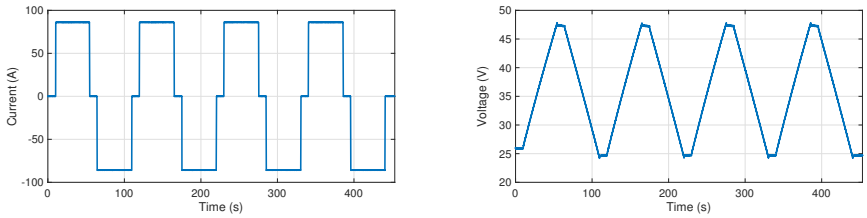

(a) (b)

Figure 3.9: Experimental test for the second SC model characterization procedure: (a) measured current and (b) corresponding terminal voltage.

amplitude have been imposed to charge and discharge the device between the nominal and minimum working voltage values. The latter is defined as half of the maximum cell voltage level.

The test was performed on the EATON supercapacitor and the extraction of the model parameters has been made by means of the "Parameter Estimator" tool in Matlab-Simulink®. It allows to fit the model voltage curve to the measured one by selecting the same current input given by the experimental test. As a solver, the nonlinear least square method was selected, and the parameters shown in table 3.8 were obtained.

Table 3.8: Fitted parameters for the 3-branch Supercapacitor model.

Parameter	**Value**
C_0	132.78 F
K_v	1.08 $\frac{F}{V}$
R_s	5.2 $m\Omega$
R_1	11.01 Ω
C_1	6.61 F
R_2	159.96 Ω
C_2	2.38 F
R_{leak}	9.5 $k\Omega$

The two sets of model parameters have been compared in numerical analysis. In detail, two different models, one for each parameter set, have been implemented in Matlab-Simulink®. The current profile shown in figure 3.9(a) has been imposed to the supercapacitor

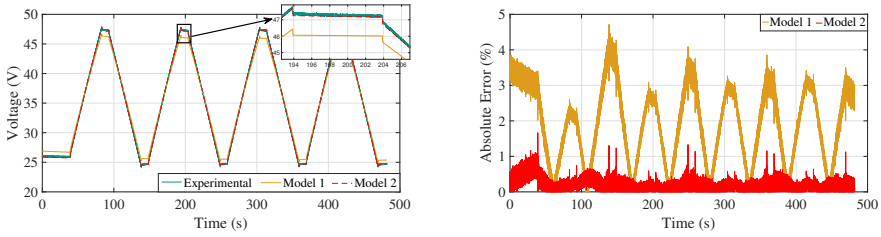

(a) (b)

Figure 3.10: Numerical comparison of the two sets of parameters: (a) terminal voltage and (b) corresponding absolute error with respect to the real supercapacitor voltage.

models and their voltage responses have been compared to the supercapacitor terminal voltage measured during the experimental test. In figure 3.10(a), the voltage measured during the experimental characterization procedure and the terminal voltages of the two models are shown. The first model (*Model 1*) is implemented by using the parameters reported in table 3.7, while the second one (*Model 2*) includes the parameters from table 3.8. As a term of comparison, the absolute errors between the model terminal voltages and the real supercapacitor voltage have been considered (figure 3.10(b)).

The model implementing the second set of parameters, which were obtained by fitting the voltage curve by means of the parameter estimator tool, shows a lower absolute error during the entire simulation. In detail, the error is always lower than 1%, while the model characterized with the procedure described in [93] reaches peaks of 4% absolute error compared to the experimentally measured voltage. Thus, the improvements given by the second identification procedure, which considers a typical operating current of a supercapacitor, have been documented.

First-order ECM model

Differently from the multi-branch models, the n-order dynamic Equivalent Circuit Models, described in section 3.2.6.3 are based on a direct relation between each model parameter and the SoC. This allows for an explicit estimation of the supercapacitor SoC when a model-based state estimator is considered [101].

Considering a first-order ECM, a specific procedure for characterizing the model parameters is needed. As mentioned in section 3.2.3, a

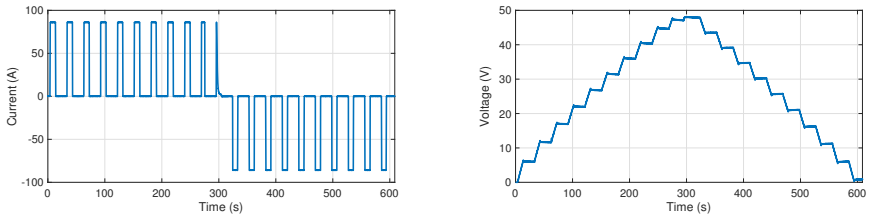

(a) (b)

Figure 3.11: Experimental test for the first-order ECM supercapacitor PPC model characterization procedure: (a) measured current and (b) corresponding terminal voltage.

commonly adopted procedure for Lithium-Ion batteries is the Hybrid Pulse Power Characterization (HPPC) [89]. It involves 20 seconds current pulses executed at incremental SoC values, assuming it to be unaffected by the short duration of the pulses. In case of a supercapacitor, the same assumption is harder to guarantee due to its lower capacity. Hence, the similar Positive Pulsed Current (PPC) approach was adopted [102], and the current pulses were exploited for increasing the supercapacitor SoC and concurrently identifying the parameters of the equivalent circuit model. The procedure has been performed on the EATON supercapacitor at different charging/discharging current levels to characterize the model parameters, which values depends on SoC and current amplitude. Figure 3.11 shows the current and voltage acquired during a nominal current test, as an example. In detail, constant current pulses are maintained for the necessary time to charge or discharge the DUT by a 10% SoC value. Between two consecutive pulses, a 20 seconds rest time is observed. The voltage measured during each resting interval is used for parameter estimation, which results related to the SoC value reached during the previous current pulse. In particular, the series resistance R_o is responsible for the voltage drop ΔV occurring at the moment the current is stopped, and it is derived by dividing ΔV by the current pulse amplitude. The second part of the voltage relaxation is modeled by the fitting of a RC exponential voltage response curve, thus obtaining the values of R_1 and C_1.

The different procedures for characterizing the two models, were both executed with a nominal current amplitude of 86 A for charging and discharging the supercapacitor.

The model parameters obtained from the PPC characterizing proce-

dure are shown in table 3.9, distinguished in charging and discharging phases.

Table 3.9: Extracted parameters with PPC procedure for the first order ECM.

	SoC	V_{oc} (V)	R_0 $(m\Omega)$	R_1 $(m\Omega)$	C_1 (kF)
Discharge	10 %	6.08	2.7	2.6	4.77
	20 %	11.28	2.7	2.1	5.47
	30 %	16.28	2.7	1.9	5.97
	40 %	21.09	2.7	1.8	5.79
	50 %	25.73	2.6	1.7	5.65
	60 %	30.27	2.7	1.6	5.63
	70 %	34.73	2.8	1.4	5.75
	80 %	39.14	2.8	1.1	5.52
	90 %	43.51	2.6	0.8	3.90
Charge	10 %	5.98	2.8	1.2	7.55
	20 %	11.62	2.8	1.6	6.23
	30 %	16.92	2.7	1.8	5.95
	40 %	21.92	2.7	2.1	5.64
	50 %	26.71	2.7	2.5	5.25
	60 %	31.34	2.7	2.8	4.82
	70 %	35.85	2.6	3.2	4.42
	80 %	40.26	2.8	3.3	4.31
	90 %	47.03	2.6	4.0	3.78

Chapter 4

Model-based SoC Estimation in ESSs and HESSs

[Original contribute]

The knowledge of accurate SoC in Energy Storage Systems is of paramount importance. In battery packs, it allows for performance maximizing and avoiding hazard conditions at cell level, such as overcharge or overdischarge. In Hybrid Energy Storage Systems, a correct estimation of the SoC of the involved devices enables the use of advanced energy control strategies. Indeed, the best power allocation between two or more energy sources with substantial differences in power and energy characteristics can be achieved considering an accurate knowledge of each system component state while ensuring safe operating conditions.
In this chapter, SoC estimation techniques for batteries and supercapacitors are illustrated. A novel adaptive algorithm has been proposed for single-cell Lithium-Ion batteries and a methodology for multiple SoC estimation in battery packs have been proposed. The same SoC estimator has been developed for supercapacitor SoC estimation in Hybrid Storage Systems and their performances in many operating conditions have been evaluated.

4.1 Introduction

The knowledge of accurate SoC in battery packs allows for performance maximizing and avoiding hazard conditions, such as overcharge

or overdischarge. The most common solution in practical applications is the Coulomb Counting method, thanks to its simplicity and low computational cost. However, the performance of this method result affected by knowledge accuracy of the initial SoC condition as well as measurement errors and noise. Different methods can be found in literature for improving SoC estimation, and most promising solutions among them are represented by Kalman Filters (KFs). They are model-based optimal state observer, which result unaffected by measurement noise and capable of correcting the initial state estimation error.

4.2 Single-cell Battery SoC Estimation

In the actual state of the art, many variants of the linear Kalman FIlter are proposed for state estimation in nonlinear systems. As already discussed in section 3, main solutions for SoC estimation in Li-Ion batteries are represented by the Extended Kalman Filter (EKF), the Unscented Kalman Filter (UKF) and the Square-Root Unscented Kalman Filter (SR-UKF).

4.2.1 Performance Comparison

The second-order ECMs for the 3.5-Ah EFEST and the 40-Ah Kokam battery cells, presented in section 3.2.3, and all the KFs previously discussed have been implemented in Matlab® using the Simulink environment with the aim of evaluating and comparing the differences in estimating the SoC. In detail, numerous experimental tests have been performed for characterizing the electrical behavior of the cells and experimentally calibrating the second-order ECMs, in which all the battery parameters depend on SoC and charging/discharging C-rate.

The initialization of the KFs has been performed with reference to the guidelines reported in [75] and discussed in 3.1.4, which consider the computation of the measurement and process noise covariances as illustrated in equations (4.1) and (4.2), respectively.

$$R = (dE_m)^2 \tag{4.1}$$

$$Q = \begin{bmatrix} (dSoC)^2 & 0 & 0 \\ 0 & (dU)^2 & 0 \\ 0 & 0 & (dU)^2 \end{bmatrix} \tag{4.2}$$

where dE_m is the voltage measurement accuracy (assumed to be equal to $1e-2$), $dSoC$ is the maximum SoC variation in a complete charging or discharging process, dU is the maximum variation of the voltages on the two RC branches in the ECM (indicatively set to $dU = 1\ V$).
Likewise, assuming the initial state variables errors equal to 10% for the SoC and 0.01 V for voltages, the initial state covariance (P_0) can be yield as follows:

$$P_0 = \begin{bmatrix} 0.01 & 0 & 0 \\ 0 & 0.0001 & 0 \\ 0 & 0 & 0.0001 \end{bmatrix} \tag{4.3}$$

The impact of the filter initialization on the estimation performances has been evaluated by imposing a variability in the filter parameters of all the considered KFs, which have been subjected to the same testing procedure. Moreover, the proposed adaptive algorithm has been included in the analysis to confirm its robustness to the imposed variability.
Then, the impact of the initial estimation error has been investigated by performing the numerical test at different initial SoC value set in the KF algorithms. Further numerical analysis has regarded the influence of the battery model accuracy in the estimation performance. In particular, the series resistance R_0 of the cell model has been subjected to a parameter variation with respect to the nominal value and the estimation error of the main KFs has been compared to the proposed ASR-UKF. Experimental results have been reported as well.

4.2.2 Impact of Filter Initialization

In this section, the issues related to the initialization and calibration of the KFs, thus the proper selection of the process and measurement noise covariance matrices, have been investigated.

A constant discharging current at 0.5C for a time interval of twelve minutes has been considered as current profile for the numerical analysis, which corresponds to a SoC reduction of 10% for the battery

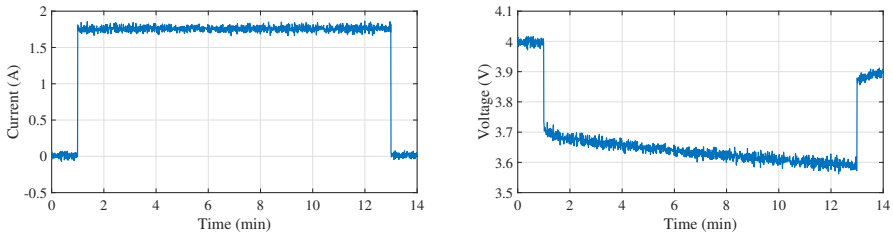

(a) (b)

Figure 4.1: (a) Current profile and (b) corresponding battery terminal voltage with random noise.

cell. Moreover, in order to reproduce the characteristics of commercial current and voltage sensors, random noise has been added to the voltage and the current measurements, as shown in figure 4.1. This specific current profile allows for correctly defining the SoC condition at the end of the discharging process and thus better evaluating and comparing the estimation errors achieved with all the KFs.

Therefore, starting from an initial SoC condition equal to 80% for the battery cell, the constant current profile at 0.5C (figure 4.1(a)) has been applied to both the battery system and the ECM adopted by the KFs for the SoC estimation. In this way, the difference between the SoC estimated by the KFs at the end of the discharging process and the expected SoC of 70% has been considered as a performance parameter for the numerical analysis. It is important to highlight that the initial SoC of the battery system model has been set to 80%, whereas the KFs have been initialized with a $SoC_0 = 75\%$ in order to evaluate the estimation results with a 5% of initial guess error as well.

The impact of the initialization and calibration of the KFs parameters on the overall performances of the filters has been evaluated by varying the values of both the measurement noise covariance R_k and the elements of the process noise covariance matrix Q_k with respect to the filter initialization performed by means of the equations (4.1), (4.2) and (4.3). Therefore, the variability of the filters parameters has been reproduced by adopting two coefficients for the measurement noise covariance (α_R) and the process noise covariance matrix (α_Q), resulting:

$$R = (dE_m)^2 \cdot \alpha_R \tag{4.4}$$

$$Q = \begin{bmatrix} (dSoC)^2 & 0 & 0 \\ 0 & (dU)^2 & 0 \\ 0 & 0 & (dU)^2 \end{bmatrix} \cdot \alpha_Q \tag{4.5}$$

In detail, the SoC estimation results achieved by adopting the EKF, the UKF and the SR-UKF with respect to different initialization of the filter parameters are summarized in tables 4.1, 4.2 and 4.3, respectively. As possible to notice, the SoC estimated by the KFs at the end of the discharging current profile is highly dependent on the process noise covariance Q. Indeed, excluding the results for which a SoC estimation error lower than 1% is achieved (highlighted in green), an incorrect initial calibration of the matrix Q could lead to estimation errors higher than 10% in several cases, especially for the EKF and the UKF, resulting $\alpha_R = \alpha_Q = 1e6$ as the worst condition. In this case, the SR-UKF is not able to provide a consistent SoC estimation as well. Moreover, the initialization of the filters parameters according to the guidelines reported in does not allow for minimizing the SoC estimation error for both the EKF and the UKF since more accurate results are observed by varying α_R and α_Q. Therefore, these results confirm quantitatively the issues related to the calibration of the KFs parameters.

Table 4.1: SoC estimated (in %) at the end of the 0.5C discharging current pulse by EKF considering a 5% initial estimation error.

α_R \ α_Q	**1e-4**	**1e-3**	**1e-2**	**1e-1**	**1**	**1e1**	**1e2**	**1e3**	**1e4**	**1e5**	**1e6**
1e-4	73.33	75.13	75.12	88.64	88.95	79.79	89.44	89.44	89.44	89.44	81.33
1e-3	70.15	73.43	75.13	75.12	88.62	88.95	88.20	89.43	89.44	89.44	89.44
1e-2	73.48	70.60	74.32	75.13	75.12	88.53	88.95	89.39	89.44	89.44	89.44
1e-1	69.74	69.76	70.07	73.19	75.13	75.12	88.55	88.48	89.39	89.44	89.44
1	70.25	70.25	70.27	70.45	71.39	75.01	75.13	88.66	88.95	89.39	81.54
1e1	70.18	70.18	70.18	70.17	70.25	70.80	74.90	75.13	88.66	81.43	89.39
1e2	70.05	70.05	70.05	70.04	70.04	70.10	70.50	74.87	75.13	88.66	88.95
1e3	69.82	69.82	69.82	69.82	69.81	69.76	69.55	69.27	73.98	75.13	88.55
1e4	68.80	68.80	68.80	68.79	68.79	68.73	68.41	67.84	67.78	73.21	75.13
1e5	66.45	66.45	66.45	66.45	66.45	66.47	66.58	66.85	67.04	67.45	73.08
1e6	65.17	65.17	65.17	65.17	65.17	65.18	65.24	65.69	66.51	66.93	67.42

Table 4.2: SoC estimated (in %) at the end of the 0.5C discharging current pulse by UKF considering a 5 initial estimation error.

α_R \ α_Q	**1e-4**	**1e-3**	**1e-2**	**1e-1**	**1**	**1e1**	**1e2**	**1e3**	**1e4**	**1e5**	**1e6**
1e-4	61.83	58.36	66.48	72.23	84.33	71.66	72.65	82.14	28.11	50.09	50.06
1e-3	69.85	65.10	65.69	66.63	76.83	71.78	72.87	90.92	28.11	50.09	50.06
1e-2	70.01	68.29	62.76	65.45	67.65	72.79	72.89	74.90	28.12	50.09	50.06
1e-1	71.35	71.46	72.20	73.67	74.13	73.23	74.12	37.90	28.07	50.09	50.06
1	70.46	70.46	70.51	70.93	72.08	73.81	74.43	77.00	80.83	50.09	50.06
1e1	70.28	70.28	70.27	70.27	70.36	70.90	73.64	77.98	58.53	50.10	50.06
1e2	70.01	70.01	70.01	70.00	69.97	69.98	69.82	69.53	54.80	50.09	50.06
1e3	69.64	69.64	69.64	69.63	69.61	69.46	69.05	68.98	60.13	50.07	50.06
1e4	68.95	68.95	68.95	68.95	68.94	68.88	68.66	69.15	59.35	50.03	50.04
1e5	67.09	67.09	67.09	67.09	67.09	67.13	67.50	69.17	56.63	50.01	50.01
1e6	65.30	65.30	65.30	65.30	65.30	65.32	65.46	66.63	50.01	50.00	50.00

Table 4.3: SoC estimated (in %) at the end of the 0.5C discharging current pulse by SR-UKF considering a 5 initial estimation error.

α_R \ α_Q	**1e-4**	**1e-3**	**1e-2**	**1e-1**	**1**	**1e1**	**1e2**	**1e3**	**1e4**	**1e5**	**1e6**
1e-4	69.95	70.25	71.07	72.81	72.84	72.84	72.84	72.85	72.84	73.22	74.09
1e-3	69.77	69.85	70.15	71.03	72.81	72.84	72.84	72.85	72.84	73.22	74.09
1e-2	69.75	69.75	69.84	70.14	71.06	72.82	72.84	72.85	72.84	73.22	74.09
1e-1	69.87	69.87	69.87	69.94	70.24	71.06	72.81	72.85	72.84	73.22	74.09
1	69.91	69.91	69.91	69.91	69.98	70.27	71.05	72.82	72.85	73.22	74.09
1e1	69.93	69.93	69.93	69.93	69.93	70.00	70.29	71.05	72.75	73.22	74.09
1e2	69.94	69.94	69.94	69.94	69.94	69.94	70.01	70.29	71.02	73.07	74.08
1e3	69.98	69.98	69.98	69.98	69.98	69.98	69.98	70.04	70.37	71.29	73.51
1e4	69.72	69.72	69.72	69.72	69.72	69.72	69.72	69.72	69.89	70.53	71.17
1e5	67.48	67.48	67.48	67.48	67.48	67.48	67.48	67.49	67.55	70.85	55.74
1e6	65.00	65.00	65.00	65.00	65.00	65.00	65.00	65.00	65.00	65.20	NaN

The proposed adaptive algorithm described in section 3.1.5 and summarized in table 4.4, has been adopted for overcoming the initialization problem in Kalman filtering methods.

Table 4.4: Adaptive Square-Root Unscented Kalman Filter algorithm.

Prediction

Sigma points calculation

$$\chi_{k-1} = [x_{k-1} \quad x_{k-1} + \gamma S_{k-1} \quad x_{k-1} - \gamma S_{k-1}]$$

$$\chi_k = f(\chi_{k-1}, u_k)$$

$$x_k^- = \sum_{i=0}^{2L} W_i^m \chi_{i,k}$$

$$S_k^- = qr\left\{\left[\sqrt{W_1^c}\left(\chi_k - x_k^-\right) \quad Q\right]\right\}$$

$$S_k^- = cholupdate\left\{S_k^-,\ \chi_k(0) - x_k^-,\ W_0^c\right\}$$

$$\Upsilon_k = g(\chi_k, u_{k-1})$$

$$y_k^- = \sum_{i=0}^{2L} W_i^m \Upsilon_{i,k}$$

Update

$$S_y = qr\left\{\left[\sqrt{W_1^c}\left(\Upsilon_k - y_k^-\right) \quad R\right]\right\}$$

$$S_y = cholupdate\left\{S_y,\ \Upsilon_k(0) - y_k^-,\ W_0^c\right\}$$

$$P_{xy} = \sum_{i=0}^{2L} W_i^c \left[\chi_{i,k,k-1} - x_k^-\right]\left[\Upsilon_{i,k} - y_k^-\right]^T$$

$$K_k = \left(P_{xy}/S_y^T\right)/S_y$$

$$x_k = x_k^- + K_k\left(y_{mk} - y_k^-\right)$$

$$U = K_k S_y$$

$$S_k = cholupdate\left\{S_k^-,\ U,\ -1\right\}$$

Update of Covariance Matrices

$$y_k = g(x_k, u_k)$$

$$C_k = \frac{1}{N}\sum_{i=k-N}^{k}(y_{mk} - y_k)^2$$

$$Q_k = \sqrt{|diag(diag(K_k C_k (K_k)^T))|}$$

$$R_k = \sqrt{C_k + \sum_{i=1}^{2L} W_i^c \cdot [\Upsilon_{i,k} - y_{mk}]\left[\Upsilon_{i,k} - y_{mk}\right]^T}$$

In order to demonstrate the high performances of the proposed ASR-UKF in terms of robustness and capability to be unaffected by covariance matrices initialization, the proposed adaptive algorithm has been tested and validated considering the discharging current profile at 0.5C and the initialization of the parameters in the worst condition previously observed. In particular, table 4.5 reports a comparison among the SoCs estimated at the end of the discharging current profile at 0.5C by the KFs and the proposed ASR-UKF in the worst

condition, highlighting the effectiveness of the proposed adaptive algorithm, which allows for achieving a SoC estimation error lower than 1% and thus results unaffected by the initial filter calibration.

Table 4.5: Comparison among the SoCs estimated by the KFs and the proposed ASR-UKF.

$\alpha_R = \alpha_Q = 1e6$	**Final SoC estimated**
EKF	67.42 %
UKF	50.00 %
SR-UKF	*NaN*
ASR-UKF	70.08 %

Then, further investigation has been carried out for evaluating the time interval needed by the proposed adaptive algorithm for updating the covariance matrices up to their optimal value. Figure 4.2 shows the variability of the covariance values operated by the proposed ASR-UKF during the discharging current profile in the worst condition. As possible to notice, the noise covariance R does not reach a steady-state value since it is only related to the voltage measurement sensor noise and thus it oscillates around the nominal accuracy value. On the other hand, according to figures 4.2(b) and 4.2(c), the covariance noise related to the SoC estimation process and the dynamic voltages behave differently since they are expressed by the three coefficients that compose the covariance matrix Q. In this case, a brief transient phase of about two minutes is noticed at the beginning of the current profile, then a very low variability of the filter parameters operated by the adaptive algorithm is observed. Therefore, these results highlight the high performances of the proposed ASR-UKF, able to eliminate the complexity and uncertainty related to the initialization and calibration of the KFs parameters as well as to provide a fast response in adjusting incorrect filter parameters.

4.2.3 Impact of Initial Estimation Error

In this analysis, the second-order ECM of the 40-Ah NMC Kokam battery has been integrated as plant model for the filters.
The Coulomb counting method operated on the ideal current profile has been considered as reference for SoC estimation results. On the other hand, random noise has been added to the voltage and current

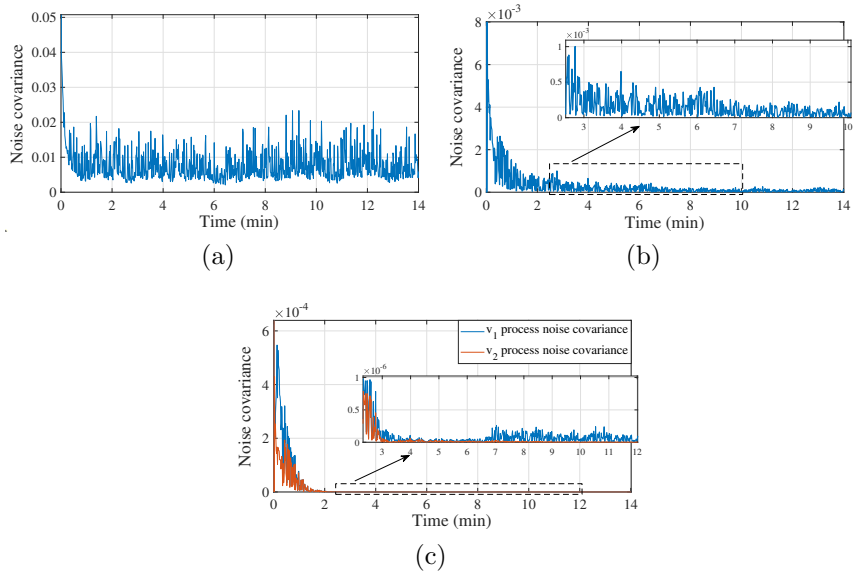

Figure 4.2: Time-varying covariance matrices in Adaptive SR-UKF considering the worst calibration conditions: (a) measurement noise covariance R, (b) SoC estimation process noise covariance and (c) dynamic voltages estimation process noise covariance.

measurements for the filters in order to reproduce the characteristics of commercial sensors.
Figure 4.3(a) shows the current profile adopted for testing the performances of the Kalman filters implemented, which consists of a discharging at 1C. The impact of different initial SoC values (SoC_0) on the performance of the filters has been evaluated by considering SoC initial guess error of 10% and 30%. In detail, setting a true initial SoC of 70% for the battery, figures 4.3(b) and 4.3(c) show the SoC estimation results and the errors with respect to the Coulomb counting method for $SoC_0 = 60\%$, while figures 4.3(d) and 4.3(e) those for $SoC_0 = 40\%$.

Table 4.6 reports the SoC estimation errors achieved with the Kalman filters implemented considering the two SoC_0 conditions. It results that all the Kalman filters ensure SoC estimation errors lower than 1% in absolute value with respect to the Coulomb counting method in both SoC_0 conditions. In particular, considering the two merit factors reported in table 4.6, a similar responses of the filters can be observed. Therefore, it can be assumed that the UKF, the

Table 4.6: Numerical results: SoC estimation errors for the UKF, the SR-UKF and the proposed ASR-UKF with respect to the ideal Coulomb counting method.

	$SoC_0 = 60\%$		$SoC_0 = 40\%$	
	Mean	**RMSE**	**Mean**	**RMSE**
UKF	0.26%	0.62%	0.76%	2.19%
SR-UKF	0.40%	0.69%	1.16%	2.33%
Proposed	0.24%	0.64%	1.14%	3.95%

SR-UKF and the proposed ASR-UKF are not particularly affected by the SoC initial guess error.

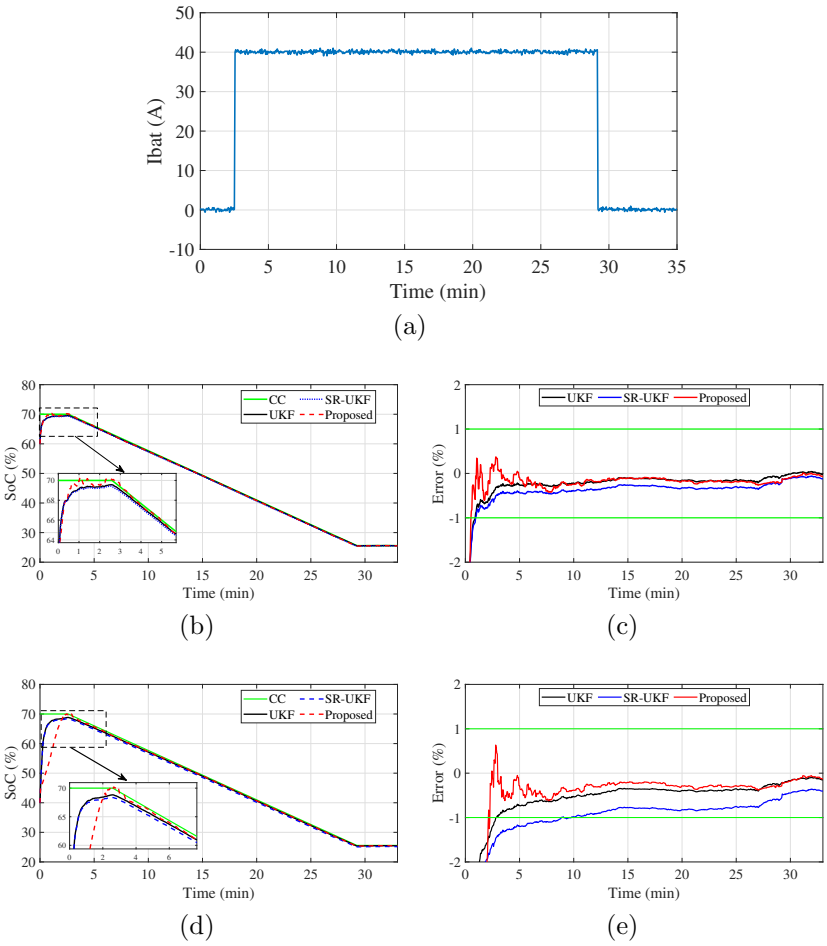

Figure 4.3: Numerical results for SoC estimation considering different values for the initial SoC: (a) current profile with random noise; (b-d) SoC estimation results and (c-e) error with respect to the Coulomb counting method for $SoC_0 = 60\%$ and $SoC_0 = 40\%$ have been considered in Kalman filters, respectively.

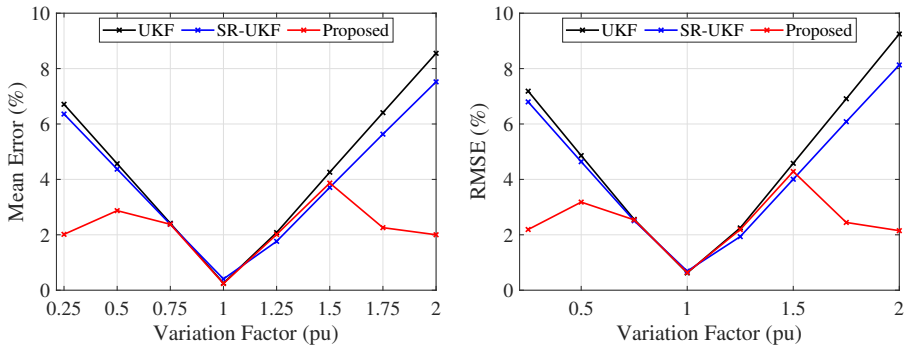

Figure 4.4: Numerical results for SoC estimation considering a variation of the internal resistance of the battery: (a) mean estimation error and (b) RMSE.

4.2.4 Impact of Model Parameter Variation

The numerical analysis has been also extended to the investigation of the filter robustness with respect to parameter variations of the battery model. In detail, a variation of the internal resistance Rs of the battery has been introduced in the model implemented for the Kalman filters. The initial SoC value has been set to $SoC_0 = 60\%$ for this analysis. Figure 4.4 shows the absolute mean SoC estimation errors and the RMSE achieved with the UKF, the SR-UKF and the proposed ASR-UKF by considering a variation of R_s that ranges from 0.25 to 2 per unit. It can be observed that the proposed ASR-UKF results to be less affected by parameter variations of the battery model than both UKF and SR-UKF, since it maintains an estimation error lower than 4% even for large variation of R_s.
The results have highlighted better performances of the proposed ASR-UKF in compensating even large variations of the internal resistance of the battery model.

4.2.5 Experimental results

An experimental set-up has been carried out for validating the performances of the proposed ASR-UKF. Since the SR-UKF has low computational cost and represents an improvement of the UKF, only the comparison between the SR-UKF and the proposed ASR-UKF has

been performed. Both filters have been implemented on a Texas Instrument TMS320F28335 evaluation board which is characterized by a 32 bit C2000 Digital Signal Processor (DSP) with a clock speed of 150 MHz mounted.
In order to avoid misalignment between the execution code of the filters in MATLAB and on the Texas microcontroller, the MATLAB coder tool has been adopted. Furthermore, the SoC estimation results from the SR-UKF and the ASR-UKF have been compared with those from the Coulomb counting method in real conditions. In this way, the performances of the filters can be evaluated with respect to a real-world application of the SoC estimation method.
Therefore, two different timer interrupt have been set, a slower one for the Kalman filter execution (3 s of time step) and a faster one for voltage and current measurements (1 ms of time step). This also allows for correctly estimating the SoC and thus reducing the estimation error from the Coulomb counting method. The battery terminal voltage has been acquired and scaled down by means of a resistor divider in order to be suitable for the 12 bit ADC of the microcontroller, whereas a current transducer (LEM model LA 125P) has been adopted for current measurement.
A control tool has been also developed for automatically acquiring the voltage and current measurements as well as managing remotely the electronic load needed for carrying out the experimental test.
In detail, the current profile adopted for the numerical analysis has been considered for the experimental test as well.
Figure 4.5 shows the results achieved from the experimental test, while table 4.7 reports the SoC estimation errors for the SR-UKF and the proposed ASR-UKF with respect to the Coulomb counting method in real conditions. In particular, the Coulomb counting method has been operated by considering the true initial SoC equal to 70%, whereas a SoC initial guess error of 10% has been defined for the Kalman filters.

Table 4.7: Experimental results: SoC estimation errors for the SR-UKF and the proposed ASR-UKF with respect to the real Coulomb counting method.

	Mean	**RMSE**
SR-UKF	0.88%	1.03%
Proposed	0.37%	0.67%

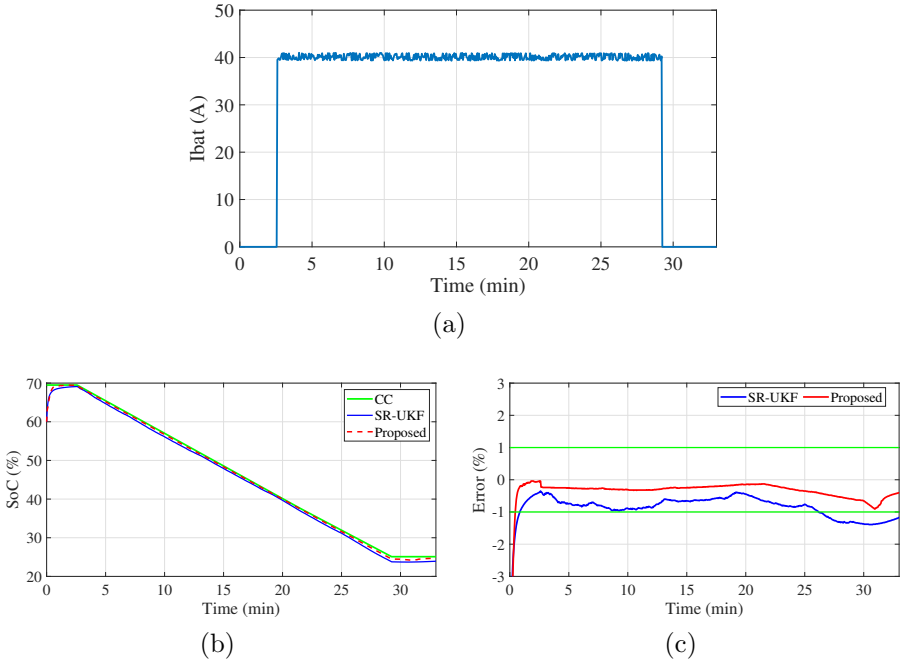

Figure 4.5: Experimental results for SoC estimation considering $SoC_0 = 60\%$: (a) acquired current profile, (b) SoC estimation results and (c) errors with respect to the Coulomb counting method in real conditions.

The experimental results validate the performance of the proposed ASR-UKF, which allows for achieving a lower SoC estimation error with respect to the SR-UKF.

4.3 Battery Pack Multiple SoC Estimation

Lithium-ion battery packs usually involve a large number of cells in series and parallel connections in order to meet the specific voltage and capacity requirements. Performances and reliability represent relevant aspects to be taken into account by the Battery Management System (BMS), responsible of maximizing the usable capacity of the battery pack while ensuring its safe operating conditions [63]. Among all the main tasks operated by the BMS, an accurate estimation of the State of Charge (SoC) is highly required for maximizing the pack

performances and avoiding hazard conditions. Moreover, considering cell-to-cell parameters' variations that can occur within the battery pack [104,105] due to manufacturing tolerances, thermal gradients and different aging conditions, the evaluation of the SoC of the least/most charged cell allows an effective and safe management of the battery pack, however a reduction of the pack energy utilization results [106]. Therefore, an estimation of the SoC at pack level is definitely necessary for maximizing the performances by providing relevant information regarding the available energy and the whole battery pack state [105]. With reference to all the single-cell estimation methods proposed in the literature, the model-based Kalman Filters (KFs) have become a commonly adopted solution thanks to their robustness to measurement noise and initial guess error [69]. They require a proper battery model able to reproduce the pack behavior for increasing the estimation performance [107].

The most accurate solutions rely on the combination of the observer with a Multicell Model (MCM) approach [108], which separately identifies model parameters for each cell. As result, the related computational effort cannot be afforded by commonly implemented BMSs [90].

Other solutions include the Big Cell Model (BCM) approach, which adopts the same single-cell model for the entire battery pack, neglecting its internal connections and cell-to-cell parameters' variations. In this way, the overall pack state is estimated but individual overcharge or overdischarge events cannot be prevented, leading to accelerated ageing of the cells [109]. The evaluation of the SoC of the cell characterized by the minimum or the maximum cell voltage during discharging and charging process, respectively, represents an effective solution for preventing hazard conditions for the battery pack [110]. Similar methods include a scanning process of the cells in order to identify the Poorest SoC Cell (PSC) as a reference for the battery pack [111]. However, the lack of global state estimation of the storage system is not addressed. Additional details of the plant condition can be achieved with the adoption of a Mean and Difference Model (MDM) concurrently with a SoC estimation method [91]. This involves a mean model composed by the mean values of all the cells' parameters, which represents the overall dynamic behavior of the battery, while each single cell is modeled with a Cell Difference Model (CDM) with respect to the mean pack representation [112]. Nevertheless, this approach leads to significant model complexity related to the number of parameter differences included in the CDMs to be implemented and a significant effort in their characterization.

A methodology based on an Adaptive Square-Root Unscented Kalman Filter (ASR-UKF) that allows for performing multiple SoC estimations in real-time has been developed.

4.3.1 Proposed Methodology for Multiple SoC Estimation

This section describes the Adaptive Square-Root Unscented Kalman Filter (ASR-UKF) method, adopted for multiple cell SoC estimation. The ASR-UKF presented in [77] is taken into account since its higher performances with respect to other Kalman filters have been demonstrated [113, 114]. The accurate state estimation has been extended to multiple SoC evaluation task, leading to a high-performance battery pack state estimation algorithm in both average and extreme cell SoC. In particular, the proposed methodology aims to correlate the SoC estimation of the least/most charged cell by means of the ASR-UKF with the average pack voltage in order to achieve the SoC at pack level, which represents an important indicator of the energy utilization of the whole battery pack.
In ideal conditions, a relationship between voltage variation and SoC difference can be identified for a battery model, since the OCV-SoC characteristic is a monotonic curve. In detail, the variation of the SoC (ΔSoC) occurring in case of the experienced voltage difference ΔV is computed as follows:

$$\Delta SoC = \frac{\Delta V}{S_V} \tag{4.6}$$

where S_V is the voltage sensitivity with respect to the SoC.
In a battery pack composed by n cells, S_V can be characterized, assuming to have a battery model that can approximate the behavior of each cell. Therefore, this relationship can be adopted for the SoC estimation of any cell by accurately knowing only one SoC in the pack. Moreover, the SoC at pack level is obtained as additional information by considering the deviation of the known cell state from the average voltage of the pack.
For this purpose, a second-order equivalent circuit model (ECM) has been experimentally calibrated for the cells and integrated in the ASR-UKF by means of lookup tables for all the cell parameters, each one composed by k values. Then, according to the cell model parameters, the voltage sensitivity with respect to the SoC (S_V) has been defined

as reported in equation (4.7), representing the expected rate of change of the cell voltage related to the SoC variation.

$$S_V = \frac{V_c(j+1) - V_c(j-1)}{SoC(j+1) - SoC(j-1)}, \quad j \in [2, k-1] \tag{4.7}$$

where V_c is the modeled cell terminal voltage, SoC is the cell State of Charge and j is the index in the lookup tables. Therefore, once identified the SoC of the least/most charged cell, the nearest index $j-1$ and $j+1$ are selected and the sensitivity S_V is calculated on the basis of the cell terminal voltages and SoCs corresponding to the index identified. Subsequently, a step-by-step computation of S_V is integrated within the ASR-UKF, leading to the equation (4.8). As result, the average pack SoC (SoC_{avg}) can be achieved as follows:

$$SoC_{avg} = SoC_{lm} - \frac{V_{lm} - V_{avg}}{S_V} \tag{4.8}$$

where SoC_{lm} is the SoC of the least/most charged cell estimated through the ASR-UKF, V_{lm} is the measured voltage of the least/most charged cell and V_{avg} is the pack voltage averaged over the number of cells that compose the whole battery pack.
The evaluation of the SoC of the least/most charged cell is achieved by considering the pack current and the minimum or the maximum cell voltage for the discharging or charging phase, respectively. All the considered voltage and current information are used in the SoC estimation by means of the ASR-UKF, according to the algorithm reported in table 4.4. More implementation details about the ASR-UKF algorithm can be found in [72, 77].

4.3.2 Numerical results

The proposed ASR-UKF has been implemented in Matlab®-Simulink with the aim of demonstrating its multiple SoC estimation capability. A 48 V battery pack has been modeled as plant model for the numerical analysis. In detail, the pack is composed by 14 series-connected cells, obtaining a battery with a nominal voltage of 51.8 V. A relevant amount of numerical tests have been performed considering different charging/discharging current profiles and imbalance conditions in terms of SoC and voltage differences among all the cells that compose the battery pack. Moreover, random noise has been added to the voltage and current measurements for the filters

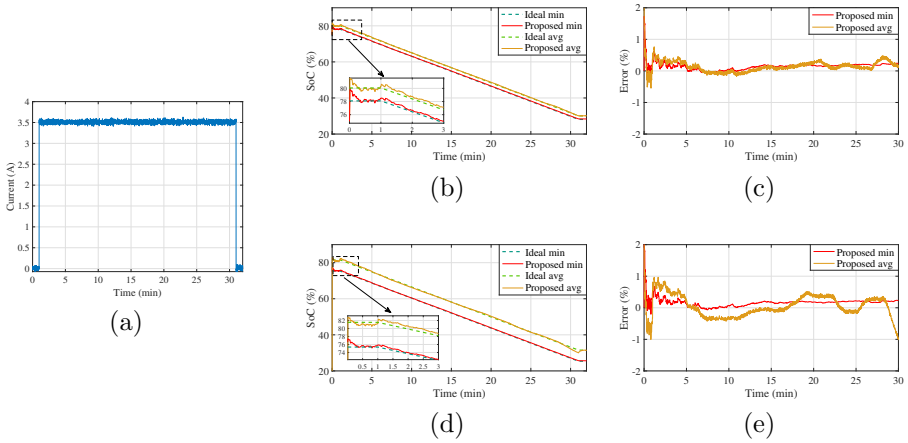

Figure 4.6: Numerical results: (a) 1C constant discharge current profile, (b-d) Average and minimum cell SoC estimated by means of the proposed methodology compared to the SoC estimated with the ideal Coulomb Counting and (c-e) related estimation errors with respect to the Coulomb Counting method.

in order to reproduce the characteristics of commercial sensors. The performances of the algorithm have been evaluated by comparing the estimation results regarding the SoC of the least/most charged cell and the SoC at pack level with the Coulomb Counting method computed in ideal conditions considering the most unbalanced cell state and the average among all the SoCs as initial conditions, respectively.

Figure 4.6(a) shows a constant discharge current at 1C-rate imposed to the battery pack to validate the performances of the estimation algorithm. The impact of different imbalance conditions, in terms of initial SoC_0 value, on the performance of the filter has been evaluated by considering a maximum SoC difference of 2% and 7% between the least charged cell and the average of the battery pack. Figures 4.6(b) and 4.6(c) show the SoC estimation results and the errors with respect to the coulomb counting method for the first case, while figures 4.6(d) and 4.6(e) those for the worst imbalance case.

As shown in figures 4.6(c) and 4.6(e), the estimation performances are worsened with the increase of imbalance conditions in the battery pack. Nevertheless, the lowest voltage cell SoC estimation and the average pack SoC estimation are both limited in the $[-0.5\%;\ +0.5\%]$ error range with respect to the ideal Coulomb Counting, even in the

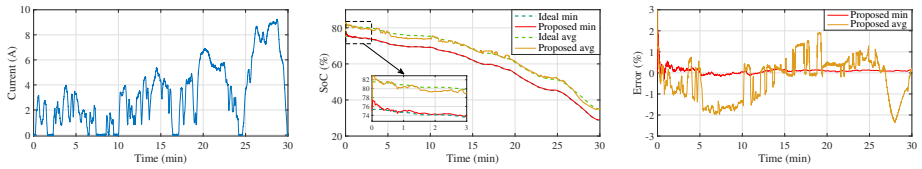

(a) (b) (c)

Figure 4.7: Numerical results for the WLTP current profile: (a) average and minimum cell SoC estimation results and (b) related estimation error with respect to the Coulomb Counting method.

case of extreme SoC discrepancy among the cells.
Further numerical analysis have been performed by considering the same battery pack subjected to similar initial state conditions. In detail, the maximum initial SoC imbalance was set at 7 % between the most and the least charged cells. Meanwhile, the rest of the cells have been randomly unbalanced in a 5% range around 80% as initial SoC value. A generic EV subjected to a WLTP driving cycle has been considered for the simulation, and figure 4.7(a) shows the current profile obtained by scaling down the power consumption to the battery pack voltage and current operating ranges.

In figure 4.7(b) the minimum and average SoC estimation performed by the proposed methodology is compared to the ideal Coulomb Counting method, whereas the estimation errors with comparison to the Coulomb Counting executed in ideal condition is reported in figure 4.7(c).

As possible to notice from figure 4.7(c), the least/most charged cell SoC estimation achieves the best performance, while the average pack SoC estimation is more sensitive to model inaccuracies when highly dynamic conditions are considered. However, the absolute error with respect to the ideal reference SoC is lower than 2%, thus leading to an effective knowledge of the energy available in the overall battery pack.

4.3.3 Real-Time implementation

In real world applications, high cost-effectiveness ratios are usually required for the control section of a common BMS. For this reason, low cost Digital Signal Processors (DSP) are commonly chosen as microcontrollers for monitoring the battery pack and controlling the hardware section of the BMS.

Table 4.8: Comparison between different microcontrollers.

	STM32G484	TMS320F28335	ATSAM3X8E
Manufacturer	STMicroelectronics	Texas Instruments	Microchip
Processor	ARM Cortex M4	C2000 DSP	ARM Cortex M3
Operating frequency	170 MHz	150 MHz	84 MHz
Flash memory	512 kB	512 kB	512 kB
RAM	128 kB	64 kB	96 kB
Single precision FPU	yes	yes	no
32-bit timers	2	3	1

The main suitable solutions among all the microcontrollers available on the market and their main characteristics are summarized in table 4.8.

The implementation of advanced state observers for the SoC and the SoH estimation tasks, which are required to be run in real time, may need high programming effort to fulfill time execution and memory restrictions [103]. Moreover, the implementation of a battery model, such as the second-order ECM, usually require a significant amount of flash memory for storing the model parameters in the form of lookup tables.

For the proposed methodology, a 1 second timer interrupt dedicated to the ASR-UKF has been adopted for ensuring the real time execution and some changes were made to the code in order to optimize the use of the microcontroller resources. In addition, the target C code has been generated by means of the MATLAB coder tool, selecting the toolchain of the specific microcontroller manufacturer, in order to avoid misalignment and errors in the final execution code. The optimization of the code has been achieved by adopting the following main changes with respect to the code executed in the Matlab® environment:

- all the division operation were changed to multiplications;
- inline functions were preferred;
- all the double-precision variables were converted in single-precision data type (i.e. *float* type in the compiler environment);
- the local defined variables were preferred to the global ones.

The final target code resulted in a memory allocation of about 20 kB for the flash memory section and 3 kB for the RAM section.

Moreover, the adoption of single-precision variables allows for taking advantage of the floating point unit (FPU) of some microcontrollers. Therefore, the two platforms from the Texas Instruments and the STMicroelectronics manufacturers resulted the best choices, according to their specification in table 4.8. Finally, the TMS320F28335 has been adopted for the experimental analysis since its resources, in terms of RAM, flash memory and computational capability, satisfied the requirements of the generated execution code.

4.3.4 Experimental results

An experimental setup has been carried out for validating the proposed methodology by means of Hardware-In-the-Loop (HIL) testing approach. In figure 4.8 a block diagram of the developed HIL setup is reported. The hardware under test is represented by the microcontroller performing the SoC estimation task, while a Typhoon HIL 404 has been adopted as HIL simulator for emulating the battery pack model.

A 48 V battery pack, composed by 14 Lithium-ion cells, has been implemented in the Typhoon HIL Control Center software as plant model. Each cell model is represented by an independent second-order ECM of the same EFEST IMR 18650 battery cell considered in the numerical analysis. Moreover, each model parameter is updated in real-time by means of lookup tables to reproduce its dependency to the actual SoC and C-rate, thus resulting time-variant during the execution of the tests. An exhaustive HIL validation has been performed by implementing a large amount of operating conditions in several test scenarios. In detail, different initial values in terms of SoC and voltage were considered for the cells to simulate various unbalancing conditions in the battery pack. Considering the input current of the battery pack, the terminal voltages are obtained from the execution of the cells ECMs and subsequently sent to the analog output of the Typhoon HIL 404, where the real-time emulation by means of the integrated 16-bit DAC takes place.
As shown in figure 4.9, a Texas Instruments TMS320F28335 evaluation board has been adopted to perform the BMS functionalities. The board is characterized by a 32 bit C2000 Digital Signal Processor (DSP) with a clock speed of 150 MHz mounted. As mentioned in section 4.3.3, in order to implement the developed estimator in the microcontroller, the MATLAB coder tool has been adopted. It allows for generating the target C code starting from a Matlab code

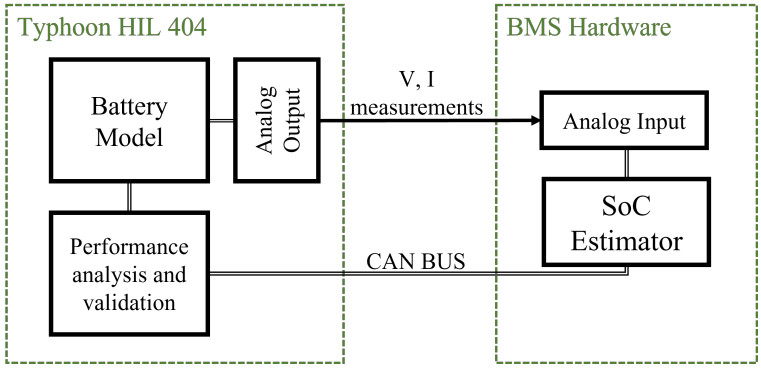

Figure 4.8: Block diagram of the Hardware-In-the-Loop setup.

script, avoiding misalignment and errors in the final execution code. Moreover, a 1 s time step interrupt has been set for the filter real time updating, while the voltages and the battery current have been acquired in a faster interrupt task (1 ms of time step).
The cell voltages have been scaled down by means of resistor dividers in order to make them suitable for the 12 bit ADC of the microcontroller, whereas a generic 20 A full-scale current transducer have been emulated in the HIL simulator by considering a $1/7$ V/A scaling factor for the current measurement. Besides the estimators, a CAN BUS communication line has been set between the HIL simulator and the BMS which enables the real time monitoring of the test execution and the results from the microcontroller by means of a custom graphical interface. Hence, the SoC estimation results from the proposed methodology have been compared with the ideal SoC profiles from the cell models in the HIL simulator. In this way, the performances of the estimator can be evaluated by reproducing realistic battery conditions without involving any power line. The Typhoon HIL SCADA software has been adopted for automatically executing the test profile as well as acquiring the measurements and the estimation results during the experimental tests.
The same current profiles adopted for the numerical analysis have been considered for the experimental tests as well, as shown in figures 4.10(a) and 4.10(d). A maximum imbalance of 7% in terms of SoC has been considered between the battery cells as initial condition, since it resulted as the worst case from the numerical analysis. In detail, the initial SoC values of the fourteen cells in the battery pack have been randomly set in the range $80\% \div 82\%$, whereas the least charged cell has been initialized with a $SoC_0 = 75$ %.

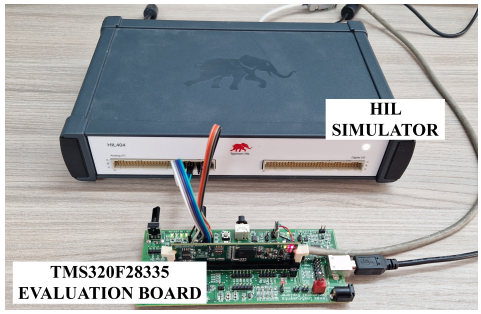

Figure 4.9: Picture of the adopted Hardware-In-the-Loop setup for the experimental analysis.

Figure 4.10(b) shows the results achieved from the experimental test when the pack is subjected to a 1C constant discharge current, while in figure 4.10(c) the errors of the minimum and average SoC estimation are reported. The error is computed with respect to the ideal reference SoCs from the least charged cell and the averaged value in the battery pack. These two reference profiles are included in the battery pack model and real-time computed in the HIL simulator, allowing the Typhoon SCADA software to concurrently analyze and validate the algorithm performances while logging the results for eventual post-processing analysis. As can be noticed in the zoomed initial minutes, the convergence time of both the estimators is very short and the ASR-UKF maintains an estimation error lower than 0.5% in absolute value for the least charged cell in all the performed tests. On the other hand, the average SoC estimation deviates in a $\pm 2\%$ range from the true value.

Figures 4.10(e) and 4.10(f) show the obtained results when the plant is subjected to a WLTP-shaped load current. The test represents a highly dynamic scenario and it is considered as the closest representation of a real-world application. It is worth to notice that the profile is significantly different from the commonly adopted modeling procedures as well, thus leading to a reduced accuracy of the considered model. The estimation of the minimum SoC cell confirmed the same results of the constant discharge test. On the other hand, despite the evident noise in the obtained SoC profile, the average SoC estimation task has shown a result within the $\pm 2\%$ range around the reference value in the overall test profile. Therefore, the experimental analysis confirmed the effectiveness of the proposed methodology in a wide operating conditions for achieving an accurate knowledge of the

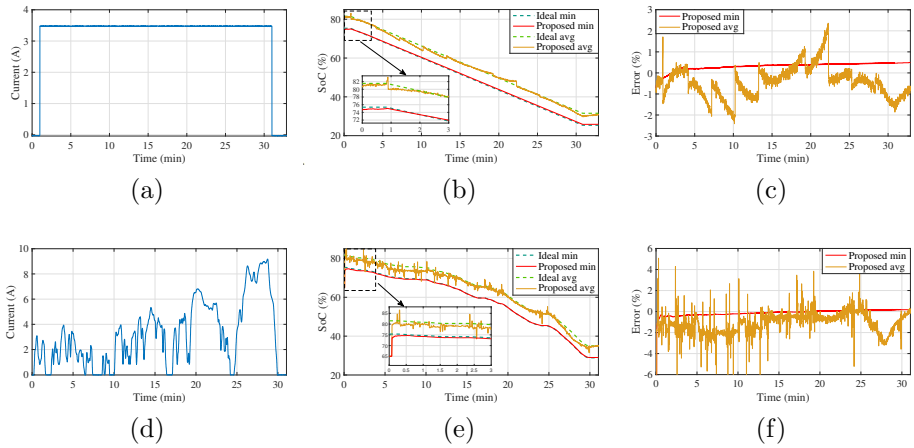

Figure 4.10: HIL testing results: (a-d) load current profiles imposed to the battery pack, (b-e) average and minimum cell SoC estimated by means of the proposed methodology compared to the SoC estimated with the ideal Coulomb Counting and (c-f) related estimation error with respect to the Coulomb Counting method.

extreme cell state in the battery pack, while giving information about the pack overall state and average available energy.

4.4 Supercapacitor SoC Estimation

As stated before, the accurate knowledge of SoC of the storage systems involved in a HESS is of paramount importance. In particular, if a battery/supercapacitor hybrid storage system is considered, the accurate SoC estimation allows for maximizing system performance and improving energy management strategies while ensuring safe operating conditions. However, the state of charge of a supercapacitor is not immediate to estimate, since its stored energy is not directly measurable due to internal nonlinear phenomena.
In order to investigate advanced methods for supercapacitor SoC estimation, both the models mentioned in 3.2.6 have been integrated with an Adaptive Square-Root Unscented Kalman Filter (ASR-UKF). Therefore, the state estimation performance of the proposed algorithm have been evaluated and compared to the main conventional methods commonly adopted for evaluating the stored energy in supercapacitors.

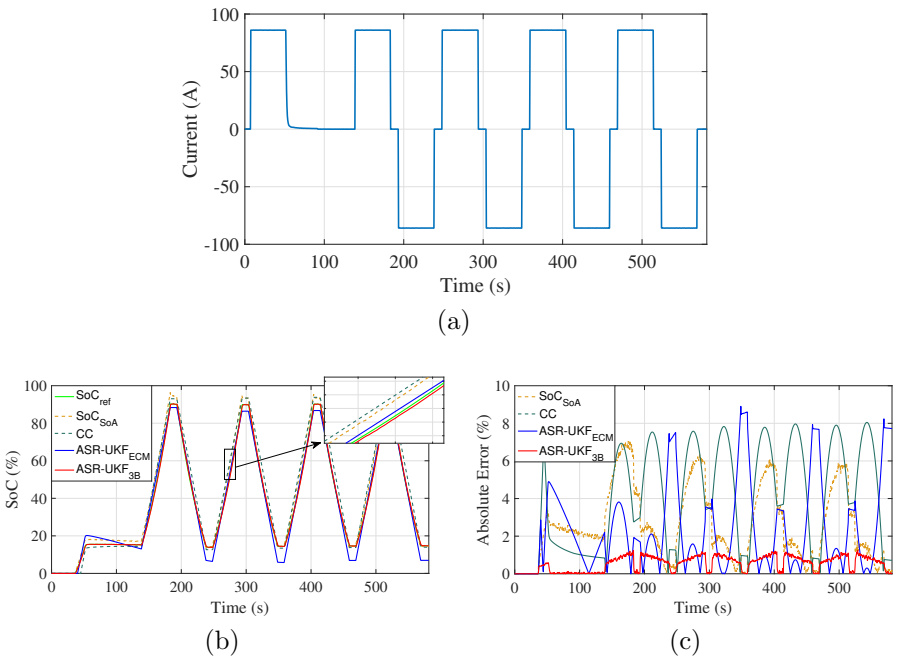

Figure 4.11: Numerical results for SoC estimation: (a) Current profile, (b) SoC estimation results and (c) errors with respect to the ideal SoC reference.

4.4.1 Numerical Results

To compare their performances, all the SoC estimation methods mentioned in section 3.1.2 have been implemented in Matlab-Simulink. The three-branches model and the first-order ECM have been both implemented as a plant model for simulating the supercapacitor behavior. Their model equations have been included in two different ASR-UKF for evaluating the impact of the two modeling approaches in SoC estimation methods. In addition, random noise has been added to voltage and current measurements for reproducing realistic operating conditions. Similar to the modeling procedure, a constant current is imposed on the SC for precharging it to the minimum operating voltage. After a resting time, a sequence of charging and discharging pulse current is adopted for testing the performances of the estimation algorithms, as shown in figure 4.11(a). The SoC estimation results obtained from the four SoC computation methods are shown in figure 4.11(b). As can be seen from the absolute errors with re-

spect to the ideal reference SoC shown in figure 4.11(c), the proposed ASR-UKF guarantees the best estimation performances if the three-branches model is considered for representing the supercapacitor dynamic behavior.

4.4.2 Experimental Results

An experimental setup has been carried out to validate the proposed SoC estimation algorithm. The ASR-UKF has been implemented with both the models described in sections 3.2.5. A comparison between their performance and the conventional methods, namely the simple SoC definition and the Coulomb Counting, has been performed. Since the internal states of the DUT cannot be accessed, the supercapacitor behavior exhibited in experimental tests has been replicated in the Simulink environment and the computation of the SoC, based on the ideal internal supercapacitor voltages, has been regarded as the true SoC reference SoC_{ref}. Moreover, the SoC resulting from the Coulomb Counting method and the one resulting from the ASR-UKF implementing the first-order ECM have been scaled in the operating range of the SC, thus obtaining a relative indication for a better comparison between the different methods.
The absolute value of the error with respect to the reference, computed as in equation (4.9), has been considered as a performance indicator for each estimation method.

$$\varepsilon = |SoC_{est} - SoC_{ref}| \tag{4.9}$$

where SoC_{est} is the estimated SoC.
The experimental measurements were obtained from the Eaton supercapacitor.
The supercapacitor has been connected to a Spitzenberger&Spies DM 15000 PAS amplifier used as bidirectional current source, depending on the imposed current profile. The power amplifier is controlled by a Novacor RTDS real-time simulator to elaborate all the necessary signals to automatically perform the tests. Voltage and current waveforms were measured and logged with a Zes-Zimmer LMG671 Power Analyzer by means of voltage dividers and current transducers. The estimation methods have been initially validated by means of an offline execution in the Simulink environment. The current and voltages acquired during experimental tests have been reproduced in simulation and the current profile adopted for characterizing the first model (figure 4.11(a)) has been considered for the comparison of different SoC

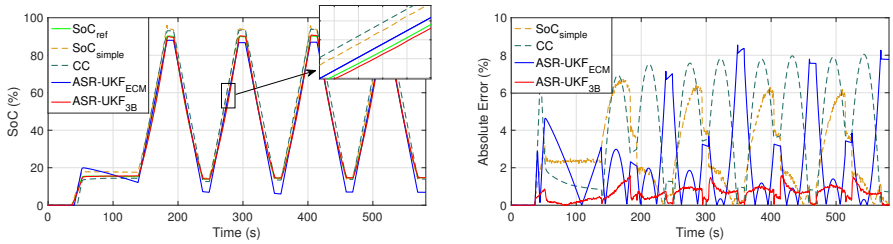

(a) (b)

Figure 4.12: Experimental results for SoC estimation: (a) SoC estimation results and (b) errors with respect to the ideal SoC reference.

estimation methods for Supercapacitors as well. The results obtained in the first test are shown in figure 4.12, where each SoC estimation is compared to the reference ideal SoC profile and the absolute error is considered as a performance indicator.

The proposed algorithm, which includes the supercapacitor three-branches model, allows for achieving the lowest estimation error during the entire test case. Indeed, a maximum error between 6% and 8% is achieved by the Coulomb Counting and the simple capacity methods. Similarly, the estimation error of the ASR-UKF, implemented with the first-order dynamic equivalent circuit model, reaches a peak value above 8%. On the other hand, if the three-branches model is considered for representing the supercapacitor dynamic behavior, the proposed estimator ensures an error lower than 2% with respect to the supercapacitor SoC computed in ideal conditions.

Subsequently, all the SoC estimation methods mentioned in section 3, have been implemented in an Opal OP5700 real-time simulator and the KFs execution time step was set to 0.5 s, while the CC and the SoC_{simple} computations were executed at 50 μs. Figure 4.13 shows the results obtained during a real-time execution of the algorithms while the SC was subjected to a charging/discharging cycle between the minimum and the maximum operating voltage.

As shown in figure 4.13(b), the conventional methods show the same error range obtained in the previous test and a more noisy result is due to the higher voltage measurement noise in the setup. The proposed estimator achieves a more stable SoC estimation and the maximum error is maintained in the nearest of 2%, thus confirming the previous results.

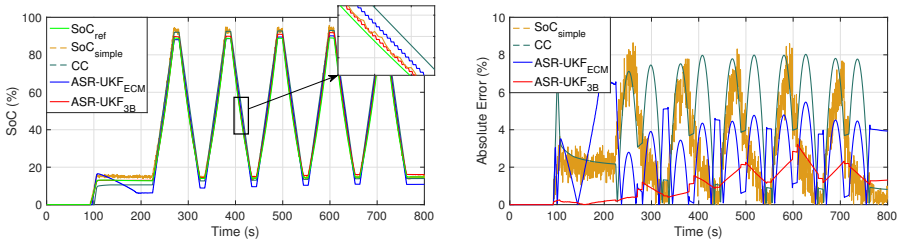

(a) (b)

Figure 4.13: Experimental results for real-time SoC estimation: (a) SoC estimation results and (b) errors with respect to the ideal SoC reference.

4.4.3 Experimental Validation under realistic grid power profiles

Further experimental tests have been performed considering a 1-hour time window extracted from a standard daily power profile measured in a German MV/LV substation [115]. As a plant model, a HESS has been considered, which includes a Supercapacitor module and a Lithium-Ion battery pack, adopting a Low-Pass Filter (LPF) control strategy for allocating the power profiles to the ESS technologies. Moreover, the supercapacitor reference power profile has been scaled down to the EATON SC voltage and current operating ranges, in order to reproduce in a real-time experimental setup the same scenario experienced in the MV/LV substation. In figure 4.14 the daily power profile is shown, where the 1-hour time window considered in the test is highlighted. The extracted 1-hour power profiles allocated to the battery and the supercapacitor by means of the low-pass filter are depicted in figures 4.14(b) and 4.14(c), respectively. Figure 4.14(d) shows the supercapacitor current profile imposed by the power amplifier during the experimental test. It has been obtained by scaling down the power profile to the supercapacitor operating range and dividing the power by the rated voltage of the device.
In figure 4.14(e), the supercapacitor SoC computed in ideal condition and selected as true reference value and the one estimated by the two conventional methods as well as the estimation performed by the proposed method are shown. As shown in figure 4.14(f), similar results to the previous tests have been confirmed. The simple capacity model reflects the voltage measurement noise, while the Coulomb Counting method error is included in the $6\% - 8\%$ range. On the other hand,

with the proposed ASR-UKF, the error is reduced from the $2\% - 4\%$ range to below 1.5% during the entire test when the three-branches model is considered, thus confirming the better performances in a realistic scenario as well.

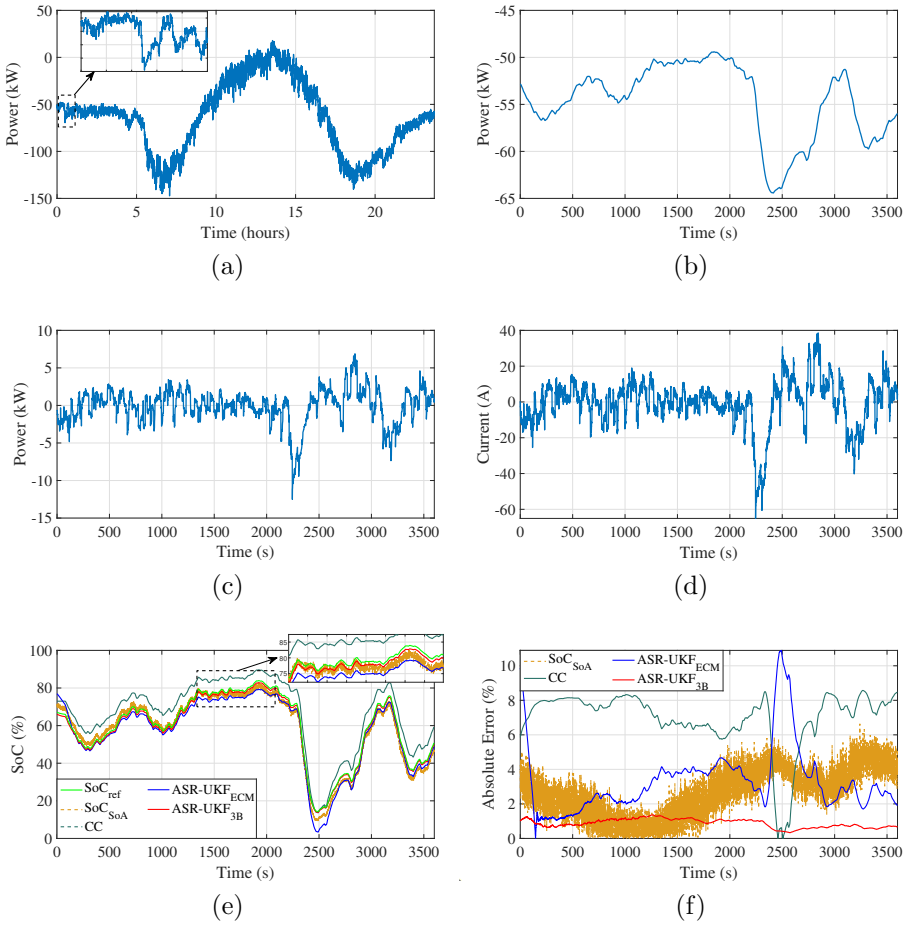

Figure 4.14: Experimental results for SoC estimation of supercapacitor in a HESS: (a) daily power reference profile in a German MV/LV substation and considered 1-hour window; (b) power profile allocated to the battery; (c) power profile allocated to the SC; (d) SC current profile scaled down to its operating range; (e) supercapacitor SoC estimation results and (f) absolute errors with respect to the ideal SoC reference.

Chapter 5

Prototyping of Dual-Active-Bridge Converters

[Original contribute]

The development of a real DAB prototype have been included in the dissertation. In particular, a modular converter for battery and hybrid storage interconnection has been designed and implemented. The development process has been conducted through the fundamental steps of numerical modelling, design and testing. Furthermore, advanced modulation techniques and high performance control strategies have been investigated. The prototype have been finally implemented with the aim of validating the control strategy in a real application.

5.1 DAB Modelling

As discussed in section 2.2.2, the Dual Active Bridge (DAB) is a promising choice in many application fields thanks to its achievable efficiency and power densities. As shown in figure 5.1, the converter is composed by two full bridge circuits connected by an high-frequency transformer and an auxiliary inductance (L). The waveform of the two voltages generated by the bridges determine a power transfer through the transformer, while the auxiliary inductance helps in performance improving by extending the Zero-Voltage Switching (ZVS) operating range of the converter [116].

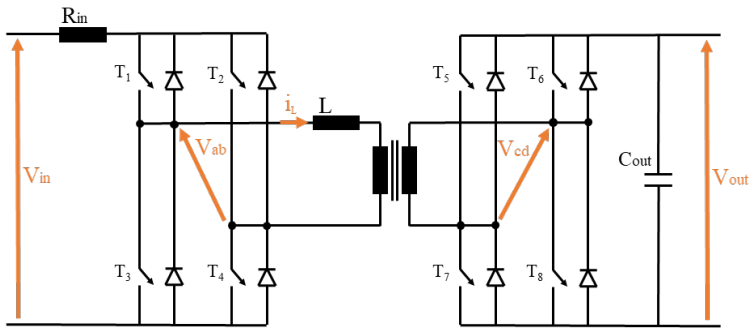

Figure 5.1: Dual Active Bridge converter topology.

5.1.1 Ideal Model

For a properly controlled power transfer, AC voltages $v_{ab}(t)$ and $v_{cd}(t)$ must be imposed on the inductor and on the transformer by the two voltage sourced H-bridges. As shown in figure 5.2, the two bridges can be replaced by the respective voltage sources $v_{ab}(t)$ and $v_{cd}(t)$ when considering the simplest representation of a DAB converter.
In the ideal model, the following assumptions can be considered:

- the transformer stray inductance is merged in the inductor L;
- all losses are neglected;
- input and output supply voltages (V_1 and V_2) are considered constant;
- ideal static switches are considered in the bridges and their transients are neglected;
- all the parasitic terms involved in the real system are neglected.

On these considerations, three voltage levels are possible to actuate at the output of the two H-bridges, as follows.

$$v_{ab} = \begin{cases} +V_1 & T_1, T_4 = 1 \quad T_2, T_3 = 0 \\ 0 & T_1, T_2 = 1 \quad T_3, T_4 = 0 \\ 0 & T_1, T_2 = 0 \quad T_3, T_4 = 1 \\ -V_1 & T_1, T_4 = 0 \quad T_2, T_3 = 1 \end{cases} \tag{5.1}$$

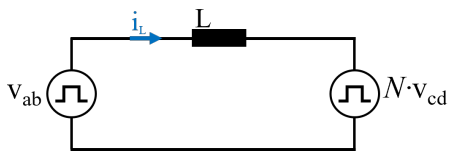

Figure 5.2: Ideal lossless DAB model.

where the state 0 indicates that the power switch is open, while 1 means closed. Similarly, the possible voltage levels at the secondary side of the transformer can be defined:

$$v_{cd} = \begin{cases} +V_1 & T_5, T_8 = 1 & T_6, T_7 = 0 \\ 0 & T_5, T_6 = 1 & T_7, T_8 = 0 \\ 0 & T_5, T_6 = 0 & T_7, T_8 = 1 \\ -V_1 & T_5, T_8 = 0 & T_6, T_7 = 1 \end{cases} \tag{5.2}$$

Referring to the simple model shown in figure 5.2, the voltage imposed on the inductor results as in equation (5.3).

$$v_L = v_{ab} - N \cdot v_{cd} \tag{5.3}$$

where N is the turns number of the high frequency transformer. The resulting inductor current is derived as follows.

$$i_L(t) = i_{L,0} + \frac{1}{L} \int_{t_0}^{t} v_L(t) dt \tag{5.4}$$

where $i_{L,0}$ is the initial current at time t_0. The instantaneous power generated or absorbed by the input and output voltage sources is easily computed by knowing the current $i_L(t)$ and the two voltages $v_{ab}(t)$ and $v_{cd}(t)$.
Considering a switching period T_s, the average power can be calculated for both the sources:

$$P_{ab} = \int_{t_0}^{T_s} v_{ab}(t) \cdot i_L(t) dt \tag{5.5}$$

$$P_{cd} = \int_{t_0}^{T_s} v_{cd}(t) \cdot i_L(t) dt \tag{5.6}$$

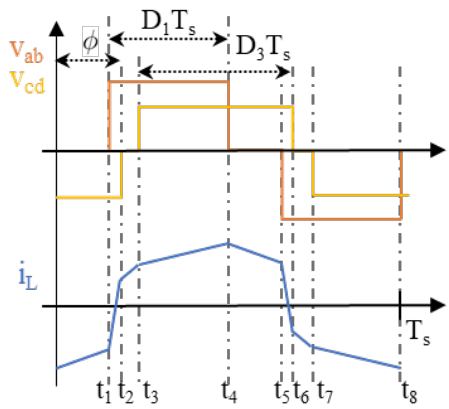

Figure 5.3: Inductor voltages and current during a switching period with generic phase-shift and duty cycles.

Since the ideal DAB model is lossless, the two average powers equal each other in absolute value ($|P_{ab}| = |P_{cd}|$). The period T_S can be easily split in m shorter time intervals including constant voltages v_{ab} and v_{cd} to simplify the maths. Once the physical components of the converter are defined, the average power is affected by the following four parameters, which are able to act on the duration of the constant-voltage time intervals:

- the phase shift between the two H-bridges (ϕ expressed in radiants)
- the duty cycle between the two legs of the input bridge (D_1)
- the duty cycle between the two legs of the output bridge (D_3)
- the switching frequency of the power switches (f_s)

The mentioned parameters in a switching cycle are shown in figure 5.3.

5.1.2 Phase-shift modulation

The basic single phase-shift modulation (PS) has been selected as reference due to its implementation simplicity and low computational cost for an extended load range. With the adoption of this modulation,

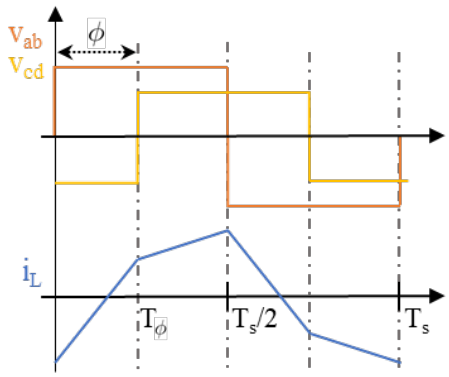

Figure 5.4: Inductor voltages and current during a switching period at steady-state operation considering a single phase-shift modulation.

the DAB is operated at constant switching frequency and maximum duty cycles ($D_1 = D_3 = 0.5$) in order to achieve the maximum operating range in terms of transfer power. The phase shift between the two converter bridges (ϕ) is only considered as control parameter to vary the output power. With the two H-bridges working at maximum duty cycle, the zero-voltage levels are not possible to be actuated on the inductor L, and the two voltages v_{ab} and v_{cd} can only assume the values $\pm V_{in}$ and $\pm V_{out}$, respectively.
Figure 5.4 show the steady-state voltage and current inductor waveforms when the converter is operated under phase-shift modulation. T_ϕ is the time period related to the phase shift, and it is computed as follows.

$$T_\phi = \frac{\phi}{2\pi f_s} \tag{5.7}$$

As possible to notice, the voltage and current quantities are repeated with opposite sign at each half switching period. Therefore, the transferred power P_t can be calculated by considering only the first half of the switching period T_s, as follows.

$$P_t = \frac{2}{T_s}\int_0^{T_s/2} v_{ab}(t)\cdot i_L(t)dt = \frac{2V_{ab}}{T_s}\int_0^{T_s/2} i_L(t)dt \tag{5.8}$$

When the phase shift is positive ($0 < \phi < \pi$), the inductor current can be worked out as follows.

$$i_L(t) = \begin{cases} i_{L0} + (V_{in} + NV_{out}) \cdot t/L & 0 < t < T_\phi \\ i_{T_\phi} + (V_{in} - NV_{out}) \cdot (t - T_\phi)/L & T_\phi < t < T_s/2 \end{cases} \tag{5.9}$$

where i_{L0} and i_{T_ϕ} are the inductor current at time $t = 0$ and $t = T_\phi$, respectively.
Considering the symmetry in the switching cycle, the current at time $t = 0$ is obtained from equations (5.7) and (5.9), resulting:

$$i_{L0} = \frac{(\pi - 2\phi)NV_{out} - \pi V_{in}}{4\pi f_s L} \tag{5.10}$$

Extending the equations to the full range of the phase shift ϕ, the transferred power as function of the phase-shift is obtained, as follows.

$$P_t = \frac{NV_{in}V_{out}\phi(\pi - |\phi|)}{2\pi^2 f_s L} \qquad -\pi < \phi < \pi \tag{5.11}$$

where a $P_t > 0$ represents a power transfer from the input to the output port, and vice versa for $P_t < 0$.
The maximum power transfer achievable with a single phase-shift modulation can be worked out from equation (5.11) as follows.

$$|P_{PSmax}| = \frac{NV_{in}V_{out}}{8 f_s L} \qquad with \quad \phi = \pm\frac{\pi}{2} \tag{5.12}$$

Equation (5.12) is commonly adopted for deriving the maximum value of inductance L when the converter power is a requirement in the design.
As can be noticed in figure 5.5, the output power is directly proportional to the phase shift only in the range $-\pi/2 \leq \phi \leq \pi/2$, which is delimited by the maximum converter power. Therefore, only the mentioned operating range is considered to guarantee stability in the system. In addition, the phase shift value required for achieving a known power transfer P_{ref} is worked out from equation (5.11), as follows.

$$\phi = sign(P_{ref}) \cdot \frac{\pi}{2}\left(1 - \sqrt{1 - \frac{8 f_s L |P_{ref}|}{NV_{in}V_{out}}}\right) \tag{5.13}$$

Since the single phase-shift is capable of reaching the highest power level among all the possible modulations, the mentioned equations are

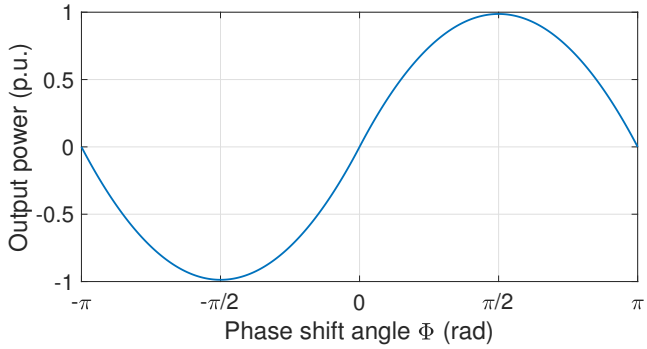

Figure 5.5: Transferred power in per unit for a DAB operated under single phase-shift modulation.

adopted in the design process for meeting the basic project requirements.
The modulation is characterized by simplicity and easy implementation, since only the phase-shift angle between the two bridges has to be adjusted to control the actual output power of the converter. Moreover, the single phase-shift is widely adopted due to the low computational effort required. However, high conduction losses and a limited Zero-Voltage-Switching (ZVS) operation represent the main drawbacks [117].

5.1.3 Advanced Modulation Techniques

The main weaknesses of the phase-shift modulation are related to low efficiency, high transformer RMS current and electric components stress. Since these drawbacks are intensified at low power operating points and especially when the input and output voltages are mismatched, alternative modulation techniques are worth investigating [118].

The Triangular and Trapezoidal Current Mode Modulation (TTCM) has the capability of ensuring the ZCS operation and a potential reduction of the inductor RMS current. In particular, in case of limited power range and sufficient difference between the voltages at the input and output ports of the converter, the triangular current mode can be applied, leading to a reduction of the inductor RMS current. Otherwise, trapezoidal current mode is operated and higher power levels are reached with the negative consequence of losing the ZCS operation on the output port [118].

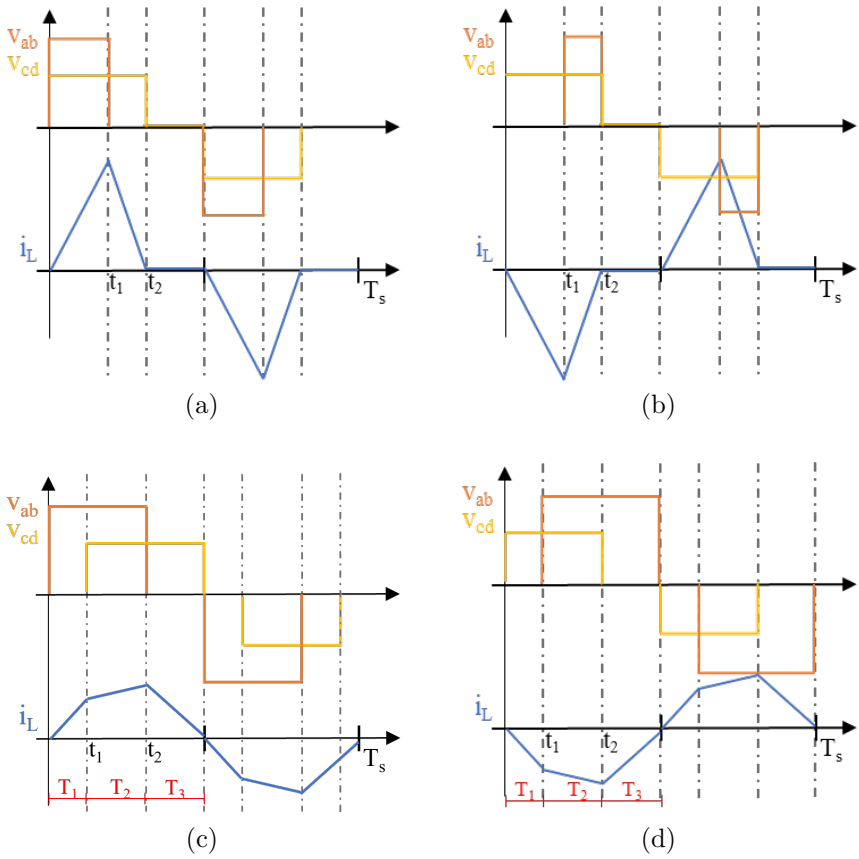

Figure 5.6: Inductor voltages and current during a switching period at steady-state operation for: (a) positive power transfer and triangular current mode, (b) negative power transfer under triangular current mode, (c) positive power transfer under trapezoidal current mode and (d) negative power transfer under trapezoidal current mode.

Figure 5.6(a) depicts the typical voltage and current waveforms for a positive power transfer from the input port to the output port of the converter. Considering $V_{in} > NV_{out}$, the inductor current is increased during the first time interval ($0 < t < t_1$), while in the second interval it is decreased to zero. In the second half-cycle the same behavior is repeated with opposite voltage and current sign.
The inductor current during the first half of the switching period can be determined, as follows.

$$i_L(t) = \begin{cases} 0 + \dfrac{V_{in} - NV_{out}}{L} \cdot t & 0 < t < t_1 \\ i_L(t_1) - \dfrac{NV_{out}}{L}(t - t_1) & t_1 < t < t_2 \\ 0 & t_2 < t < \dfrac{T_s}{2} \end{cases} \tag{5.14}$$

In order to switch both the bridges to zero voltage when the current is zero, the time instant t_2 can be determined as a function of t_1, as follows.

$$t_2 = \frac{V_{in}}{NV_{out}} \cdot t_1 \tag{5.15}$$

Therefore, the power transfer can be controlled by changing the duration of the time interval t_1.

$$P_t = \frac{2}{T_s} \int_0^{t_1} v_{ab} \cdot i_L(t) dt = \frac{V_{in}}{T_s} \frac{V_{in} - NV_{out}}{L} t_1^2 \tag{5.16}$$

The maximum power transfer is reached when the half switching period is met with the decreasing current time period, i.e. $t_2 = T_s/2$. Therefore, the value of the maximum increasing current time period and the power limit achievable by means of the triangular modulation are derived, as follows.

$$t_{1,MAX} = \frac{NV_{out}}{V_{in}} \cdot \frac{T_s}{2} \tag{5.17}$$

$$P_{tri,MAX} = \frac{N^2 V_{out}^2 (V_{in} - NV_{out})}{4 f_s L V_{in}} \tag{5.18}$$

As possible to notice from equation (5.16), the transferred power is zero if $V_{in} = NV_{out}$ and it can be only positive if $V_{in} > NV_{out}$. However, a negative power transfer is achieved by swapping the two intervals in which V_{in} and NV_{out} are imposed to the transformer, as shown

in figure 5.6(b). Similarly to the previous case, the equations can be rearranged, as follows.

$$i_L(t) = \begin{cases} 0 - \dfrac{NV_{out}}{L} \cdot t & 0 < t < t_1 \\ i_L(t_1) + \dfrac{V_{in} - NV_{out}}{L}(t - t_1) & t_1 < t < t_2 \\ 0 & t_2 < t < \dfrac{T_s}{2} \end{cases} \tag{5.19}$$

$$t_2 = \frac{V_{in}}{V_{in} - NV_{out}} \cdot t_1 \tag{5.20}$$

$$P_t = -\frac{V_{in}}{T_s}\frac{V_{in} - NV_{out}}{L}t_1^2 \tag{5.21}$$

Therefore, the operating range of the triangular current mode modulation can be summarized:

$$-\frac{N^2V_{out}^2(V_{in} - NV_{out})}{4f_sLV_{in}} < P_{tri} < \frac{N^2V_{out}^2(V_{in} - NV_{out})}{4f_sLV_{in}} \tag{5.22}$$

As a consequence, the power range is either zero or close to zero if the input and output voltages are close to each other.
As discussed in [118], higher power levels can be reached by considering a trapezoidal current mode modulation. Typical waveforms of this case are shown in figures 5.6(c) and 5.6(d). Similarly to the triangular current mode, the maximum power limit can be worked out, as follows.

$$P_{TTCM,Max} = \frac{N^2V_{in}^2V_{out}^2}{4f_sL(V_{in}^2 + NV_{in}V_{out} + N^2V_{out}^2)} \tag{5.23}$$

As a result, the extended operating range is achieved with the adoption of the TTCM modulation which can be summarized as follows.

$$TTCM \begin{cases} |P| \leq P_{tri,MAX} & \text{Triangular current mode} \\ P_{tri,MAX} \leq |P| \leq P_{TTCM,MAX} & \text{Trapezoidal current mode} \end{cases}$$

Compared to other modulations, the TTCM presents lower current peak values with consequent decrease in conduction losses, while the

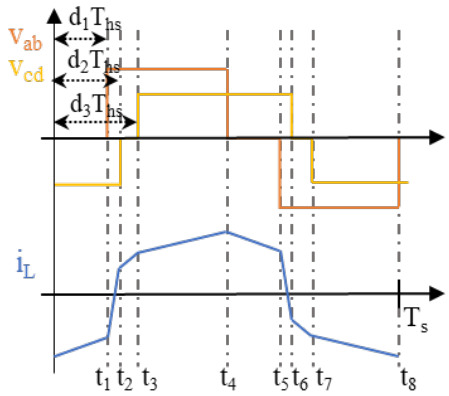

Figure 5.7: Inductor voltages and current during a switching period at steady-state operation under TPS modulation.

switching at zero current for low load condition leads to further increase of efficiency. However, the operating range in which the modulation can be actuated is limited with respect to the full power range of the converter and different modulation techniques have to be considered to optimize the converter operation under high load condition. Adding one or more degrees of freedom to the single Phase-Shift modulation, the Phase-Shift Pulse Modulation (PSPM) [119], the Dual Phase-Shift Modulation (DPS) and the Triple Phase-Shift Modulation (TPS) allow for maximizing the converter efficiency and extending the operating ZVS range [120]. In detail, the TPS represents the more general modulation by adopting three degrees of freedom in the control strategy. As a matter of fact, the PSPM and the DPS can be achieved as special forms of the TPS, depending on the choice of the duty cycles of the H-bridges [121]. Therefore, the converter model is extensively investigated by considering the more general case of TPS modulation.

With the TPS modulation, the three voltage levels illustrated in equations (5.1) and (5.2) can be imposed by the two H-bridges by considering all the possible combinations of duty cycles and phase shift, as shown in figure 5.7. The parameters d_1, d_2 and d_3 are defined as the duty cycle of the voltage v_{ab}, the phase shift between the two bridges and the duty cycle of v_{cd}, respectively.

The TPS extends the degrees of freedom in the DAB modulation by adopting the duty cycles of both the H-bridges as control variables, in addition to the phase-shift angle. As result, the TPS modulation can

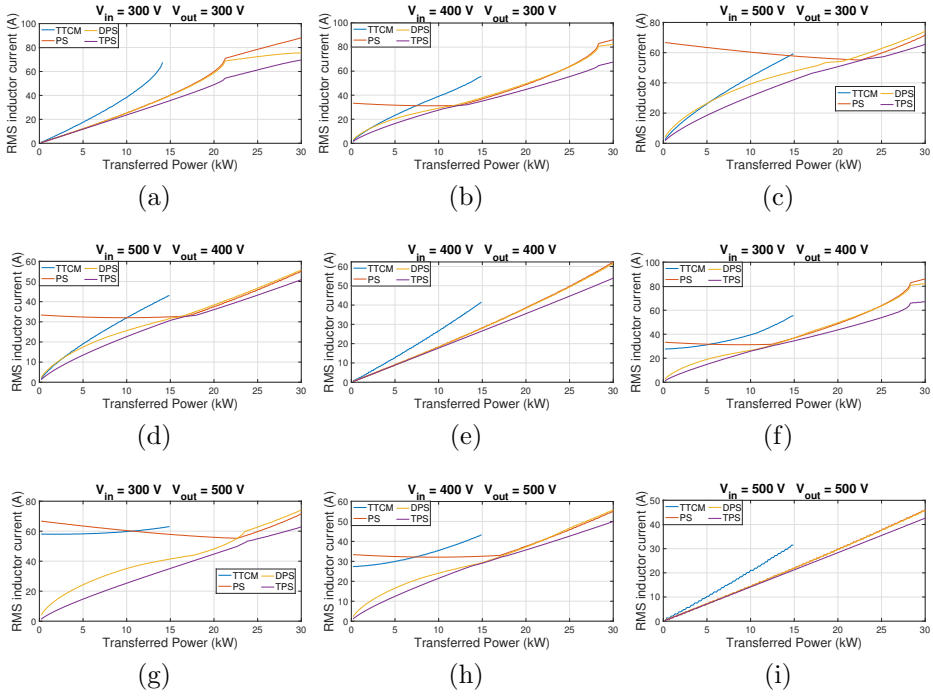

Figure 5.8: Variability of the RMS inductor current with respect to the output power for each modulation technique at different operating conditions, in terms of input (V_{in}) and output (V_{out}) voltage.

be considered as the most general case for a DAB converter, since any other modulation can be achieved by appropriately fixing to a constant value one of the three duty cycles. Therefore, only the assumption of TPS operation can lead to the most comprehensive converter model. Furthermore, the optimal operating point can be met by means of TPS modulation and further reduction in current stress and converter losses can be achieved with comparison to the other modulation techniques.

Figure 5.8 reports the variability of the RMS inductor current with respect to the output power for each modulation technique considering different operating conditions, in terms of input and output voltage levels. In detail, the possible combinations of three voltage levels (300, 400 and 500 V) at the input and otuput ports of the converter have been considered considered in the analysis. As result, the TPS modulation always achieves the lowest RMS current value and it is confirmed as the most general case among the possible techniques.

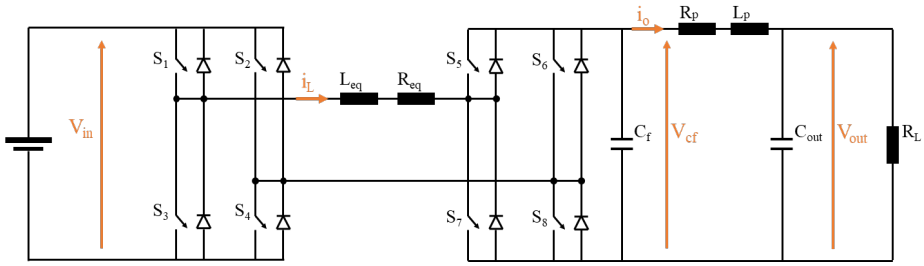

Figure 5.9: Equivalent circuit model of a Dual-Active-Bridge power converter including the output filter and a resistive load.

5.1.4 DAB Dynamic Model

A DAB dynamic model has been worked out by considering the equivalent electric circuit shown in figure 5.9. An ideal voltage generator is included for the input voltage source, whereas a resistive load R_L and a second order filter are considered at the output side.
In order to define the most general model for the considered converter, all the possible combinations related to the switches states are defined, as shown in figure 5.10. The value of the voltages imposed by the two H-bridges on the reactive tank R_{eq}-L_{eq} is dictated by the states of the high-side power switches on each bridge leg, since each respective low-side is always driven in the opposite state.

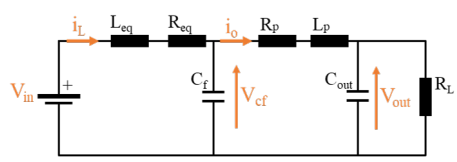

(a) case {1 0 1 0}

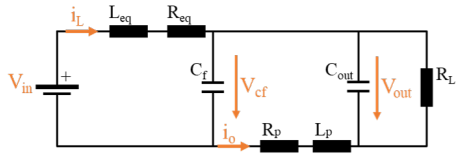

(b) case {1 0 0 1}

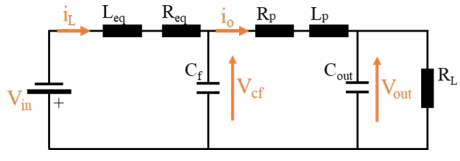

(c) case {0 1 1 0}

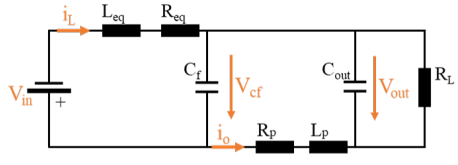

(d) case {0 1 0 1}

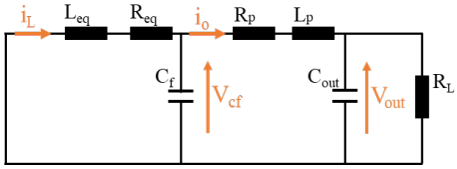

(e) case {1 1 1 0}

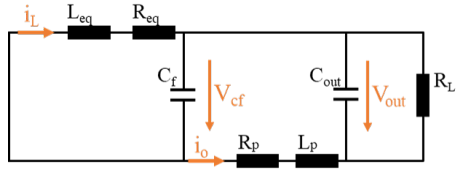

(f) case {1 1 0 1} or {0 0 0 1}

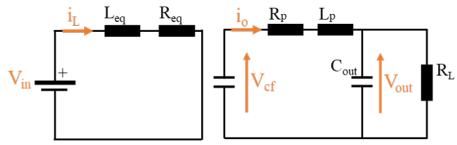

(g) case {1 0 1 1} or {1 0 0 0}

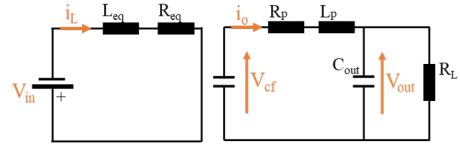

(h) case {0 1 1 1} or {0 1 0 0}

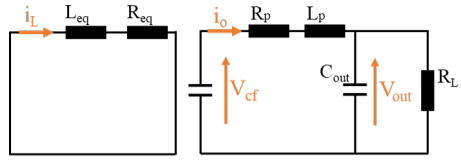

(i) case {1 1 1 1} or {1 1 0 0}
or {0 0 1 1} or {0 0 0 0}

Figure 5.10: Equivalent circuit models of a Dual-Active-Bridge converter with respect to the high side switches states $\{S_1 \quad S_2 \quad S_5 \quad S_6\}$.

As possible to notice, the main circuit schemes corresponding to the phase shift modulation are given by the combination of $\pm V_{in}$ and $\pm V_{out}$ and the circuit behavior is modelled by a fourth order dynamic model (figures 5.10(a-d)). On the other hand, two ideally separated equivalent circuits, characterized by a lower order dynamic, are identified when zero-voltage is imposed by the output bridge, as shown in figures 5.10(g-i).

Subsequently, the equivalent circuits shown in figure 5.10 can be generally summarized by defining the following equations.

$$i_L(t) = \begin{cases} \dfrac{di_L(t)}{dt} = (S_1 - S_2)\dfrac{V_{in}}{L_{eq}} - \dfrac{R_{eq}}{L_{eq}} i_L(t) - (S_5 - S_6)\dfrac{v_{cf}(t)}{L_{eq}} \\ \dfrac{di_o(t)}{dt} = \dfrac{v_{cf}(t)}{L_p} - \dfrac{R_p}{L_p} i_o(t) - \dfrac{v_{out}(t)}{L_p} \\ \dfrac{dv_{cf}(t)}{dt} = (S_5 - S_6)\dfrac{i_L(t)}{C_f} - \dfrac{i_o(t)}{C_f} \\ \dfrac{dv_{out}(t)}{dt} = \dfrac{i_o(t)}{C_{out}} - \dfrac{v_{out}(t)}{R_L C_{out}} \end{cases} \tag{5.24}$$

where S_k is the state of the k-th power switch and it equals 0 and 1 for the ON and OFF state, respectively.

The resulting fourth order differential equation system can be rearranged in the matrix form, as follows.

$$\dot{x}(t) = A(t)x(t) + B \tag{5.25}$$

where the state variable vector $x(t)$ is chosen as follows.

$$x(t) = \begin{bmatrix} i_L(t) \\ i_o(t) \\ v_{cf}(t) \\ v_{out}(t) \end{bmatrix} \tag{5.26}$$

and the matrices $A(t)$ and B are properly defined, as follows.

$$A = \begin{bmatrix} -\frac{R_{eq}}{L_{eq}} & 0 & -\frac{S_5 - S_6}{L_{eq}} & 0 \\ 0 & -\frac{R_p}{L_p} & \frac{1}{L_p} & -\frac{1}{L_p} \\ \frac{S_5 - S_6}{C_f} & -\frac{1}{C_f} & 0 & 0 \\ 0 & \frac{1}{C_{out}} & 0 & -\frac{1}{R_L C_{out}} \end{bmatrix} \tag{5.27}$$

$$B = \begin{bmatrix} (S_1 - S_2)\frac{V_{in}}{L_{eq}} \\ 0 \\ 0 \\ 0 \end{bmatrix} \tag{5.28}$$

The solution to the matrix system equation can be expressed as follows.

$$x(t) = C_1 e^{\lambda_1 t}\hat{v}_1 + C_2 e^{\lambda_2 t}\hat{v}_2 + C_3 e^{\lambda_3 t}\hat{v}_3 + C_4 e^{\lambda_4 t}\hat{v}_4 + x_P \tag{5.29}$$

where C_1, C_2, C_3 and C_4 are constant coefficients,λ_1, λ_2, λ_3 and λ_4 are the eigenvalues of matrix A and $\hat{v}_1$, $\hat{v}_2$, $\hat{v}_3$ and $\hat{v}_4$ are their respective eigenvectors. x_P is the vector of the particular solutions, which is defined as the steady state solution of the system equation (5.24) by neglecting all the derivative terms.
At each time interval in the switching period, equations in (5.24) change according to the power switch states S_1, S_2, S_5 and S_6. Therefore, the constant coefficients in equation (5.29) are computed at each time interval and the initial conditions $x(t_0)$ are taken from the last value of $x(t)$ evaluated during the previous time step. In particular, the constant coefficients as function of $x(t_0)$ and x_P are worked out by means of symbolic computation using a numerical solver. The resulting symbolic functions are then implemented in the dynamic model.
Moreover, a finite set of time-variant matrix A can be defined with respect to the finite number of combinations of the power switches states. Therefore, the eigenvalues and the eigenvectors can only be defined once for all the possible cases.
Similarly the same approach can be adopted to include in the model the dead time period, which generates additional equivalent circuits depending on the direction of the current flowing in the anti-parallel diodes other than the switches states.

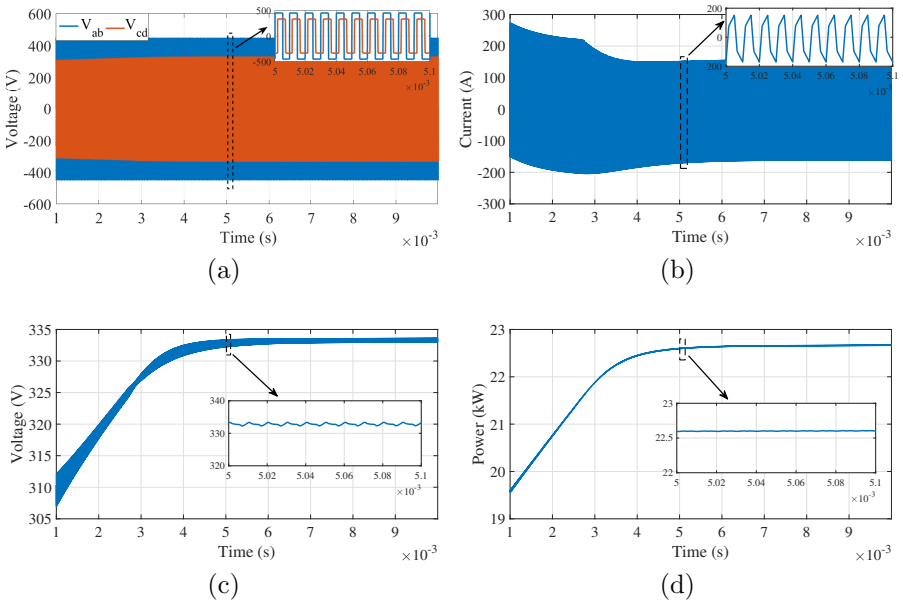

Figure 5.11: Simulation results of the Dual-Active-Bridge obtained from the developed model considering the single phase-shift modulation: (a) voltages imposed on the HF transformer (v_{ab} and v_{cd}), (b) inductor current i_L, (c) output voltage and (d) transferred power.

Afterwards, the obtained model has been implemented in a runtime script to be executed in Matlab®. Figure 5.11 depicts the results obtained from the runtime script when the model is operated under single phase-shift modulation. In detail, figures 5.11(a) and 5.11(b) show the imposed voltages and the resulted current in the reactive tank of the converter. On the other hand, the voltage and the transferred power at the output port are illustrated in figures 5.11(c) and 5.11(d).

Then, the equivalent circuit shown in figure 5.9 has been implemented in Matlab®-Simulink by means of the "simscape" blockset to perform a comparative analysis with the developed dynamic model. Figures 5.12(a) and 5.12(b) show the imposed voltages and the resulted current in the reactive tank of the converter, while the voltage and the transferred power at the output port obtained from the simscape simulation are illustrated in figures 5.12(c) and 5.12(d).
As can be noticed by comparing figures 5.11 and 5.12, the developed model reflects qualitatively the same behavior obtained in the simscape simulation environment. On the other hand, some quantitative

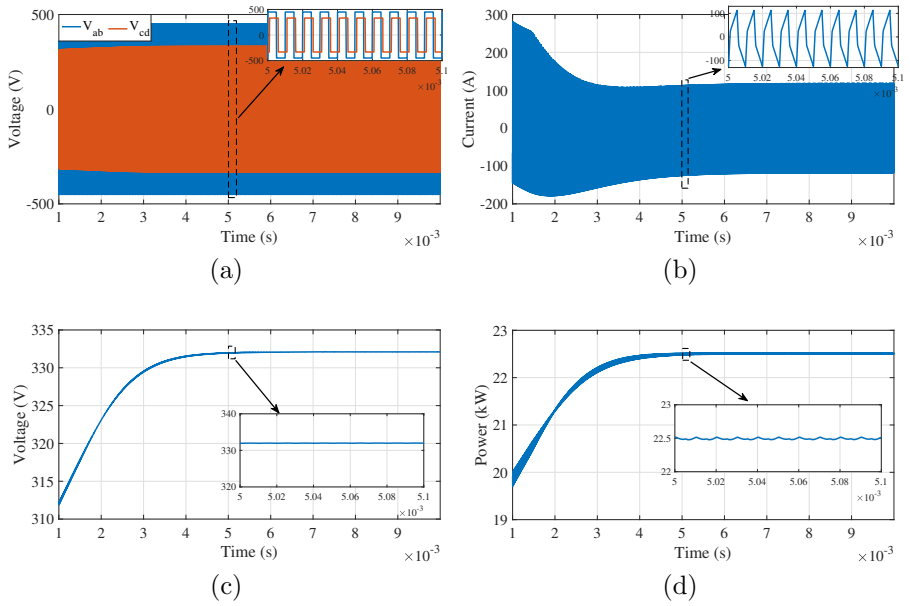

Figure 5.12: Simulation results of the Dual-Active-Bridge obtained from the simscape model considering the single phase-shift modulation: (a) voltages imposed on the HF transformer (v_{ab} and v_{cd}), (b) inductor current i_L, (c) output voltage and (d) transferred power.

differences occur due to the larger amount of non-ideal operating conditions included in the second simulation, since the simscape blockset presents more parameters to be set for the electrical components. However, the dynamic model results in less computational effort and thus it is more suited for longer numerical analyses while still representing accurate dynamic performances.

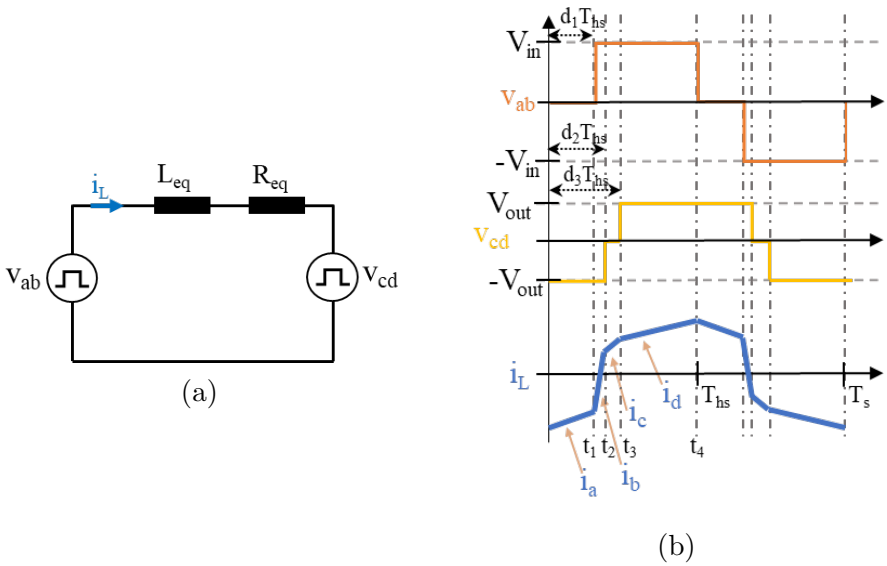

Figure 5.13: Simplified Dual-Active-Bridge model considering a generic Triple Phase-Shift modulation: (a) equivalent circuit and (b) voltages and current in the reactive tank, highlighting the constant-voltage time intervals.

5.1.5 DAB Average Model

As stated in the previous section, the TPS modulation resembles the most generic case in a DAB converter. It allows to exploit all the three output voltage levels of the input and output H-bridge with any combination of duty cycles. Therefore, the TPS modulation is considered to derive an average model of the converter for real-time implementation.

The case $0 < d_1 < d_2 < d_3 < 1$ is taken as an example for the analysis, and the typical current and voltage waveform of the DAB transformer are depicted in figure 5.13(b). The other possible cases are similar to each other and can be analyzed in the same way [121].

In order to simplify the calculations, the ideal model shown in figure 5.13(a) is considered, in which the R_{eq} includes the transformer winding resistance and the conduction resistance of the power switches. Meanwhile, L_{eq} includes the eventual auxiliary and the transformer stray inductance whereas a unit value $N = 1$ is considered for the transformer ratio.

At steady-state operation, the model is derived by dividing the switch-

ing period in time intervals during which the voltage across the reactive tank is constant.

$$i_L(t) = \begin{cases} i_a(t) & 0 \leq t \leq d_1 T_{hs} \\ i_b(t) & d_1 T_{hs} \leq t \leq d_2 T_{hs} \\ i_c(t) & d_2 T_{hs} \leq t \leq d_3 T_{hs} \\ i_d(t) & d_3 T_{hs} \leq t \leq T_{hs} \end{cases} \tag{5.30}$$

Then, the average value of the current i_L can be derived by means of a piece-wise integration in the switching period T_S, resulting in the following expression.

$$\begin{cases} i_a(t) = \dfrac{V_{out}}{R_{eq}} + \left(-I_{t4} - \dfrac{V_{out}}{R_{eq}} \right) e^{-\frac{R_{eq}}{L_{eq}} t} \\ i_b(t) = \dfrac{V_{in} + V_{out}}{R_{eq}} + \left(I_{t1} - \dfrac{V_{in} + V_{out}}{R_{eq}} \right) e^{-\frac{R_{eq}}{L_{eq}} (t - d_1 T_{hs})} \\ i_c(t) = \dfrac{V_{in}}{R_{eq}} + \left(I_{t2} - \dfrac{V_{in}}{R_{eq}} \right) e^{-\frac{R_{eq}}{L_{eq}} (t - d_2 T_{hs})} \\ i_d(t) = \dfrac{V_{in} - V_{out}}{R_{eq}} + \left(I_{t3} - \dfrac{V_{in} - V_{out}}{R_{eq}} \right) e^{-\frac{R_{eq}}{L_{eq}} (t - d_3 T_{hs})} \end{cases} \tag{5.31}$$

where I_{t1}, I_{t2}, I_{t3} and I_{t4} are the inductor current in the time instants t_1, t_2, t_3 and t_4, respectively. In ideal conditions, i.e. considering constant voltages V_{in} and V_{out} in the whole switching period, it results:

$$\begin{cases} i_a(0) = -I_{t4} \\ i_a(d_1 T_{hs}) = I_{t1} \\ i_b(d_2 T_{hs}) = I_{t2} \\ i_c(d_3 T_{hs}) = I_{t3} \\ i_d(T_{hs}) = I_{t4} \end{cases} \tag{5.32}$$

I_{t1}, I_{t2}, I_{t3} and I_{t4} are derived by substituting the equations (5.31) in (5.32), as follows.

$$I_{t1} = \frac{\frac{V_{out}}{R_{eq}} - \frac{V_{in}}{R_{eq}} e^{-\frac{R_{eq}}{L_{eq}} d_1 T_{hs}} - \frac{V_{out}}{R_{eq}} e^{-\frac{R_{eq}}{L_{eq}}(1+d_1-d_2)T_{hs}}}{1 + e^{-\frac{R_{eq}}{L_{eq}} T_{hs}}} + \\ + \frac{-\frac{Vout}{R_{eq}} e^{-\frac{R_{eq}}{L_{eq}}(1+d_1-d_3)T_{hs}} + \frac{V_{in}+V_{out}}{R_{eq}} e^{-\frac{R_{eq}}{L_{eq}} T_{hs}}}{1 + e^{-\frac{R_{eq}}{L_{eq}} T_{hs}}} \tag{5.33}$$

$$I_{t2} = \frac{\frac{V_{in}+V_{out}}{R_{eq}} - \frac{V_{in}}{R_{eq}} e^{-\frac{R_{eq}}{L_{eq}} d_2 T_{hs}} - \frac{V_{in}}{R_{eq}} e^{-\frac{R_{eq}}{L_{eq}}(d_2-d_1)T_{hs}}}{1 + e^{-\frac{R_{eq}}{L_{eq}} T_{hs}}} + \\ + \frac{-\frac{Vout}{R_{eq}} e^{-\frac{R_{eq}}{L_{eq}}(1+d_2-d_3)T_{hs}} + \frac{V_{in}}{R_{eq}} e^{-\frac{R_{eq}}{L_{eq}} T_{hs}}}{1 + e^{-\frac{R_{eq}}{L_{eq}} T_{hs}}} \tag{5.34}$$

$$I_{t3} = \frac{\frac{V_{in}}{R_{eq}} - \frac{V_{in}}{R_{eq}} e^{-\frac{R_{eq}}{L_{eq}} d_3 T_{hs}} - \frac{V_{in}}{R_{eq}} e^{-\frac{R_{eq}}{L_{eq}}(d_3-d_1)T_{hs}}}{1 + e^{-\frac{R_{eq}}{L_{eq}} T_{hs}}} + \\ + \frac{\frac{Vout}{R_{eq}} e^{-\frac{R_{eq}}{L_{eq}}(d_3-d_2)T_{hs}} + \frac{V_{in}-V_{out}}{R_{eq}} e^{-\frac{R_{eq}}{L_{eq}} T_{hs}}}{1 + e^{-\frac{R_{eq}}{L_{eq}} T_{hs}}} \tag{5.35}$$

$$I_{t4} = \frac{\frac{V_{in}-V_{out}}{R_{eq}} - \frac{V_{in}}{R_{eq}} e^{-\frac{R_{eq}}{L_{eq}}(1-d_1)T_{hs}} + \frac{V_{out}}{R_{eq}} e^{-\frac{R_{eq}}{L_{eq}}(1-d_2)T_{hs}}}{1 + e^{-\frac{R_{eq}}{L_{eq}} T_{hs}}} + \\ + \frac{\frac{Vout}{R_{eq}} e^{-\frac{R_{eq}}{L_{eq}}(1-d_3)T_{hs}} - \frac{V_{out}}{R_{eq}} e^{-\frac{R_{eq}}{L_{eq}} T_{hs}}}{1 + e^{-\frac{R_{eq}}{L_{eq}} T_{hs}}} \tag{5.36}$$

The expressions (5.30), (5.31) and (5.33)-(5.36) constitute the average model of the considered DAB circuit. The model can be used for defining the inductor RMS current value by means of a piece-wise integration in the switching period, as follows.

$$I_{L,rms} = \sqrt{\frac{2}{T_S}\left(\int_0^{d_1 T_{hs}} i_a(t)^2 dt + \cdots \int_{d_3 T_{hs}}^{d_4 T_{hs}} i_d(t)^2 dt\right)} \tag{5.37}$$

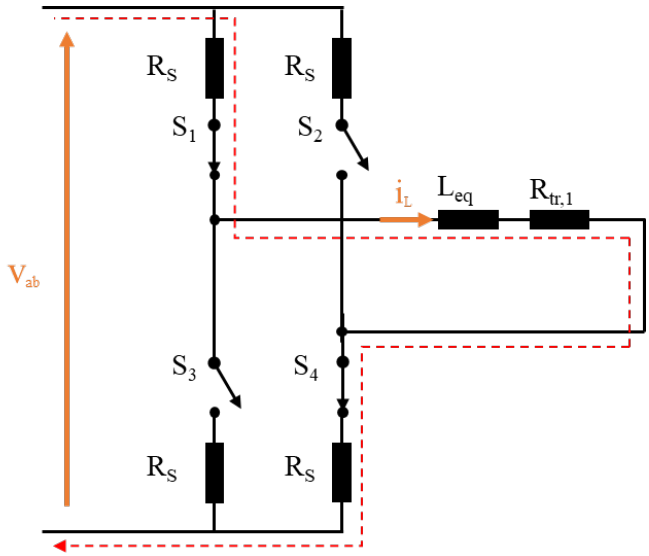

Figure 5.14: Ideal current path during a positive conduction phase of the input H-bridge.

5.1.6 DAB Loss Model

An approximated model of the DAB losses is developed to optimize the design process of the converter. The efficiency and performances of the system are estimated by taking into account voltage and current stresses of the components as well as the respective dissipated power.

5.1.7 Conduction losses

According to equation (5.38), conduction losses are computed by considering the current path occurring during conduction phases in the switching period. All the components involved in the path are taken into account. In detail, the transformer windings resistance R_{tr} and the ON-resistance $R_{DS,on}$ of the power switches are derived from the respective manufacturer datasheets.

$$P_{cond} = R_S \cdot I_{RMS}^2 \tag{5.38}$$

where R_S is the sum of all the modelled resistors in the conducting phase of a power switch and I_{RMS} is the RMS value of the circulating current.

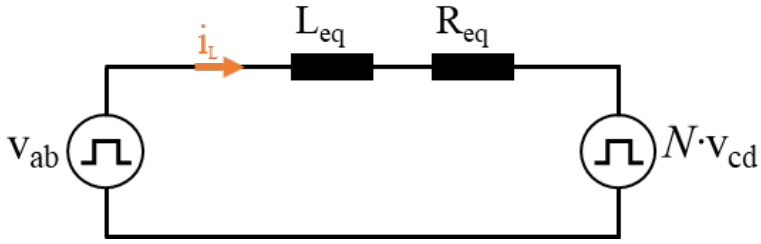

Figure 5.15: Ideal DAB model considering conduction losses.

Figure 5.14 shows the circuit involved in the conduction phase of the input H-bridge, highlighting the ideal current path occurring in the full bridge when a positive voltage $v_{ab} = V_{in}$ is imposed to the converter AC side. The two switches S_1 and S_4 are in ON state and their conducting resistances are considered in the current path. The circuit and the primary-side transformer winding resistors are included in $R_{tr,1}$. On the other hand, when a negative voltage $v_{ab} = -V_{in}$ is imposed the switches S_2 and S_3 are turned ON and the same resistance value occurs in the system.
The dual current path occurs in the output bridge when imposing positive and negative voltages $v_{cd} = V_{out}$ and $v_{cd} = -V_{out}$, respectively. As a result, the ideal DAB model considering conduction losses from both input and output bridges is obtained as shown in figure 5.15. The equivalent inductor L_{eq} includes the auxiliary and the transformer stray inductances. Similarly, the equivalent resistance R_{eq} comprises all the resistors involved in the current path, as follows.

$$L_{eq} = L + L_{tr,1} + N^2 L_{tr,2} \tag{5.39}$$

$$R_{eq} = 2 \cdot R_S + R_{tr,1} + N^2 \cdot (2 \cdot R_S + R_{tr,2}) \tag{5.40}$$

In the circuit shown in figure 5.15, the current i_L results according to equation (5.41).

$$i_L(t) = i_L(t_0) + \frac{1}{L_{eq}} \int_{t_0}^{t} (v_{ab} - N v_{cd} - R_{eq} i_L(t))\, dt \tag{5.41}$$

Depending on the implemented modulation technique, the switching period can be divided in a certain number of time intervals in which the voltages v_{ab} and v_{cd} are constant. Therefore, the solution to equation (5.41) is easily computed by piece-wise integration.

In detail, if $V_{ac,i} = v_{ab,i} - N v_{cd,i}$ is defined as constant during the i-th time interval, the solution of equation (5.41) results as follows.

$$i_L(t) = e^{-t/\tau} i_L(t_{i-1}) + \left(1 - e^{-t/\tau}\right) \frac{V_{ac,i}}{R_{eq}} \qquad t \in [t_{i-1}, t_i] \tag{5.42}$$

with $\tau = L_{eq}/R_{eq}$.
With the same approach, the RMS inductor current can be computed. Taking as an example the simple phase shift modulation, the RMS value of the current $i_L(t)$ shown in figure 5.4 results as follows.

$$I_{L,rms} = \sqrt{\frac{2}{T_S}\left(\int_0^{T_\phi} i_L(t)^2 dt + \int_{T_\phi}^{T_s/2} i_L(t)^2 dt\right)} \tag{5.43}$$

The inductor RMS current is finally derived by substituting the equation (5.42) in (5.43).

Similarly, the RMS value of the inductor current can be computed in the case of Triple Phase-Shift by increasing the number of constant-voltage time intervals in the switching period.

5.1.8 Switching Losses

Considering the high switching frequency of the converter, hard switching condition of the MOSFETs lead to excessive losses and they cannot be neglected in the dissipated power computation. The energy dissipated during turn-on (E_{on}) and turn-off (E_{off}) event can be determined from the manufacturer datasheet of the semiconductor switching devices.
However, thanks to the DAB operating principle, ZVS operation for the turn on phase of the switches is easy to achieve with advanced modulation techniques. When this condition occurs, the switch on losses are neglected and only the power dissipated during the turn off phase are considered.
The datasheet values are declared at nominal testing condition, considering the nominal voltage and current amplitudes V_{nom} and I_{nom}, respectively. According to equation (5.44), the dissipated energy is linearly converted to the actual operating conditions by considering the maximum voltage on the bridge V_{sw} and the peak current value I_{sw}.

$$E_{sw} = \frac{|I_{sw}| \cdot V_{sw}}{V_{nom} \cdot I_{nom}} \tag{5.44}$$

The switching losses in the input and output H-bridges are thus calculated according to equations (5.45) and (5.46), respectively.

$$P_{sw,in} = n_{sw} \cdot n_p \cdot f_s \cdot E_{ON} \frac{|I_{sw}| \cdot V_{in}}{V_{nom} I_{nom}} + 4 \cdot n_p \cdot f_s \cdot E_{OFF} \frac{|I_{sw}| \cdot V_{in}}{V_{nom} I_{nom}} \tag{5.45}$$

$$P_{sw,out} = n_{sw} \cdot n_p \cdot f_s \cdot E_{ON} \frac{|I_{sw}| \cdot V_{out}}{V_{nom} I_{nom}} + 4 \cdot n_p \cdot f_s \cdot E_{OFF} \frac{|I_{sw}| \cdot V_{out}}{V_{nom} I_{nom}} \tag{5.46}$$

where n_p is the number of parallel-connected switches and n_{sw} is the number of hard-switching devices in the bridge.
The losses are evaluated in various operating conditions of the converter, which also affect the value of n_{sw}.
The total switching losses are finally computed as follows.

$$P_{sw,tot} = P_{sw,in} + P_{sw,out} \tag{5.47}$$

5.2 Design of a Dual-Active-Bridge

A prototype of a Dual-Active-Bridge has been designed and its performances have been evaluated in simulation environment. Then, the results obtained from the design process have been used for the implementation of a prototype and an experimental analysis have been performed to validate the converter performances.
In this section, the application specifications are reported and the proposed design workflow is depicted. Numerical results and the experimental test performed on the developed prototype are reported as well.

5.2.1 Specifications

The application for the DAB converter design regards the interconnection of battery energy storage systems by means of a DC link. The basic project requirements for the DAB are listed in table 5.1.

Table 5.1: Key system specifications for the DAB converter design.

Parameter	Value
Input/Output Voltages	300 ÷ 500 V
Nominal power P_n	25 kW
Overall efficiency η_{ref}	$\geq$ 90 %
Switching frequency	100 kHz

5.2.2 Design Methodology

According to the numerical model developed for the DAB converter, a proper sizing tool has been carried out for designing and selecting its main parameters. This sizing tool is also integrated with iterative processes able to optimize both the efficiency and the performances of the converter.
A flowchart representation of the proposed design workflow is shown in figure 5.16. In the following, a detailed description of each design step is reported as well.

The *Initial Parameters Definition* consists in defining the initial components of the circuit based on the key specifications of the project (table 5.1). In detail, the transformer turns ratio N is identified to meet a similar voltage range on its primary and secondary side (equation (5.48)). Indeed, a voltage ratio m as close as possible to 1 is usually desired to extend the ZVS operating range.

$$m = \frac{V_{in}}{NV_{out}} \tag{5.48}$$

In the case of study, the input and output bridges have to be designed for the same voltage range and a transformer turns ratio $N = 1$ has been selected. Then, the maximum value admissible for the auxiliary inductance is calculated by considering the nominal power as the maximum achievable with the phase-shift modulation. Therefore, $P_{PSmax} = 25kW$ is substituted in equation (5.12) and L_{max} is obtained, as follows.

$$L_{max} = \frac{NV_{in}V_{out}}{8f_sP_{PSmax}} = 5.3\ \mu H \tag{5.49}$$

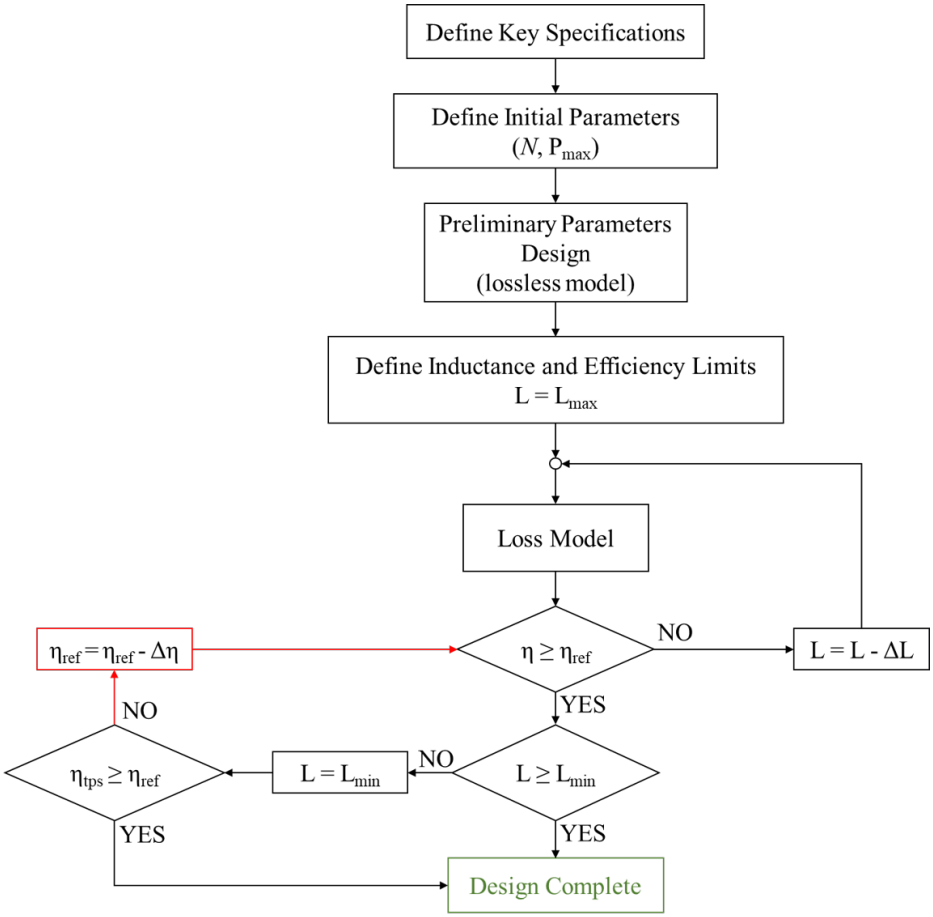

Figure 5.16: Flowchart of the proposed DAB design methodology.

The *Lossless Model* is then used to define a preliminary set of components, including the power switches. Considering the nominal power and the minimum voltage on the input bridge, the maximum expected current is computed, as follows.

$$I_{in,max} = \frac{P_n}{V_{in,min}} \tag{5.50}$$

The $I_{in,max}$ current value is taken into account to choose the power switches. Considering the power level and the high voltage on both the bridges of the converter, 1200 V SiC MOSFET are chosen and the possibility of multiple parallel-connected switches is taken into account for handling the rated current.

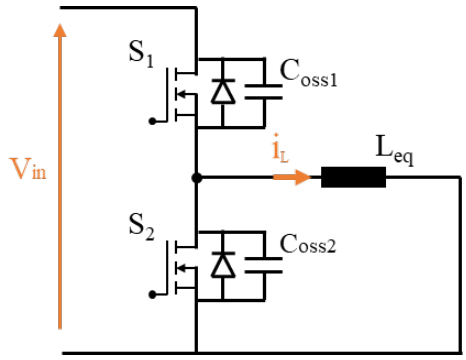

Figure 5.17: Circuit components involved in the soft switching process.

Once the power switches are chosen, the minimum auxiliary inductance for ensuring ZVS operation is computed. In detail, the output parasitic capacitance of the MOSFETs (C_{oss}) has to be considered in order to optimize the converter with zero-voltage switching [122].

As shown in figure 5.17, two power switches and the equivalent inductance L_{eq} are involved in the soft switching event. When a transition from the ON to the OFF state takes place in the static switch, the relative parasitic capacitance is charged from 0 V (short-circuited condition) up to the input voltage level V_{in}. Meanwhile, the complementary switch is commuted in the opposite way. The inductive component in the circuit has the role of imposing the necessary current to charge/discharge completely both the output capacitances of the MOSFETs before the second switch is turned on, allowing for the soft switch transition. This condition is met if the energy stored in the inductor, which depends on the inductance L_{eq} and the current amplitude I, equals at least the energy stored in the two capacitances, which depends on the C_{oss} value and the voltage level V_{in}, as follows.

$$\frac{1}{2}L_{eq}I_L^2 \geq \frac{1}{2}C_{eq}V_{in}^2 \tag{5.51}$$

where C_{eq} is the sum of all the C_{oss} involved in the commutation, and L_{eq} takes into account the transformer stray inductance and any auxiliary inductance.
Equation (5.51) is used to determine the minimum inductance value needed in the DAB, since the ZVS operation is a requirement in the project. In order to guarantee soft switching at least in nominal conditions, the maximum current at rated power and the maximum input voltage are considered, as follows.

$$L_{min} = \frac{C_{eq} V_{in,max}^2}{I_{in,max}^2} \tag{5.52}$$

At this point, the loss model can be considered to optimize and validate the circuit parameters. An iterating process is executed until the best conditions are met, by taking into account the following boundaries:

- nominal power, which has to be guaranteed in all the operating conditions of the converter;
- overall efficiency;
- minimum inductance value L_{min}, since it is decisive to enable zero-voltage switching.

Starting from the maximum value L_{max}, the circuit inductance is gradually decreased. As stated in section 5.1, the RMS inductor current is directly proportional to the equivalent inductance L_{eq}. Hence, the conduction losses are decreased and the converter efficiency η is increased by lowering L_{eq}.

The design process is completed when both the conditions $\eta \geq \eta_{ref}$ and $L \geq L_{min}$ are satisfied. In case this is not possible, the efficiency resulting from an advanced modulation scheme, such as the triple phase shift, is considered, otherwise the project specification regarding the overall efficiency has to be reconsidered.

Table 5.2 summarizes the results of the sizing tool, highlighting the main design parameters of the DAB converter. An optimal size for the auxiliary inductor has been selected taking into account for the nominal power, which defines the upper inductance limit, and the reactive energy needed for performing the ZVS operation of the DAB converter, which defines the lower inductance limit.

Table 5.2: Design parameters of the DAB converter.

Parameter	Value	Parameter	Value
Input/Output Voltages	300 ÷ 500 V	*Output capacitor*	0.33 mF
Nominal power	25 kW	*Output filter capacitor*	3.3 mF
Transformer ratio	1	*Output filter resistance*	3 mΩ
Switching frequency	100 kHz	*Output filter inductor*	2.35 μH
Auxiliary inductor	5.3 μH	*Input capacitor*	10 mF

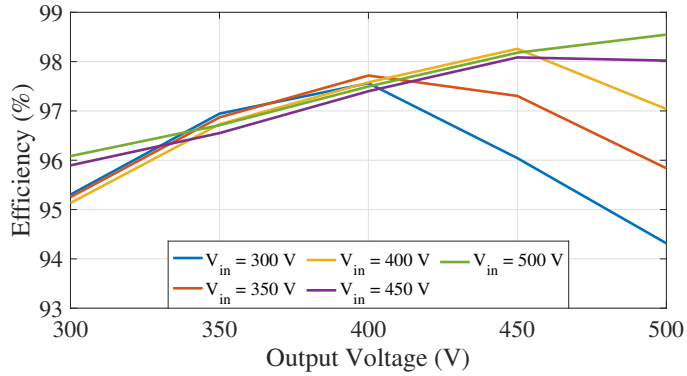

Figure 5.18: Variability of the designed DAB converter efficiency with respect to input and output voltage at nominal power ($P_t = 25\ kW$).

5.2.3 Numerical Analysis

A numerical analysis has been performed to validate the designed DAB converter. The converter model described in section 5.1.4 and the DAB loss model depicted in section 5.1.6 have been implemented in a simulation environment and the performances of the converter, in terms of power transfer and efficiency, have been evaluated under various operating conditions.
Figure 5.18 shows the variability of the converter efficiency with respect to the input and output voltage at nominal power transfer of 25 kW. As can be noticed, the developed DAB is characterized by an efficiency of 96% in the worst case, when the input voltage is the lowest admissible by the design ($V_{in} = 300\ V$). Moreover, the maximum efficiency of 98.6% resulted at nominal input and output voltage, fulfilling the technical requirements reported in section 5.2.1.

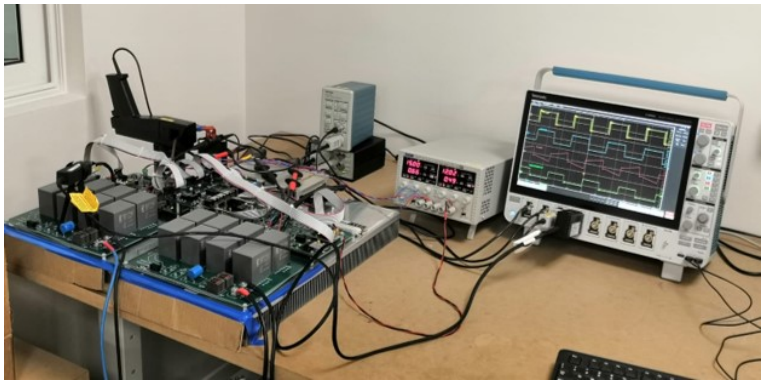

Figure 5.19: Experimental setup of 25-kW SiC-based DAB converter.

5.2.4 Experimental Validation

An experimental setup has been carried out with the aim of validating the numerical results and the performances of the DAB converter due to the adoption of different modulation techniques. According to the design parameters achieved from the sizing tool, a prototype of a 25-kW SiC-based DAB converter has been developed and implemented. Figure 5.19 shows the experimental setup including the prototype of 25-kW SiC-based DAB converter designed and implemented. The prototype has been connected to a bidirectional power supply used as voltage source for the input bridge, while a resistive load has been connected at the output bridge. The efficiency of the converter has been evaluated by means of a Yokogawa WT3000 Precision Power Analyzer, while isolated current probes and Tektronix IsoVu probes were adopted for current and voltage monitoring, respectively.

The preliminary experimental results obtained in case of phase-shift modulation at 9 kW of power transfer are depicted in figure 5.20. They show a correct functionality of the DAB prototype when operated at 350 V and 300 V for the input and output bridge voltage, respectively.

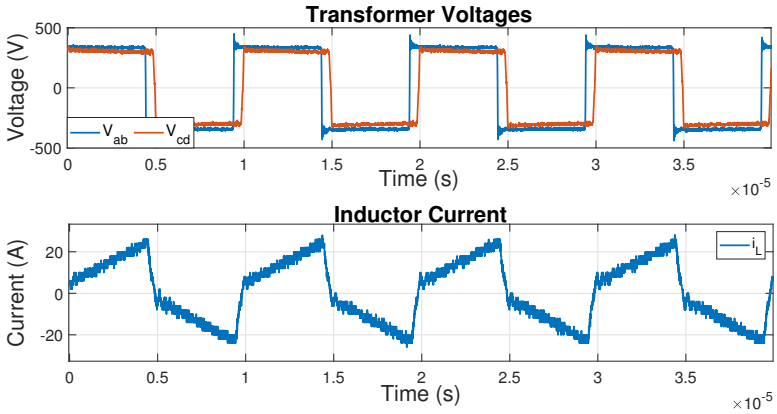

Figure 5.20: Preliminary experimental results obtained with the prototyped DAB converter at $P = 9\ kW$, $V_{in} = 350\ V$ and $V_{out} = 300\ V$ considering a single phase-shift modulation.

Further experimental tests were performed to characterize the converter efficiency, as shown in table 5.3. Three different operating points have been experimentally validated and the measured efficiency resulted in the nearest of 96% for all the tested operating conditions.

Table 5.3: Experimental results obtained with a 25-kW SiC-based DAB converter.

	Test 1	**Test 2**	**Test 3**
Input DC Voltage (V)	300	300	300
Output DC Voltage (V)	300	300	350
Resistive Load (Ω)	40	30	30
Input Power (W)	2424.3	3112.5	4173.9
Output Power (W)	2320.1	2993.0	4013.8
Overall Efficiency (%)	95.70	96.16	96.16
Overall Losses (W)	104.2	119.5	160.1

These results are in line with the ones obtained in the numerical analysis. Indeed, the differences between the efficiencies experimentally measured and the ones obtained with the numerical model are -0.21%, -0.5% and 0.15% for the first, second and third test case, respectively. This fully confirms the numerical analysis and the goodness of the experimental results obtained with the implemented prototype.

Conclusions

In the presented work, design methodologies for BESSs and HESSs have been discussed considering automotive and stationary applications. An extensive research activity has been focused on model-based state estimators for the accurate knowledge of SoC in different energy storage technologies, such as Lithium-Ion batteries and Dual Layer Supercapacitors. In particular, different variants of Kalman filtering algorithms have been investigated and their performances have been evaluated under various operating conditions. Moreover, an Adaptive Square-Root Unscented Kalman Filter (ASR-UKF) has been proposed, which allows for correctly estimating the SoC while overcoming the typical initialization issue of Kalman filters. A methodology to extend the estimation task for assessing multiple SoC information in battery packs has been proposed as well.

Equivalent circuit models have been developed and experimentally characterized for representing the behavior of Lithium-Ion battery cells and supercapacitor modules. Their integration with the proposed ASR-UKF and their impact on the system performances have been evaluated by means of numerical analyses in terms of estimation accuracy and robustness to parametric variations. Then, the obtained results have been experimentally validated. In particular, two different Lithium cells have been adopted to perform charging/discharging cycles with the aim of validating the performance of real-time SoC estimation. The multiple estimation capability of the developed ASR-UKF has been analysed by emulating a 48 V battery pack in a Hardware-In-the-Loop testing environment. Moreover, a 48 V supercapacitor module has been adopted with the aim of experimentally validating the SoC estimation algorithm under realistic grid power profiles.

Both numerical and experimental results confirm the validity of the developed algorithms and their feasibility for real-time implementation in real-world applications.

The power conversion stage in Hybrid Energy Storage Systems has

been included in the research activity and different DC-DC converter topologies have been investigated. According to specific application requirements, a design methodology for Dual-Active-Bridge (DAB) converters has been developed to optimize both the efficiency and the performances of the converter. Moreover, a detailed dynamic model for extensive numerical analysis has been developed, while a loss model has been adopted with the aim of evaluating the efficiency of the designed DAB converter. Numerical analyses have been performed to investigate the impact of different modulation techniques in terms of power transfer capability, efficiency and dynamic performances of the DAB. Then, the developed DC-DC converter has been prototyped with the aim of experimentally validating the design methodology and the considered modulation techniques.
Both numerical and experimental results validate the designed prototype and the goodness of the proposed methodology.
In conclusion, this dissertation provides an overall knowledge that enables an effective approach in defining the main aspects related to the implementation of BESSs and HESSs. This includes the development of an accurate model-based SoC estimation algorithm, the selection of appropriate storage technologies and interconnection architectures as well as the design and implementation of the DC-DC converter.
Future improvements and developments will regard the implementation of the proposed estimation methodology in different real-world applications, such as high voltage battery packs and complex hybrid storage systems for Electric Vehicles as well as for grid ancillary services. This will allow to evaluate the impact of the accurate SoC knowledge on advanced power allocation control algorithms. On the other hand, additional DC-DC converter topologies can be investigated for extending the analysis presented in this dissertation. Furthermore, the performance optimization by means of advanced control strategies for an online selection of the optimal modulation technique can be investigated and the experimental analysis can be extended in different operating conditions.

List of Figures

List of Tables

Bibliography

[1] M. Y. Suberu, M. W. Mustafa, and N. Bashir, "Energy storage systems for renewable energy power sector integration and mitigation of intermittency," *Renewable and Sustainable Energy Reviews*, vol. 35, pp. 499–514, 2014.

[2] M. R. Chakraborty, S. Dawn, P. K. Saha, J. B. Basu, and T. S. Ustun, "A comparative review on energy storage systems and their application in deregulated systems," *Batteries*, vol. 8, no. 9, 2022. [Online]. Available: https://www.mdpi.com/2313-0105/8/9/124

[3] J. I. LEON, E. Dominguez, L. Wu, A. Marquez Alcaide, M. Reyes, and J. Liu, "Hybrid energy storage systems: Concepts, advantages, and applications," *IEEE Industrial Electronics Magazine*, vol. 15, no. 1, pp. 74–88, 2021.

[4] A. Eftekhari, Ed., *Future Lithium-ion Batteries*. The Royal Society of Chemistry, 2019. [Online]. Available: http://dx.doi.org/10.1039/9781788016124

[5] K. A. Smith, "Electrochemical control of lithium-ion batteries [applications of control]," *IEEE Control Systems Magazine*, vol. 30, no. 2, pp. 18–25, 2010.

[6] M. Dubarry and G. Baure, "Perspective on commercial li-ion battery testing, best practices for simple and effective protocols," *Electronics*, vol. 9, no. 1, 2020. [Online]. Available: https://www.mdpi.com/2079-9292/9/1/152

[7] H. P. Zhao W., Yi J. and Z. H., "Solid-state electrolytes for lithium-ion batteries: Fundamentals, challenges and perspectives," *Electrochemical Energy Reviews*, pp. 574–605, 2019.

[8] B. Bilgin, P. Magne, P. Malysz, Y. Yang, V. Pantelic, M. Preindl, A. Korobkine, W. Jiang, M. Lawford, and A. Emadi, "Making the case for electrified transportation," *IEEE Transactions on Transportation Electrification*, vol. 1, no. 1, pp. 4–17, 2015.

[9] B. K. Saikia, S. M. Benoy, M. Bora, J. Tamuly, M. Pandey, and D. Bhattacharya, "A brief review on supercapacitor energy storage devices and utilization of natural carbon resources as their electrode materials," *Fuel*, vol. 282, p. 118796, 2020. [Online]. Available: https://www.sciencedirect.com/science/article/pii/S0016236120317920

[10] W. Raza, F. Ali, N. Raza, Y. Luo, K.-H. Kim, J. Yang, S. Kumar, A. Mehmood, and E. E. Kwon, "Recent advancements in supercapacitor technology," *Nano Energy*, vol. 52, pp. 441–473, 2018. [Online]. Available: https://www.sciencedirect.com/science/article/pii/S2211285518305755

[11] M. Bahloul and S. K. Khadem, "Impact of power sharing method on battery life extension in hess for grid ancillary services," *IEEE Transactions on Energy Conversion*, vol. 34, no. 3, pp. 1317–1327, 2019.

[12] J. W. Shim, G. Verbič, N. Zhang, and K. Hur, "Harmonious integration of faster-acting energy storage systems into frequency control reserves in power grid with high renewable generation," *IEEE Transactions on Power Systems*, vol. 33, no. 6, pp. 6193–6205, 2018.

[13] B. Yang, J. Wang, X. Zhang, J. Wang, H. Shu, S. Li, T. He, C. Lan, and T. Yu, "Applications of battery/supercapacitor hybrid energy storage systems for electric vehicles using perturbation observer based robust control," *Journal of Power Sources*, vol. 448, p. 227444, 2020. [Online]. Available: https://www.sciencedirect.com/science/article/pii/S0378775319314375

[14] L. Zhang, X. Ye, X. Xia, and F. Barzegar, "A real-time energy management and speed controller for an electric vehicle powered by a hybrid energy storage system," *IEEE Transactions on Industrial Informatics*, vol. 16, no. 10, pp. 6272–6280, 2020.

[15] J. W. Shim, G. Verbič, H. Kim, and K. Hur, "On droop control of energy-constrained battery energy storage systems for grid

frequency regulation," *IEEE Access*, vol. 7, pp. 166 353–166 364, 2019.

[16] N. M. L. Tan, T. Abe, and H. Akagi, "Design and performance of a bidirectional isolated dc-dc converter for a battery energy storage system," *IEEE Transactions on Power Electronics*, vol. 27, no. 3, pp. 1237–1248, 2012.

[17] S. Vazquez, S. M. Lukic, E. Galvan, L. G. Franquelo, and J. M. Carrasco, "Energy storage systems for transport and grid applications," *IEEE Transactions on Industrial Electronics*, vol. 57, no. 12, pp. 3881–3895, 2010.

[18] S.-A. Amamra and J. Marco, "Vehicle-to-grid aggregator to support power grid and reduce electric vehicle charging cost," *IEEE Access*, vol. 7, pp. 178 528–178 538, 2019.

[19] B. K. Bose, "Global energy scenario and impact of power electronics in 21st century," *IEEE Transactions on Industrial Electronics*, vol. 60, no. 7, pp. 2638–2651, 2013.

[20] C. Liu, K. T. Chau, D. Wu, and S. Gao, "Opportunities and challenges of vehicle-to-home, vehicle-to-vehicle, and vehicle-to-grid technologies," *Proceedings of the IEEE*, vol. 101, no. 11, pp. 2409–2427, 2013.

[21] M. A. Masrur, A. G. Skowronska, J. Hancock, S. W. Kolhoff, D. Z. McGrew, J. C. Vandiver, and J. Gatherer, "Military-based vehicle-to-grid and vehicle-to-vehicle microgrid-system architecture and implementation," *IEEE Transactions on Transportation Electrification*, vol. 4, no. 1, pp. 157–171, 2018.

[22] M. Bragard, N. Soltau, S. Thomas, and R. W. De Doncker, "The balance of renewable sources and user demands in grids: Power electronics for modular battery energy storage systems," *IEEE Transactions on Power Electronics*, vol. 25, no. 12, pp. 3049–3056, 2010.

[23] G. Wang, G. Konstantinou, C. D. Townsend, J. Pou, S. Vazquez, G. D. Demetriades, and V. G. Agelidis, "A review of power electronics for grid connection of utility-scale battery energy storage systems," *IEEE Transactions on Sustainable Energy*, vol. 7, no. 4, pp. 1778–1790, 2016.

[24] S.-J. Jang, T.-W. Lee, W.-C. Lee, and C.-Y. Won, "Bi-directional dc-dc converter for fuel cell generation system," in *2004 IEEE 35th Annual Power Electronics Specialists Conference (IEEE Cat. No.04CH37551)*, vol. 6, 2004, pp. 4722–4728 Vol.6.

[25] J. Barton and D. Infield, "Energy storage and its use with intermittent renewable energy," *IEEE Transactions on Energy Conversion*, vol. 19, no. 2, pp. 441–448, 2004.

[26] T. S. Babu, K. R. Vasudevan, V. K. Ramachandaramurthy, S. B. Sani, S. Chemud, and R. M. Lajim, "A comprehensive review of hybrid energy storage systems: Converter topologies, control strategies and future prospects," *IEEE Access*, vol. 8, pp. 148 702–148 721, 2020.

[27] M. Glavin, P. K. Chan, S. Armstrong, and W. Hurley, "A standalone photovoltaic supercapacitor battery hybrid energy storage system," in *2008 13th International Power Electronics and Motion Control Conference*, 2008, pp. 1688–1695.

[28] Z. Song, H. Hofmann, J. Li, X. Han, X. Zhang, and M. Ouyang, "A comparison study of different semi-active hybrid energy storage system topologies for electric vehicles," *Journal of Power Sources*, vol. 274, pp. 400–411, 2015.

[29] J. Cao and A. Emadi, "A new battery/ultracapacitor hybrid energy storage system for electric, hybrid, and plug-in hybrid electric vehicles," *IEEE Transactions on Power Electronics*, vol. 27, no. 1, pp. 122–132, 2012.

[30] U. Manandhar, N. R. Tummuru, S. K. Kollimalla, A. Ukil, G. H. Beng, and K. Chaudhari, "Validation of faster joint control strategy for battery- and supercapacitor-based energy storage system," *IEEE Transactions on Industrial Electronics*, vol. 65, no. 4, pp. 3286–3295, 2018.

[31] S. K. Kollimalla, M. K. Mishra, A. Ukil, and H. B. Gooi, "Dc grid voltage regulation using new hess control strategy," *IEEE Transactions on Sustainable Energy*, vol. 8, no. 2, pp. 772–781, 2017.

[32] I. J. Cohen, D. A. Wetz, J. M. Heinzel, and Q. Dong, "Design and characterization of an actively controlled hybrid energy storage module for high-rate directed energy applications," *IEEE Transactions on Plasma Science*, vol. 43, no. 5, pp. 1427–1433, 2015.

[33] F. Pellitteri, R. Miceli, G. Schettino, F. Viola, and L. Schirone, "Design and realization of a bidirectional full bridge converter with improved modulation strategies," *Electronics*, vol. 9, no. 5, 2020. [Online]. Available: https://www.mdpi.com/2079-9292/9/5/724

[34] L. Zhu, "A novel soft-commutating isolated boost full-bridge zvs-pwm dc-dc converter for bidirectional high power applications," *IEEE Transactions on Power Electronics*, vol. 21, no. 2, pp. 422–429, 2006.

[35] I. Shigenori and A. Hirofumi, "A bidirectional isolated dc-dc converter as a core circuit of the next-generation medium-voltage power conversion system," *IEEE Transactions on Power Electronics*, vol. 22, no. 2, pp. 535–542, 2007.

[36] N. M. L. Tan, T. Abe, and H. Akagi, "Design and performance of a bidirectional isolated dc-dc converter for a battery energy storage system," *IEEE Transactions on Power Electronics*, vol. 27, no. 3, pp. 1237–1248, 2012.

[37] B. Zhao, Q. Song, and W. Liu, "Efficiency characterization and optimization of isolated bidirectional dc-dc converter based on dual-phase-shift control for dc distribution application," *IEEE Transactions on Power Electronics*, vol. 28, no. 4, pp. 1711–1727, 2013.

[38] L. Xue, Z. Shen, D. Boroyevich, P. Mattavelli, and D. Diaz, "Dual active bridge-based battery charger for plug-in hybrid electric vehicle with charging current containing low frequency ripple," *IEEE Transactions on Power Electronics*, vol. 30, no. 12, pp. 7299–7307, 2015.

[39] S. Inoue and H. Akagi, "A bidirectional dc-dc converter for an energy storage system with galvanic isolation," *IEEE Transactions on Power Electronics*, vol. 22, no. 6, pp. 2299–2306, 2007.

[40] J. Huang, Y. Wang, Z. Li, and W. Lei, "Unified triple-phase-shift control to minimize current stress and achieve full soft-switching of isolated bidirectional dc-dc converter," *IEEE Transactions on Industrial Electronics*, vol. 63, no. 7, pp. 4169–4179, 2016.

[41] S. Shao, H. Chen, X. Wu, J. Zhang, and K. Sheng, "Circulating current and zvs-on of a dual active bridge dc-dc converter: A review," *IEEE Access*, vol. 7, pp. 50 561–50 572, 2019.

[42] Q. Bu, H. Wen, J. Wen, Y. Hu, and Y. Du, "Transient dc bias elimination of dual-active-bridge dc-dc converter with improved triple-phase-shift control," *IEEE Transactions on Industrial Electronics*, vol. 67, no. 10, pp. 8587–8598, 2020.

[43] B. Zhao, Q. Song, and W. Liu, "Efficiency characterization and optimization of isolated bidirectional dc-dc converter based on dual-phase-shift control for dc distribution application," *IEEE Transactions on Power Electronics*, vol. 28, no. 4, pp. 1711–1727, 2013.

[44] N. Hou and Y. W. Li, "Overview and comparison of modulation and control strategies for a nonresonant single-phase dual-active-bridge dc-dc converter," *IEEE Transactions on Power Electronics*, vol. 35, no. 3, pp. 3148–3172, 2020.

[45] Y.-C. Jeung and D.-C. Lee, "Voltage and current regulations of bidirectional isolated dual-active-bridge dc-dc converters based on a double-integral sliding mode control," *IEEE Transactions on Power Electronics*, vol. 34, no. 7, pp. 6937–6946, 2019.

[46] F. Lin, X. Zhang, X. Li, C. Sun, W. Cai, and Z. Zhang, "Automatic triple phase-shift modulation for dab converter with minimized power loss," *IEEE Transactions on Industry Applications*, vol. 58, no. 3, pp. 3840–3851, 2022.

[47] S. Dutta, S. Hazra, and S. Bhattacharya, "A digital predictive current-mode controller for a single-phase high-frequency transformer-isolated dual-active bridge dc-to-dc converter," *IEEE Transactions on Industrial Electronics*, vol. 63, no. 9, pp. 5943–5952, 2016.

[48] Q. Xiao, L. Chen, H. Jia, P. W. Wheeler, and T. Dragičević, "Model predictive control for dual active bridge in naval dc microgrids supplying pulsed power loads featuring fast transition

and online transformer current minimization," *IEEE Transactions on Industrial Electronics*, vol. 67, no. 6, pp. 5197–5203, 2020.

[49] S. M. Akbar, A. Hasan, A. J. Watson, and P. Wheeler, "Model predictive control with triple phase shift modulation for a dual active bridge dc-dc converter," *IEEE Access*, vol. 9, pp. 98 603–98 614, 2021.

[50] R. L. Steigerwald, "High-frequency resonant transistor dc-dc converters," *IEEE Transactions on Industrial Electronics*, vol. IE-31, no. 2, pp. 181–191, 1984.

[51] M. Yaqoob, K. H. Loo, and Y. M. Lai, "A four-degrees-of-freedom modulation strategy for dual-active-bridge series-resonant converter designed for total loss minimization," *IEEE Transactions on Power Electronics*, vol. 34, no. 2, pp. 1065–1081, 2019.

[52] R. Steigerwald, "A comparison of half-bridge resonant converter topologies," *IEEE Transactions on Power Electronics*, vol. 3, no. 2, pp. 174–182, 1988.

[53] J. Lazar and R. Martinelli, "Steady-state analysis of the llc series resonant converter," in *APEC 2001. Sixteenth Annual IEEE Applied Power Electronics Conference and Exposition (Cat. No.01CH37181)*, vol. 2, 2001, pp. 728–735 vol.2.

[54] S. De Simone, C. Adragna, C. Spini, and G. Gattavari, "Design-oriented steady-state analysis of llc resonant converters based on fha," in *International Symposium on Power Electronics, Electrical Drives, Automation and Motion, 2006. SPEEDAM 2006.*, 2006, pp. 200–207.

[55] G. Pledl, M. Tauer, and D. Buecherl, "Theory of operation, design procedure and simulation of a bidirectional llc resonant converter for vehicular applications," in *2010 IEEE Vehicle Power and Propulsion Conference*, 2010, pp. 1–5.

[56] D. Xie, L. Wang, Z. Zhang, S. Wang, L. Kang, and J. Yao, "Photovoltaic energy storage system based on bidirectional llc resonant converter control technology," *Energies*, vol. 15, no. 17, 2022. [Online]. Available: https://www.mdpi.com/1996-1073/15/17/6436

[57] X. Wang, C. Jiang, B. Lei, H. Teng, H. K. Bai, and J. L. Kirtley, "Power-loss analysis and efficiency maximization of a silicon-carbide mosfet-based three-phase 10-kw bidirectional ev charger using variable-dc-bus control," *IEEE Journal of Emerging and Selected Topics in Power Electronics*, vol. 4, no. 3, pp. 880–892, 2016.

[58] L. Shi, B. Liu, and S. Duan, "Burst-mode and phase-shift hybrid control method of llc converters for wide output range applications," *IEEE Transactions on Industrial Electronics*, vol. 67, no. 2, pp. 1013–1023, 2020.

[59] J. Lu, Y. Wang, X. Li, and C. Du, "High-conversion-ratio isolated bidirectional dc-dc converter for distributed energy storage systems," *IEEE Transactions on Power Electronics*, vol. 34, no. 8, pp. 7256–7277, 2019.

[60] J.-H. Jung, H.-S. Kim, M.-H. Ryu, and J.-W. Baek, "Design methodology of bidirectional cllc resonant converter for high-frequency isolation of dc distribution systems," *IEEE Transactions on Power Electronics*, vol. 28, no. 4, pp. 1741–1755, 2013.

[61] J. Huang, X. Zhang, Z. Shuai, X. Zhang, P. Wang, L. H. Koh, J. Xiao, and X. Tong, "Robust circuit parameters design for the cllc-type dc transformer in the hybrid ac-dc microgrid," *IEEE Transactions on Industrial Electronics*, vol. 66, no. 3, pp. 1906–1918, 2019.

[62] J. Min and M. Ordonez, "Bidirectional resonant cllc charger for wide battery voltage range: Asymmetric parameters methodology," *IEEE Transactions on Power Electronics*, vol. 36, no. 6, pp. 6662–6673, 2021.

[63] H. Rahimi-Eichi, U. Ojha, F. Baronti, and M.-Y. Chow, "Battery management system: An overview of its application in the smart grid and electric vehicles," *IEEE Industrial Electronics Magazine*, vol. 7, no. 2, pp. 4–16, 2013.

[64] C. Zhang, K. Li, L. Pei, and C. Zhu, "An integrated approach for real-time model-based state-of-charge estimation of lithium-ion batteries," *Journal of Power Sources*, vol. 283, pp. 24–36, 2015.

[65] G. Fan, X. Li, and M. Canova, "A reduced-order electrochemical model of li-ion batteries for control and estimation applications," *IEEE Transactions on Vehicular Technology*, vol. 67, no. 1, pp. 76–91, 2018.

[66] M. Li, "Li-ion dynamics and state of charge estimation," *Renewable Energy*, vol. 100, 06 2016.

[67] J. Gomez, R. Nelson, E. E. Kalu, M. H. Weatherspoon, and J. P. Zheng, "Equivalent circuit model parameters of a high-power li-ion battery: Thermal and state of charge effects," *Journal of Power Sources*, vol. 196, no. 10, pp. 4826–4831, 2011. [Online]. Available: https://www.sciencedirect.com/science/article/pii/S0378775311000899

[68] R. E. Kalman, "A New Approach to Linear Filtering and Prediction Problems," *Journal of Basic Engineering*, vol. 82, no. 1, pp. 35–45, 03 1960. [Online]. Available: https://doi.org/10.1115/1.3662552

[69] M. Hannan, M. Lipu, A. Hussain, and A. Mohamed, "A review of lithium-ion battery state of charge estimation and management system in electric vehicle applications: Challenges and recommendations," *Renewable and Sustainable Energy Reviews*, vol. 78, pp. 834–854, 2017. [Online]. Available: https://www.sciencedirect.com/science/article/pii/S1364032117306275

[70] G. L. Plett, "Kalman-filter soc estimation for LiPB HEV cells," in *CD-ROM Proceedings of the 19th Electric Vehicle Symposium (EVS19), Busan Korea*, 2002.

[71] E. A. Wan and R. Van Der Merwe, "The unscented kalman filter for nonlinear estimation," in *Proceedings of the IEEE 2000 Adaptive Systems for Signal Processing, Communications, and Control Symposium (Cat. No.00EX373)*, 2000, pp. 153–158.

[72] R. Van der Merwe and E. A. Wan, "The square-root unscented kalman filter for state and parameter-estimation," in *2001 IEEE International Conference on Acoustics, Speech, and Signal Processing. Proceedings (Cat. No.01CH37221)*, vol. 6, 2001, pp. 3461–3464 vol.6.

[73] W. H. Press, S. A. Teukolsky, W. T. Vetterling, and B. P. Flannery, "Numerical recipes in c: The art of scientific computing," *Cambridge University Press, 2nd edition*, 1992.

[74] H. Aung, K. Soon Low, and S. Ting Goh, "State-of-charge estimation of lithium-ion battery using square root spherical unscented kalman filter (sqrt-ukfst) in nanosatellite," *IEEE Transactions on Power Electronics*, vol. 30, no. 9, pp. 4774–4783, 2015.

[75] Mathworks, "Nonlinear state estimation of a degrading battery system." [Online]. Available: https://it.mathworks.com/help/predmaint/ug/nonlinear-state-estimation-of-a-degrading-battery-system.html

[76] M. Partovibakhsh and G. Liu, "An adaptive unscented kalman filtering approach for online estimation of model parameters and state-of-charge of lithium-ion batteries for autonomous mobile robots," *IEEE Transactions on Control Systems Technology*, vol. 23, no. 1, pp. 357–363, 2015.

[77] D. Fusco, M. Di Monaco, F. Porpora, and G. Tomasso, "A novel adaptive square-root unscented kalman filter for battery soc estimation," in *PCIM Europe digital days 2021; International Exhibition and Conference for Power Electronics, Intelligent Motion, Renewable Energy and Energy Management*, 2021, pp. 1–8.

[78] S. Liu, N. Cui, and C. Zhang, "An adaptive square root unscented kalman filter approach for state of charge estimation of lithium-ion batteries," *Energies*, p. 10, 2017.

[79] Y. Zhou, C. Zhang, Y. Zhang, and J. Zhang, "A new adaptive square-root unscented kalman filter for nonlinear systems with additive noise," *International Journal of Aerospace Engineering*, p. 9, 2015.

[80] J. Meng, G. Luo, and F. Gao, "Lithium polymer battery state-of-charge estimation based on adaptive unscented kalman filter and support vector machine," *IEEE Transactions on Power Electronics*, vol. 31, no. 3, pp. 2226–2238, 2016.

[81] S. Mousavi G. and M. Nikdel, "Various battery models for various simulation studies and applications," *Renewable and Sustainable Energy Reviews*, vol. 32, pp. 477–485, 2014. [Online].

Available: https://www.sciencedirect.com/science/article/pii/S1364032114000598

[82] C. Zhang, K. Li, S. McLoone, and Z. Yang, "Battery modelling methods for electric vehicles - a review," jun 2014, paper FrB10.5; 13th European Control Conference (ECC'2014) ; Conference date: 24-06-2014 Through 27-06-2014.

[83] G. Fan, K. Pan, M. Canova, J. Marcicki, and X. Yang, "Modeling of li-ion cells for fast simulation of high c-rate and low temperature operations," *Journal of The Electrochemical Society*, vol. 163, pp. A666–A676, 02 2016.

[84] Q. Zhang, Y. Li, Y. Shang, B. Duan, N. Cui, and C. Zhang, "A fractional-order kinetic battery model of lithium-ion batteries considering a nonlinear capacity," *Electronics*, vol. 8, no. 4, 2019. [Online]. Available: https://www.mdpi.com/2079-9292/8/4/394

[85] L. Tao, J. Ma, Y. Cheng, A. Noktehdan, J. Chong, and C. Lu, "A review of stochastic battery models and health management," *Renewable and Sustainable Energy Reviews*, vol. 80, pp. 716–732, 2017. [Online]. Available: https://www.sciencedirect.com/science/article/pii/S1364032117307736

[86] D. Yang, Y. Wang, R. Pan, R. Chen, and Z. Chen, "A neural network based state-of-health estimation of lithium-ion battery in electric vehicles," *Energy Procedia*, vol. 105, pp. 2059–2064, 2017.

[87] D. Jiani, L. Zhitao, W. Youyi, and W. Changyun, "A fuzzy logic-based model for li-ion battery with soc and temperature effect," in *11th IEEE International Conference on Control & Automation*, 2014, pp. 1333–1338.

[88] W. Junping, C. Quanshi, and C. Binggang, "Support vector machine based battery model for electric vehicles," *Energy Conversion and Management*, vol. 47, pp. 858–864, 2006.

[89] J. P. Christophersen, "Battery test manual for electric vehicles, revision 3," 6 2015. [Online]. Available: https://www.osti.gov/biblio/1186745

[90] M. A. Roscher, O. S. Bohlen, and D. U. Sauer, "Reliable state estimation of multicell lithium-ion battery systems," *IEEE Transactions on Energy Conversion*, vol. 26, no. 3, pp. 737–743, 2011.

[91] Y. Zheng, W. Gao, M. Ouyang, L. Lu, L. Zhou, and X. Han, "State-of-charge inconsistency estimation of lithium-ion battery pack using mean-difference model and extended kalman filter," *Journal of Power Sources*, vol. 383, pp. 50–58, 2018. [Online]. Available: https://www.sciencedirect.com/science/article/pii/S0378775318301794

[92] G. De Carne, A. Morandi, and S. Karrari, "Supercapacitor modeling for real-time simulation applications," *IEEE Journal of Emerging and Selected Topics in Industrial Electronics*, vol. 3, no. 3, pp. 509–518, 2022.

[93] L. Zubieta and R. Bonert, "Characterization of double-layer capacitors for power electronics applications," *IEEE Transactions on Industry Applications*, vol. 36, no. 1, pp. 199–205, 2000.

[94] F. Rafik, H. Gualous, R. Gallay, A. Crausaz, and A. Berthon, "Frequency, thermal and voltage supercapacitor characterization and modeling," *Journal of Power Sources*, vol. 165, no. 2, pp. 928–934, 2007, iBA - HBC 2006. [Online]. Available: https://www.sciencedirect.com/science/article/pii/S0378775306025110

[95] P. KURZWEIL, M. CHWISTEK, and R. Gallay, "Electrochemical and spectroscopic studies on rated capacitance and aging mechanisms of supercapacitors," 01 2006.

[96] R. Spyker and R. Nelms, "Classical equivalent circuit parameters for a double-layer capacitor," *IEEE Transactions on Aerospace and Electronic Systems*, vol. 36, no. 3, pp. 829–836, 2000.

[97] A. Berrueta, A. UrsÃºa, I. S. MartÃn, A. Eftekhari, and P. Sanchis, "Supercapacitors: Electrical characteristics, modeling, applications, and future trends," *IEEE Access*, vol. 7, pp. 50 869–50 896, 2019.

[98] N. Devillers, S. Jemei, M.-C. PÃ©ra, D. BienaimÃ©, and F. Gustin, "Review of characterization methods for supercapacitor modelling," *Journal of Power Sources*, vol.

246, pp. 596–608, 2014. [Online]. Available: https://www.sciencedirect.com/science/article/pii/S0378775313013256

[99] V. Musolino, L. Piegari, and E. Tironi, "New full-frequency-range supercapacitor model with easy identification procedure," *IEEE Transactions on Industrial Electronics*, vol. 60, no. 1, pp. 112–120, 2013.

[100] A. Morandi, A. Lampasi, A. Cocchi, F. Gherdovich, U. Melaccio, P. L. Ribani, C. Rossi, and F. Soavi, "Characterization and model parameters of large commercial supercapacitor cells," *IEEE Access*, vol. 9, pp. 20 376–20 390, 2021.

[101] P. Saha, S. Dey, and M. Khanra, "Modeling and state-of-charge estimation of supercapacitor considering leakage effect," *IEEE Transactions on Industrial Electronics*, vol. 67, no. 1, pp. 350–357, 2020.

[102] X. Huang, Y. Li, A. Acharya, X. Sui, J. Meng, R. Teodorescu, and D.-I. Stroe, "A review of pulsed current technique for lithium-ion batteries," *Energies*, vol. 13, p. 2458, 05 2020.

[103] V. M. Fico, C. P. Arribas, Ã. R. Soaje, M. A. Martin Prats, S. R. Utrera, A. L. Rodriguez Vazquez, and L. M. Parrilla Casquet, "Implementing the unscented kalman filter on an embedded system: A lesson learnt," in *2015 IEEE International Conference on Industrial Technology (ICIT)*, 2015, pp. 2010–2014.

[104] R. Xiong, F. Sun, X. Gong, and H. He, "Adaptive state of charge estimator for lithium-ion cells series battery pack in electric vehicles," *Journal of Power Sources*, vol. 242, pp. 699–713, 2013. [Online]. Available: https://www.sciencedirect.com/science/article/pii/S0378775313008616

[105] X. Zhang, Y. Wang, C. Liu, and Z. Chen, "A novel approach of remaining discharge energy prediction for large format lithium-ion battery pack," *Journal of Power Sources*, vol. 343, pp. 216–225, 2017. [Online]. Available: https://www.sciencedirect.com/science/article/pii/S037877531730054X

[106] R. Xiong, J. Cao, Q. Yu, H. He, and F. Sun, "Critical review on the battery state of charge estimation methods for electric vehicles," *IEEE Access*, vol. 6, pp. 1832–1843, 2018.

[107] F. Feng, X. Hu, K. Liu, Y. Che, X. Lin, G. Jin, and B. Liu, "A practical and comprehensive evaluation method for series-connected battery pack models," *IEEE Transactions on Transportation Electrification*, vol. 6, no. 2, pp. 391–416, 2020.

[108] N.-T. Pham, P.-H. La, and S.-J. Choi, "Online cell-by-cell soc/soh estimation method for battery module employing extended kalman filter algorithm with aging effect consideration," *Journal of Power Electronics*, vol. 22, pp. 1–8, 09 2022.

[109] M. Naguib, P. Kollmeyer, and A. Emadi, "Lithium-ion battery pack robust state of charge estimation, cell inconsistency, and balancing: Review," *IEEE Access*, vol. 9, pp. 50 570–50 582, 2021.

[110] Z. Zhang, X. Cheng, Z.-Y. Lu, and D.-J. Gu, "Soc estimation of lithium-ion battery pack considering balancing current," *IEEE Transactions on Power Electronics*, vol. 33, no. 3, pp. 2216–2226, 2018.

[111] S. Liu, J. Wang, Q. Liu, J. Tang, H. Liu, Y. Zhou, and X. Pan, "A novel discharge mode identification method for series-connected battery pack online state-of-charge estimation over a wide life scale," *IEEE Transactions on Power Electronics*, vol. 36, no. 1, pp. 326–341, 2021.

[112] W. Gao, Y. Zheng, M. Ouyang, J. Li, X. Lai, and X. Hu, "Micro-short-circuit diagnosis for series-connected lithium-ion battery packs using mean-difference model," *IEEE Transactions on Industrial Electronics*, vol. 66, no. 3, pp. 2132–2142, 2019.

[113] M. Luzi, M. Paschero, A. Rossini, A. Rizzi, and F. M. F. Mascioli, "Comparison between two nonlinear kalman filters for reliable soc estimation on a prototypal bms," in *IECON 2016 - 42nd Annual Conference of the IEEE Industrial Electronics Society*, 2016, pp. 5501–5506.

[114] D. Fusco, F. Porpora, M. Di Monaco, V. Nardi, and G. Tomasso, "High performance battery soc estimation method based on an adaptive square-root unscented kalman filter," in *2022 International Symposium on Power Electronics, Electrical Drives, Automation and Motion (SPEEDAM)*, 2022, pp. 424–429.

[115] S. Karrari, N. Ludwig, G. De Carne, and M. Noe, "Sizing of hybrid energy storage systems using recurring daily patterns," *IEEE Transactions on Smart Grid*, vol. 13, no. 4, pp. 3290–3300, 2022.

[116] H. Akagi, S.-i. Kinouchi, and Y. Miyazaki, "Bidirectional isolated dual-active-bridge (dab) dc-dc converters using 1.2-kv 400-a sic-mosfet dual modules," *CPSS Transactions on Power Electronics and Applications*, vol. 1, no. 1, pp. 33–40, 2016.

[117] M. Kheraluwala, R. Gascoigne, D. Divan, and E. Baumann, "Performance characterization of a high-power dual active bridge dc-to-dc converter," *IEEE Transactions on Industry Applications*, vol. 28, no. 6, pp. 1294–1301, 1992.

[118] F. Krismer, "Modeling and optimization of bidirectional dual active bridge dc-dc converter topologies," Ph.D. dissertation, ETH Zurich, ZÃ¼rich, 2010, diss., EidgenÃ¶ssische Technische Hochschule ETH ZÃ¼rich, Nr. 19177, 2010.

[119] G. G. Oggier, G. O. García, and A. R. Oliva, "Switching control strategy to minimize dual active bridge converter losses," *IEEE Transactions on Power Electronics*, vol. 24, no. 7, pp. 1826–1838, 2009.

[120] N. Hou and Y. W. Li, "Overview and comparison of modulation and control strategies for a nonresonant single-phase dual-active-bridge dc-dc converter," *IEEE Transactions on Power Electronics*, vol. 35, no. 3, pp. 3148–3172, 2020.

[121] P. Wang, X. Chen, C. Tong, P. Jia, and C. Wen, "Large- and small-signal average-value modeling of dual-active-bridge dc-dc converter with triple-phase-shift control," *IEEE Transactions on Power Electronics*, vol. 36, no. 8, pp. 9237–9250, 2021.

[122] M. Kasper, R. M. Burkart, G. Deboy, and J. W. Kolar, "Zvs of power mosfets revisited," *IEEE Transactions on Power Electronics*, vol. 31, no. 12, pp. 8063–8067, 2016.